Fabrication of DNA origami lattice on silicon surface for DNA-assisted lithography

Master's Thesis, 30.6.2022

Author:

Heini Järvinen

Supervisors:

Jussi Toppari
Kosti Tapio
Karolina Sokolowska
Johannes Parikka

UNIVERSITY OF JYVÄSKYLÄ
DEPARTMENT OF PHYSICS

Abstract

Järvinen, Heini
Fabrication of DNA origami lattice on silicon surface for DNA-assisted lithography
Pro gradu, master's thesis
Department of Physics, University of Jyväskylä, 2022, 136 pages.

Metamaterials obtain new properties from having metallized nanoscale features that are often arranged in repeating patterns. In particular, there is a need to create metasurfaces with a negative refractive index. As nanoscale fabrication using conventional top-down methods can be both difficult and time-consuming, bottom-up techniques have gained growing interest. Especially, the DNA origami method can be utilized to assemble lattices with nanoscale features on 2D surfaces, which can then be metallized using DNA-assisted lithography (DALI). This thesis provides a full study of the DNA origami fishnet lattice assembly kinetics and optimization of lattice order on a silicon surface using liquid and air AFM imaging. Similar studies have only been performed on mica, which is unsuitable for the lithographic processes used in DALI. A fishnet lattice with nanoscale features was assembled on silicon utilizing the blunt-ended, twist-corrected Seeman tile (TC-ST) origami and ionic interactions on a solid-liquid interface. In total, the effect of six different cations (Mg^{2+}, Ni^{2+}, Ca^{2+}, Na^{+}, K^{+}, Li^{+}) on DNA origami attachment and lattice quality were studied, out of which magnesium (Mg^{2+}) and sodium (Na^{+}) produced the best quality monolayer. Additionally, for dried samples nickel (Ni^{2+}) was found to be essential for fixing the formed structures on silicon to avoid the detachment of DNA origami during washing. Also, the effect of temperature was found to be crucial for utilizing lower ionic concentrations like the ones employed on mica. Alternatively, the amount of blunt-end interactions between origami can be decreased to work in lower temperatures. In conclusion, similar fishnets with polycrystal-like lattice domains can be produced on silicon as what can be created on mica.

Keywords: DNA, DNA origami, DNA nanotechnology, lattice, solid-liquid interface, metamaterial, metasurface, negative refractive index, silicon, atomic force microscopy

Tiivistelmä

Järvinen, Heini
DNA-origami hilojen muodostaminen pii-pinnoille DNA-avusteista litografiaa varten
Pro gradu -tutkielma
Fysiikan laitos, Jyväskylän yliopisto, 2021, 136 sivua

Metamateriaalit ovat uudentyyppisiä synteettisiä materiaaleja, joilla on uusia luonnollisista materiaaleista poikkeavia ominaisuuksia. Metamateriaalien uudet ominaisuudet syntyvät usein metallisten, nanomittakaavassa symmetrisesti järjestettyjen hilarakenteiden seurauksena. Erityinen kiinnostuksen kohde on valmistaa metapintoja, joilla on negatiivinen taitekerroin. Koska nanometrien kokoisten rakenteiden valmistaminen on vaikeaa ja aikaa vievää käyttäen tyypillisiä ylhäältä-alas (*eng.* top-down) -menetelmiä, monet tällä hetkellä kehityksen alla olevat alhaalta-ylös (*eng.* bottom-up) -menetelmät ovat herättäneet kasvavaa mielenkiintoa nanomittakaavan rakenteiden valmistuksessa. DNA-origami menetelmällä voidaan kasvattaa nanometrien kokoisia toistuvia rakenteita sisältäviä hilarakenteita kaksiulotteisille pinnoille, joita voidaan myöhemmin käyttää muotteina metallisten rakenteiden kasvatuksessa hyödyntäen DNA-avusteista litografiaa (*eng.* DNA-assisted lithography, DALI). Tutkielma tarjoaa kokonaisvaltaisen tutkimuksen DNA-origami verkkohilojen (*eng.* fishnet) muodostumisen kinetiikasta ja hilajärjestyksen optimoinnista käyttäen atomivoimamikroskopiaa sekä ilmassa että nesteessä oleville näytteille. Vastaavia tutkimuksia on tehty ainoastaan mica-pinnoilla, mitkä eivät sovellu käytettäväksi DALI:ssa. Nanokokoluokan verkkohila muodostetaan ristin muotoisella, vääntö-korjatulla Seemanin tiileksi (*eng.* twist-corrected Seeman tile, TC-ST) kutsutulla DNA-origamilla, jonka reunoihin on lisätty tylpiksi päiksi (*eng.* blunt-end) kutsuttuja vuorovaikutuksia. Tylpät päät perustuvat DNA:n kaksoisjuosteen emästen aromaattisten renkaiden pinoutumiseen (*eng.* stacking) ja niitä voidaan käyttää DNA-origamien välillä attraktiivisten vuorovaikutusten luomiseen. TC-ST-origameista voidaan muodostaa hiloja ionisten vuorovaikutusten avulla hyödyntäen kiinteän pinnan ja nesteen välisiä rajapintoja. Kuuden eri kationin (Mg^{2+}, Ni^{2+}, Ca^{2+}, Na^{+}, K^{+}, Li^{+}) vaikutusta tutkittiin DNA-origamien kiinnittymiseen pii-pintaan ja

laadukkaan hilan muodostumiseen. Tutkituista kationeista magnesium ja natrium muodostivat laadukkaimman yksikerroksisen hilan. Muodostuneiden hilarakenteiden kiinnittäminen pii-pintaan nikkelin avulla osoittautui äärimmäisen tärkeäksi kuivattujen näytteiden valmistamisessa, jotta DNA-origamit eivät irtoa pinnalta näytteen pesun ja kuivaamisen aikana. Lisäksi lämpötilan säätäminen mahdollistaa matalampien ionikonsentraatioiden käyttämisen, joita hyödynnetään myös mica-pinnoilla. Tylppien päiden määrää rakenteissa voidaan vaihtoehtoisesti vähentää, jotta voidaan työskennellä matalammissa lämpötiloissa (<35 °C). Johtopäätöksenä voidaan todeta, että pii-pinnalla voidaan muodostaa samanlaisia polykristalleja muistuttavia verkkohiloja, kuin mitä pystytään muodostamaan micalla.

Avainsanat: DNA, DNA-origami, DNA nanoteknologia, hila, rajapinta, metamateriaali, metapinta, negatiivinen taitekerroin, pii, atomivoimamikroskopia

Preface

I have had the absolute pleasure to work with this project from the very beginning. I wish to give a warm thank you to Assoc. Prof. Jussi Toppari[1] for the opportunity of getting to be a part of such an amazing group, in general being a mentor and for supervising the presented thesis. I want to thank everyone in our lab group, both old and new members, for all the hard work and the best company. An additional thank you also for supervising this thesis to Dr. Kosti Tapio[1], Dr. Karolina Sokolowska[12] and Johannes Parikka[1] for all of the insightful comments. An extra thank you to Johannes Parikka for providing the extra material introduced in the appendix as well as the illustration in section 2.1. I wish to acknowledge Dr. Nemanja Markešević[1] for the kind help at the beginning of the project as well as the other personnel at NSC for creating such a welcoming and collaborative environment. I also want to thank my family and friends for all the given support and for proofreading the thesis.

A special thank you to Dr. Charlotte Kielar[3] and Dr. Kosti Tapio for imaging and providing the results in section 4.4 regarding the temperature controlled liquid AFM imaging. A special thank you to also Ashwin Natarajan[4] and Assoc. Prof. Anton Kuzyk[4] for helping our group with the cryo-EM imaging in section 4.2.3. I wish to thank all of the other collaborators of the project: apl. Prof. Dr. Wolfgang Fritzsche [5], Dr. Veikko Linko[4], Dr. Boxuan Shen[46], Prof. Mauri Kostiainen[4] and PD Dr. Adrian Keller[7] as well as the Jane and Aatos Erkko foundation and the Academy of Finland for funding the project. All of the efforts and contributions for aiding the finishing and improving the quality of this thesis are greatly appreciated.

Jyväskylä 30th of June, 2022
Heini Järvinen

[1]Nanoscience center (NSC) & Physics Dept., University of Jyväskylä (JYU), Jyväskylä, Finland
[2]PiBond Oy, Espoo, Finland
[3]Helmholtz-Zentrum Dresden-Rossendorf (HZDR), Dresden, Germany
[4]Aalto university, Espoo, Finland
[5]Leibniz Institute of Photonic Technology (Leibniz-IPHT), Jena, Germany
[6]Karolinska Institutet, Stockholm, Sweden
[7]Paderborn University, Paderborn, Germany

Contents

Abbreviations

AFM = atomic force microscopy
BLIN = biotemplated lithography of inorganic nanostructures
α-Si = amorphous silicon
CPD = contact potential difference
CVD = chemical vapour deposition
cryo-EM = cryogenic electron microscopy
DALI = DNA-assisted lithography
DNA = deoxyribonucleic acid
dsDNA = double-stranded DNA
HCL = honeycomb lattice
ICP-RIE = inductively coupled plasma reactive ion etching
IDT = integrated DNA technologies
IPA = isopropanol or 2-propanol
KPFM = kelvin probe force microscopy
MEMS = micro-electro-mechanical-system
mono-Si = monocrystalline silicon
NIM = negative-index metamaterial
NTC = non-twist-corrected
PCR = polymerase chain reaction
PECVD = plasma-enhanced chemical vapour deposition
PVD = physical vapour deposition
QNM = quantitative nanomechanical mapping
RF = radio frequency
RNA = ribonucleic acid
RIE = reactive ion etching
RMSF = root-mean-square fluctuation
RT = room temperature
sc-Si = single-crystal silicon
SEM = scanning electron microscope

SFM = scanning force microscopy
Si = silicon
SiN = silicon nitride
SKPM = scanning kelvin probe microscopy
SPM = scanning probe microscopy
SQL = square lattice
ssDNA = single-stranded DNA
ST = seeman tile
TC = twist-corrected
UV = ultraviolet
ZS = z shape

1 Introduction

Optical metamaterials are new type of materials having properties and features that are not otherwise encountered in nature or conventional materials [1]. New unnatural properties can arise from special shapes, sizes and arrangements that are able in some form to manipulate electomagnetic waves [2]. In particular, metasurfaces are trends of the future that offer means to create compelling future applications such as the superlens [1, 2]. There is also a particular interest in creating materials that exhibit a negative refractive index for certain wavelengths, referred to as a negative-index metamaterial (NIM) [2, 3].

Generally, metasurfaces are formed out of regular, metallic lattice structures that are often difficult to fabricate on the nanoscale. Although, top-down methods are typically used to fabricate such surfaces, emerging bottom-up approaches have garnered interest due to promise of simpler methods and low cost [4]. However, the fabrication of metasurfaces using bottom-up techniques requires precise, nanoscale control of the dimensions and positioning of the structures, which is in general hard to achieve.

The DNA origami method can be utilized to form nanoscale lattices on 2D surfaces [4–6]. As creating DNA origami structures is based on self-assembly of the double-stranded DNA (dsDNA) helix, it provides a profound means to work on the nanoscale with unprecedented precision and feature sizes down to 6 nm [7]. Such a bottom-up method offers effortlessly programmable shapes and patterns without the need for less efficient top-down techniques, *e.g.*, ion-beam patterning, remaining costly in both time and resources [4, 8]. The DNA origami method provides superior means to work on the nanoscale but does not by itself introduce novel properties required of a metamaterial. Since most of the prominent metasurfaces are produced out of metals, transforming the shapes of origami into metallized structures is required. DNA-assisted lithography (DALI) is a method previously created for transforming the silhouettes of origami deposited on 2D surfaces into metallized structures using quintessential lithographic processes [8]. Therefore, DALI in combination with the DNA origami approach can be used to create metasurfaces with almost any pattern

imaginable.

This thesis introduces the formation kinetics of a large-scale 2D "fishnet" lattice out of the Seeman tile (ST) origami, *i.e.*, a cross-tile shaped origami utilizing blunt-end interactions between origami. Blunt-end interactions are based on π-stacking of protruding π-orbitals at the ends of the dsDNA helices and are considerably weaker than, *e.g.*, sticky-ends that are based on base pairing interactions of short complementary strands [4]. In theory, a weaker interaction should be able to correct a higher proportion of forming lattice errors and flaws as the origami can attach and detach in repeated cycles. In addition, the blunt-end interactions can be more easily controlled using external stimuli in comparison to the more sturdy DNA hybridization.

DNA origami can be attached on a negatively charged surface using divalent cations (ions having a charge of +2) that create a salt bridge between the surface and the negatively charged origami [4]. The solid-liquid interface is exploited to support the efficient growth of a single layer of lattice. Furthermore, interactions with the surface can be adjusted by modifying the ionic conditions as the presence of monovalent cations can increase origami diffusion by screening or neutralizing charge from the surface [5].

Fishnet lattices have already been assembled on an inherently negatively charged mica surface using sticky-ends exceeding to dimensions of a few micrometers [9]. An area of $15\,\mu m \times 15\,\mu m$ can also be covered with a single layer of ST origami on mica using blunt-ends having a polycrystal-like arrangement of small, assembled fishnet structures [6]. Unfortunately, the mica surface is unsuitable for any further lithographic processing in DALI and therefore lattice assembly needs to be optimized on a different surface [8]. Silicon is a common substrate typically used in conventional lithography and suitable for DALI processing. For these reasons, it was chosen to be optimized for ST origami lattice assembly.

2 Theoretical background

The theoretical section begins with a detailed description of the DNA molecule and interactions it can have with different cations as DNA origami lattice assembly is highly dependent on the ionic conditions. Next, a brief history and theoretical background of DNA origami is presented. The chosen ST origami is also covered in detail. Commonly used surfaces referred to as substrates for origami deposition are described and compared briefly, after which the theoretical details for assembling lattices out of DNA origami are introduced. Furthermore, the section continues with theoretical descriptions of the utilized processes needed to treat the used substrates as well as the lithographic steps of DALI. Next, metamaterials are covered in more detail to reveal the most appealing uses and future applications for such materials. The metamaterial section outright discusses the motivation behind working towards optimizing the protocols used in creating metasurfaces. The final section introduces the basis behind the AFM imaging technique.

2.1 DNA molecule and ionic interactions

The deoxyribonucleic acid (DNA) molecule is responsible for storing all the genetic information of life as a sequence of four bases. DNA is a polymer and consists of building blocks called nucleotides. A single nucleotide in DNA consist of the deoxyribose five-carbon sugar, a nitrogen-containing base and a phosphate group [10]. When multiple nucleotides are combined they form a polymer chain referred to as single-stranded DNA (ssDNA). As demonstrated by figure 1, the phosphate group together with deoxyribose form the backbone of a DNA strand whereas the base hydrogens bond with another base of a second nucleotide to form the double stranded DNA helix (dsDNA) [10].

A single DNA strand expresses a direction that runs from the five prime (5') end to the three prime (3') end as demonstrated by figure 1. The type of end is determined from the backbone of DNA from the bonds between the phosphate groups and the number of carbon in the sugar group. The 3'-end has an open hydroxyl

group (OH) bonded on the third carbon in the sugar ring. The 5'-end has an exposed phosphate group (PO_4^{3-}) that bonds to the fifth carbon of the sugar ring.

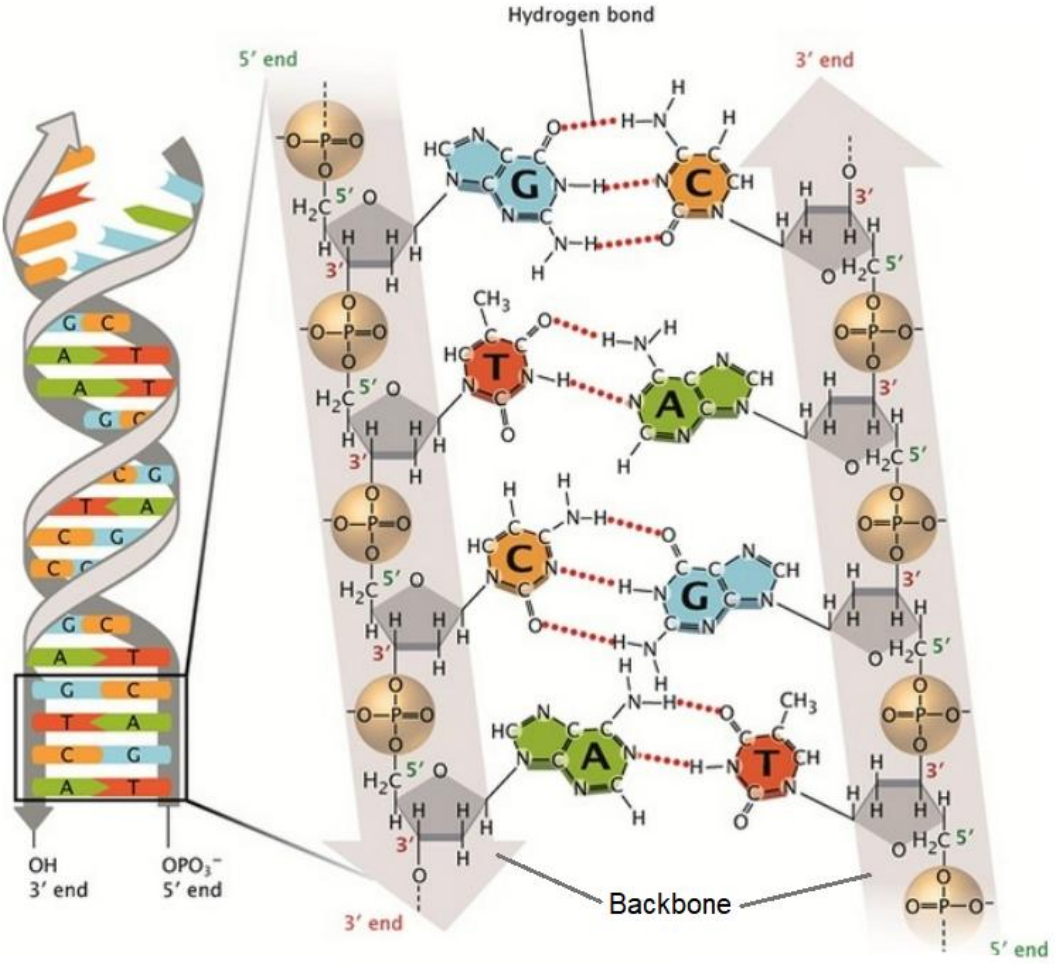

Figure 1. The chemical structure of dsDNA according Watson and Crick [11]. A representation of the dsDNA helix is shown on the left. On the right, a description of the backbone structure is shown inside the grey arrows. A strand runs in the direction of the grey arrow from 5' to 3' end. Also, the four hydrogen bonded bases are shown between the grey arrows. Adenine (A, in green), thymine (T, in red), Cytosine (C, in orange) and guanine (G, in blue). Adapted with permission from [11]. © 2008 Nature Education.

According to Watson-Crick base pairing only two pairings are allowed in most of the physiological conditions [12]. Adenine (A) can only bond with thymine (T) with two hydrogen bonds, whereas cytosine (C) only bonds with guanine (G) with three hydrogen bonds. The bases A and G represent purines whereas T and C are pyrimidines. An alternative base pairing geometry was later reported by Hoogstein

that would result in a different quadruplex shape [13]. The Hoogstein base pairing is achieved by rotating one of the bases in the pair by 180°. In the Hoogstein geometry both pairings (A-T and C-G) will be held together using two hydrogen bonds in the major groove of dsDNA [14]. When two DNA strands are hydrogen bonded together through base pairing, the molecule twists into a helical structure that exhibits two types of turns, called the major and minor grooves [10]. The helical shape of DNA is based on the π-stacking interactions between the aromatic rings of the bases which further stabilize the dsDNA helix [10].

Three different conformations exist for the dsDNA helix, out of which B-DNA is the most common and the assumed model for the helix in DNA origami. In the B-DNA conformation, a single nucleotide corresponds to a rise of 0.34 nm in the helix and one repeating turn in the helix consists of approximately 10.5 nucleotides. Also, the diameter of the individual helix is 2 nm. A-DNA is a wider conformation mainly found in dehydrated environments. The Z-DNA conformation is adopted when bases go through methylation. Unlike A- and B-DNA, Z-DNA is the only conformation to express a left-handed spiral. [10, 11]

2.1.1 Binding sites for ions

As the thesis studies the formation kinetics of DNA origami lattices on 2D surfaces with the help of cations (discussed further in sections 2.2 and 2.4), it is crucial to understand what roles and properties each cation embodies in the DNA molecule. Cation binding can affect the interactions between individual DNA origami and the binding of origami on the surface. Different ions express a preferred binding site in DNA either in the phosphates of the DNA backbone or the bases. Differences in the preferred binding sites can be based on varying ionic radii and the amount of ionic charges. Since the DNA molecule is inherently negatively charged, due to the phosphate groups in the backbone, mainly positively charged cations are attracted to DNA. Although, the dsDNA helix is held together by base pairing and π-stacking interactions, the structure is further stabilized by using cations like sodium and magnesium that neutralize the electrostatic charges and thus the repulsion between ssDNAs.

The atomic and ionic radii, hydration enthalpies and preferred binding sites in the DNA molecule are presented for six elements in table 1. The presented ions can be divided into two groups based on the amount of charge they possess. A cation

can be divalent or monovalent, having either a charge of +2 or +1, respectively. Out of all the introduced alkali and alkaline earth metals, lithium has the smallest ionic radius whereas potassium has the largest. However, being a transition metal, nickel has an even smaller atomic radius than lithium. As most of the introduced ions prefer to bind to the backbone phosphates, the most notable differences between the preferred binding sites include nickel and potassium. Nickel is able to bind both binding sites in DNA, phosphates and the bases, whereas potassium prefers to only bind the bases.

Table 1. The atomic and ionic radii of elements are presented in pm [15, 16]. Experimental hydration enthalpies ($-\Delta H^\circ_{\text{hyd}}$) for the ions are presented in kJ/mol [17]. Also, the preferred binding site in the DNA molecule are presented for each ion [5].

Atom	**Atomic radius** (pm)	**Ion**	**Ionic radius** (pm)	$-\Delta H^\circ_{\text{hyd}}$ (kJ/mol)	**Binding site**
Mg	160	Mg^{2+}	65	1921 ± 6	Phosphates
Ni	123	Ni^{2+}	70	2105 ± 6	Phosphates, bases
Ca	197	Ca^{2+}	99	1577 ± 6	Phosphates
Na	186	Na^{+}	95	409 ± 3	Phosphates
Li	152	Li^{+}	60	519 ± 3	Phosphates
K	227	K^{+}	133	322 ± 3	Bases

The absolute hydration enthalpy in table 1 for each ion describes the magnitude of attraction between the specified ion and a water molecule. In general, smaller ions have a higher absolute hydration enthalpy and the values increase for more highly charged ions. Therefore, any divalent cation has a higher enthalpy compared to monovalent cations. The differences in ionic radii lead to varying charge densities between mono- and divalent cations, which in turn can lead to varying hydration behaviour. The hydration behaviour correlates with the ability of an ion to replace other ions from the DNA molecule [6]. The available binding sites for cation binding in the DNA backbone and the nucleobases are demonstrated in figure 2[8]. Cations can create coordination bonds with lone pairs of the phosphate groups in the DNA backbone and with the carbonyl and tertiary amine groups in the nucleobases [18, 19].

[8]The chemical structure of the ssDNA was kindly provided by Johannes Parikka.

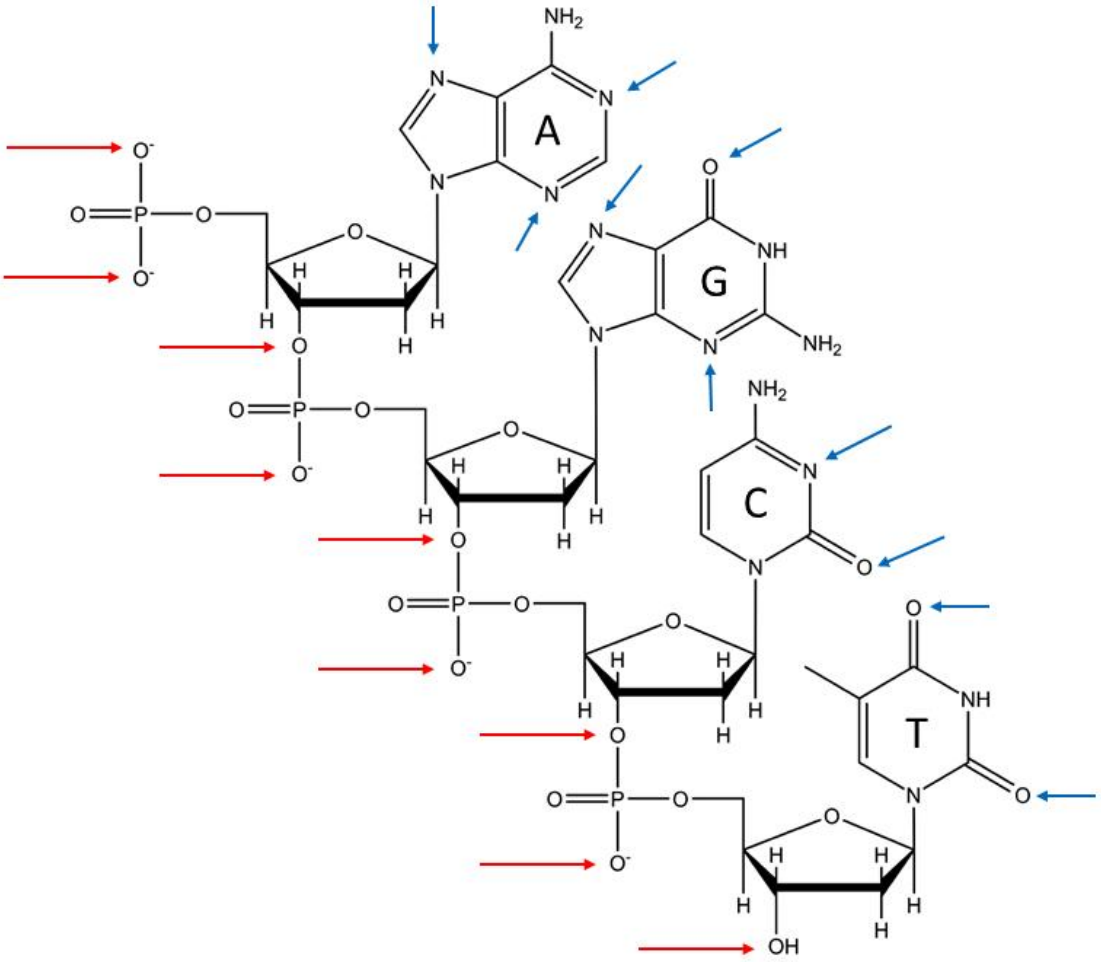

Figure 2. A chemical structure of a ssDNA base sequence of 5'-AGCT-3' (read from top to bottom). Red arrows demonstrate binding locations for cations in the DNA backbone [18]. Blue arrows demonstrate binding locations for cations in the nucleobases [19].

The binding of ssDNA to a surface called mica (discussed in section 2.3) in the presence of transition metal cations was found to correlate with the ionic radii [20]. These experiments suggest that the varying binding strengths of ions are based on their ionic sizes. The cations with an ionic radii from 69 pm to 74 pm bind the DNA effectively to mica [20]. Ionic radii of 82 pm binds DNA on mica only weakly and radii from 97 pm to 110 pm exhibited poor if not nonexistent adsorbance [20]. Most likely, bigger ions start experiencing more and more of steric hindrance as the binding sites in DNA get too small. Nickel, with ionic radius of 70 pm, is a transition metal which binds strongly to the DNA backbone [5]. Although, the absolute hydration enthalpy of nickel shown in table 1 is higher than for magnesium, the affinity of

binding the DNA phosphate groups was found to be stronger with magnesium ions, with ionic radii of 65 pm, compared to nickel [21]. Although, the binding ability of ions seems to decrease for increasing ionic radii, nickel was still expected to be a stronger binder as a transition metal. This conflicting result might be explained by the partial preferred nucleobase binding of nickel, since ions are shared between multiple locations. Furthermore, the affinity of a metal ion binding the bases in DNA was also found to be sequence dependent [22].

Lithium is known to possess tight hydration shells and has the highest absolute hydration enthalpy of the monovalent cations described in table 1. For these reasons and because of the small size of the lithium ion resulting in higher charge density compared to sodium, lithium does not have as strong binding affinity to the phosphates as the other alkali cations [5]. Therefore, out of the introduced monovalent ions, sodium is found to be the most efficient in displacing divalent cations [6]. Especially, out of the introduced divalent cations calcium was found to be more easily displaced from the phosphates of DNA by sodium ions compared to magnesium [5]. As demonstrated by table 1, the ionic radius of sodium is very close to that of calcium. Possibly, similar ionic radii can also have an effect on the affinity of replacing other ions.

2.1.2 Absorption measurement

The concentration of DNA in solution can be determined using a spectrophotometer [23]. The principle of nucleic acid detection is based on the absorption of ultraviolet (UV) light by the heterocyclic rings of the nucleobases. The conjugated double bonds in the purine and pyrimidine rings of bases have a charasteristic, broad absorbance peak at a wavelength of 260 nm (A_{260}) [24]. The final nucleic acid concentration can be determined using the A_{260} value and the Beer-Lambert law [25]

$$A = \varepsilon \ell c, \tag{1}$$

where ε is the molar attenuation coefficient or extinction coefficient of the absorbing species, ℓ is optical path length and c is the concentration of the absorbing species. Furthermore, the determination of the absorbance peak at a wavelength of 280 nm (A_{280}) can be used to assess purity of the given sample as the A_{280} should be half of A_{260} [24]. Typically, organic impurities, *e.g.*, proteins and ribonucleic acid

(RNA), absorb in the same UV range but the A_{260} peak for proteins is lower than the A_{280} peak [24]. Therefore, the A_{260} to A_{280} ratio varies in the presence of impurities and should be about 1.8 for pure nucleic acid solutions [24]. Also, other external factors like pH and ionic strength can further affect the absorbance spectrum [23].

2.2 DNA origami

The DNA origami method creates 2D and 3D structures out of ssDNA [7, 26]. The method is able to create specific structures with 6 nm feature sizes that are simple and easy to design using automated computer software called caDNAno [27]. The creation of DNA origami is based on self-assembly of the dsDNA helix and (mostly Watson-Crick) base pairing. Each origami can be individually designed out of a longer scaffold strand, typically the M13mp18 bacteriophage genome, and shorter oligonucleotides referred to as staple strands, which are used to staple the scaffold in the form of the wanted shape as shown in figure 3 [7].

Nadrian C. Seeman is referred to as the founding father of DNA nanotechnology as he was one of the first people to utilize DNA structures referred to as the immobile 4-arm junctions [28]. Seeman's junctions were influenced by the resembling holliday junctions found in nature during gene expression in meiosis. The aim of Seeman was to order proteins into symmetrical crystal positions to determine the 3D shape of the proteins with X-ray crystallography. The scope of the DNA origami method was later emphasized in an article by Paul W.K. Rothemund in 2006 [7]. The effortless programmability of the user-specific designs and the small feature sizes of DNA origami give it an advantage for creating nanoscale structures over the more conventional top-down methods, *e.g.*, electron beam lithography, that are both time consuming and expensive.

Preceding Rothemund and the DNA origami technique, a similar approach was published by William M. Shih *et al.* to create structures out of DNA [29]. This approach exploited the 4-arm junction created by Seeman in forming a 3D octahedron [29]. Following the release of these approaches, the DNA origami method was adapted to form hollow 3D structures [26, 30–32]. Later, automated design programs started emerging for the creation of 2D (SARSE) [33] and 3D origami (caDNAno) [27]. These programs introduced features like curvature by skipping or adding bases [34], design of sticky-ends and hairpin-loops [27] and ways to create even bigger origami referred to as superstructures with the help of sticky-ended DNA bricks [35] and

origami wireframe networks [36–38]. Nowadays, automated design programs for more complex structures can be achieved using software like DAEDALUS and vHelix [39–41].

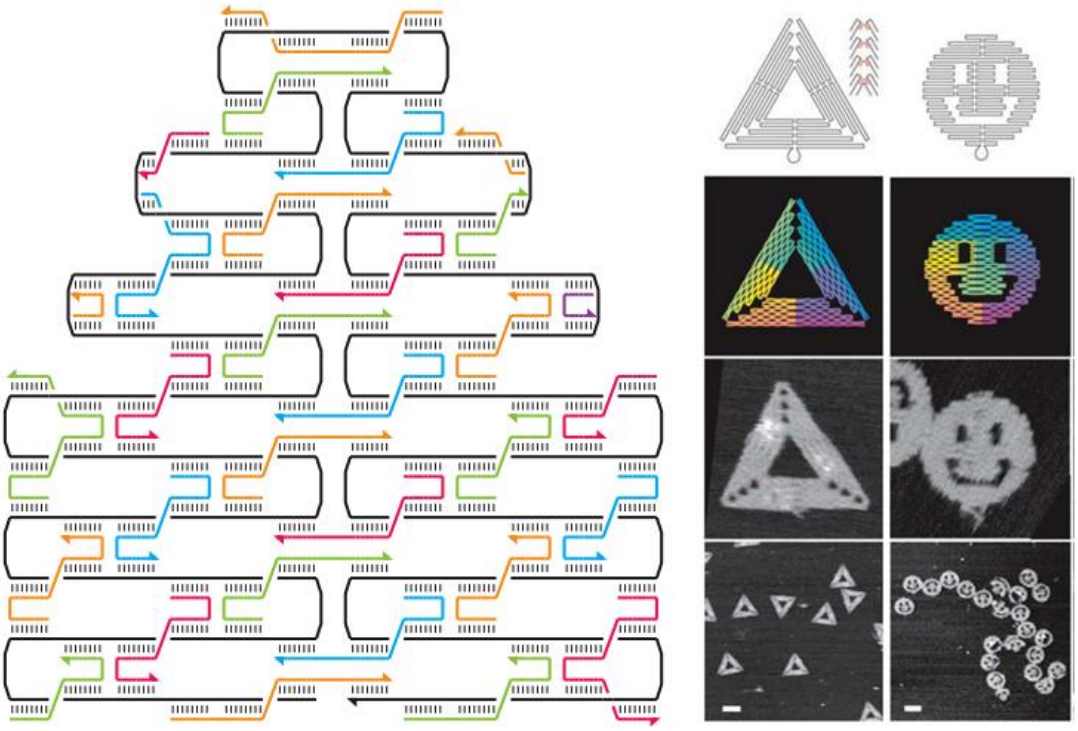

Figure 3. As shown on the left, DNA origami are formed out of a long scaffold (black strand) and a multitude of shorter oligonucleotides (colorful strands) that staple the scaffold in the wanted shape. Arrows represent the directionality of the ssDNA. Black, vertical lines between strands represent base pairing and formation of the dsDNA helix. On the right, two well-known DNA origami designs of Rothemund are presented: the Rothemund triangle and the smiley. The top-most images demonstrate the routing of the scaffold in the origami. On the second row, the scaffold routing is demonstrated in color, where red shows the beginning and purple the end of the scaffold. In the two bottom images the folded DNA origami are imaged with AFM. Both origami structures are designed to be 100 nm in size. The scales of the bottom images are 100 nm. Adapted with permission from [7]. © 2006 Nature.

2.2.1 The Seeman tile (ST) design and twist-correction

As the thesis studies connected structures formed out of the Seeman tile (ST) origami, the specifics of this origami design are covered in more detail. In general, two types of designs can be created for each origami which are referred to as the non-twist-corrected (NTC) and twist-corrected (TC) design. The twist-correction for origami is created to prevent the floppiness or twisting of the structure. One helical turn in the natural found B-DNA has approximately 10.5 nucleotides per turn as discussed in section 2.1. The structural distortion in designing DNA origami originates from having an average twist of 10.67 per helical turn [4]. This difference in the helical twist accumulates over hundreds of units when forming full DNA origami structures [4]. Therefore, the strain in the helix needs to be relaxed by omitting a base pair for every 48th nucleotide when designing origami using the square lattice (SQL) as the base for the relative positioning between adjacent dsDNA helices [42]. Another approach to relieve the strain of the DNA helix is to design the DNA origami on the honeycomb lattice (HCL), which brings a natural minimization of twist for the structure due to a natural helical turn of 10.5 bases [43].

The ST origami is designed utilizing the SQL and is composed of two 100 nm long rectangles which bind together in the middle forming the shape of a plus or a cross. Therefore, one of the rectangles can be seen to be on top of the other. This top-most rectangle has a hole around the connection point to the bottom rectangle resulting in two areas of bumps in the middle of the origami, which are examined more closely in section 4.1 using AFM imaging. A conformational AFM image of the TC-ST origami is presented in figure 2 of article [9]. A CanDo simulation of the NTC-ST origami is presented in figure 4. As can be seen, the NTC-ST is very floppy in shape and can be made flat only in the presence of a supporting surface. In contrast to the NTC-ST, the side-profile of the z shape (ZS) origami is mainly straight since it is formed using the HCL.

The caDNAno design for the TC-ST design is provided by Rafat *et al.* with a full listing of the 210 staple base sequences as well as the M13mp18 scaffold sequence [6]. 24 of the oligonucleotide staple sequences are referred to as edge staples which are situated on the edges of the four arms of the plus-shaped origami. The ST origami is designed to connect with neighboring STs from the ends of the cross-tile arms to form a fishnet lattice. The edge staples are responsible for creating protruding π-orbitals at the ends of the dsDNA helices resulting from the stacking interactions

of the aromatic rings of the nucleobases. There are six edge staples per origami arm, which create in total twelve helices available for blunt-end interactions. Result section 4.3 experiments with decreasing the amount of blunt-end interactions from the arms of the origami, which obeys the following notation. For a full design, having 6 edge staples on each of the 4 four origami arms, uses a notation of 6×4 blunt-ends. The number of the blunt-end interactions is decreased by omitting some of the edge staples from the design. The edge staples are removed first from the edges of the arms moving to the center. Therefore a 4×4 blunt-end design has four edge staples remaining in the middle of the arm as one edge staple is removed from both sides. A design with 0×4 blunt-ends has removed all of the edge staples from the origami design.

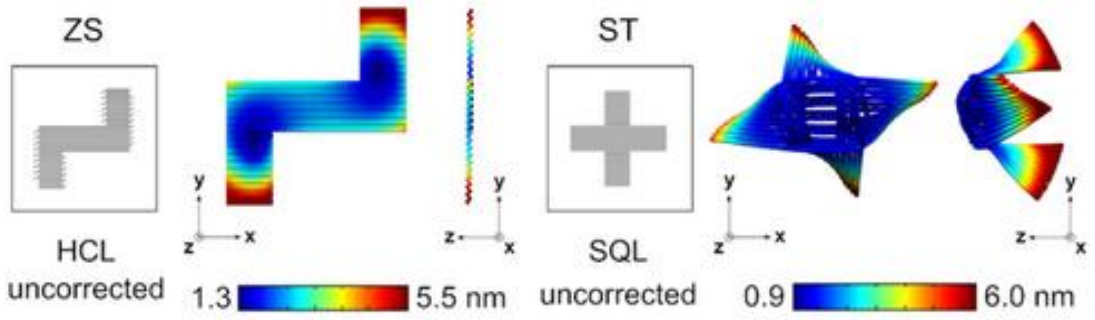

Figure 4. Cando simulations for two different DNA origami structures. On the left, a root-mean-square fluctuation (RMSF) of the z shape (ZS) and on the right, of the seeman tile (ST, with omitted side strands). The term uncorrected refers to a NTC design. Adapted with permission from [44]. © 2019 ChemBioChem

The combinations of different bases in the blunt-ends can lead to different binding strengths. In general, the weakest blunt-end interactions are formed between 3-pyrimidine interfaces that are stacked on 5' purines, *e.g.*, in the CG:AT combination [45]. When purines are stacked on purines or pyrimidines on pyrimidines, *e.g.*, in the AT:AT combination, the interaction strength becomes intermediate [45]. The strongest interactions are formed when 3' purine interfaces are stacked on 5' pyrimidines, *e.g.*, GC:CG or AT:TA [45].

2.3 Substrates

To form the 2D DNA origami lattice and to image them, the structures need to be deposited on suitable substrates. One of the most commonly used substrates for DNA origami imaging is the atomically flat mica. Mica refers to a group of minerals consisting of hydrous potassium and aluminum silicates [46]. A well-known property of these minerals is their layered structure of thin and elastic, two-dimensional sheets. This main advantage allows the robust creation of thin-films that are both tough and transparent. The low thermal and electrical conductivity as well as chemical stability are also important characteristics of mica [46]. A few different types of mica exist, where the main difference arises from having different cations present in the structures. The commercially most widely used mica types are muscovite and phlogopite mica [46]. Structurally, muscovite is a hydrous potassium aluminium silicate ($KAl_2[Si_3AlO_{10}][OH]_2$) whereas phlogopite is a hydrous magnesium aluminum silicate ($KMg_3AlSi_3O_{10}[FOH]_2$). Out of the two, muscovite mica has a lighter color compared to the dark brownish complexion of phlogopite.

The chemical structure of muscovite mica is presented in figure 5. The basic units of mica sheets are composed of two layers of polymerized silica (SiO_4) tetrahedrons which are bound together by cations (aluminium in muscovite) and hydroxyl pairs [47]. This firmly bound double-layer has the bases of the tetrahedrons on both outer-layers of the sheet, which is inherently negatively charged. These negative charges are balanced with large cations (like potassium in muscovite) bringing the individual silica sheets into a multilayered structure [47]. Since the interactions between individual sheets of mica are coulombic, instead of robust covalent bonds, the sheets can be easily cleaved layer by layer using even regular scotch tape.

Also, two types of silicon surfaces are discussed to present an alternative to mica that are more suitable for any lithographic processing. The difference between the two silicon surfaces is based on their fabrication resulting in different structural composition. Figure 6 presents the difference between an ordered single-crystal and an randomly assembled amorphous solid. Additionally, a third type of composition is presented having a polycrystalline nature. In polycrystals, smaller, ordered pieces of (single-)crystals are packed together into a solid. This kind of structure exhibits a multitude of grain boundaries.

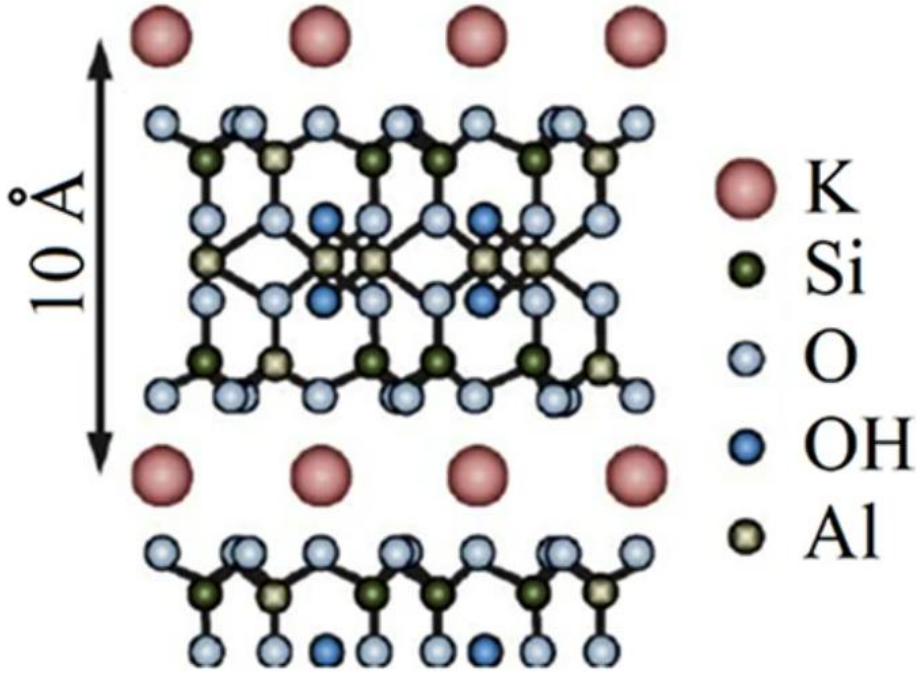

Figure 5. The atomic structure of muscovite mica ($KAl_2[Si_3AlO_{10}][OH]_2$). The negatively charged aluminosilicate layer can be easily cleaved off by breaking the coulombic interactions to the positively charged layer of K^+ ions. Adapted with permission from [47]. © 2020 Encyclopedia Britannica.

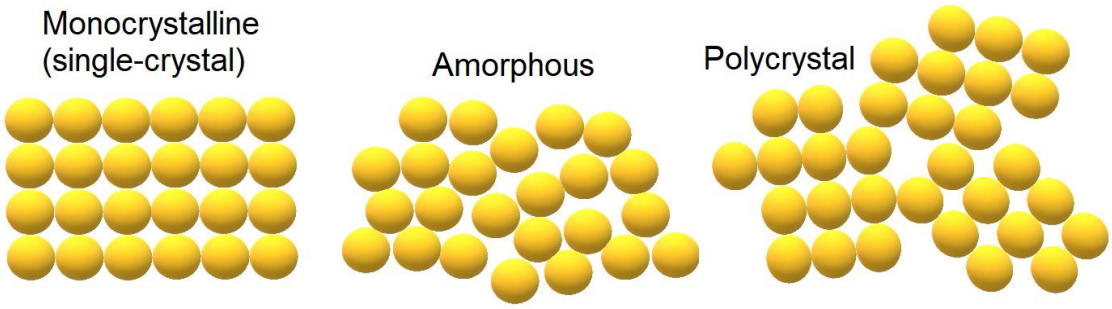

Figure 6. Three types of structural compositions for a solid. The monocrystalline solid on the left consists of perfectly ordered atoms through the whole solid, whereas the amorphous structure is thoroughly randomly assembled. The polycrystalline solid on the right consist of smaller, ordered crystals that are packed together in different orientations.

Monocrystalline silicon (mono-Si), which is more commonly known as single crystal silicon (sc-Si), is a type of silicon wafer that has a continuous crystal lattice structure through the whole solid as shown in figure 6. This type of material is free of any grain boundaries and hence forms a single crystal of solid. In more detail,

silicon forms a diamond cubic crystal structure with a lattice spacing of 542 pm [48]. This corresponds to a face-centered cubic Bravais lattice with 8 atoms contained in the unit-cell [48]. Wafers made out of sc-Si can be purely silicon based or can be doped with boron or phosphorus to create a p- or n-typed semiconductors. The most common type of sc-Si production technique is the Czochralski method [49].

The second type of silicon, amorphous silicon (α-Si), can be grown on a base wafer using plasma enhanced chemical vapour deposition (PECVD). The growing technique results in an amorphous composition introduced in figure 6. Both types of silicon substrates are used in microelectronics, semiconductors and sensor applications, *e.g.*, accelerometers (acceleration, vibration and shock sensors) and micro-electro-mechanical-systems (MEMS) sensors as well as solar cell manufacture [50, 51]. Although, sc-Si is more commonly used in solar cells and microelectronics because of the low surface roughness. The roughness tool of the Nanoscope Analysis software was used to determine the mean surface roughness for both silicon wafers. The mean surface roughness of a sc-Si wafer was determined to be 0.275 nm and 0.954 nm for an amorphous silicon wafer. Both surfaces are used in this thesis to study the effect of surface roughness on origami adsorption. Additionally, sc-Si is cheaper and simpler to work with as it does not require PECVD growing and is readily available to order. Therefore, many of the protocols in the thesis are first optimized using sc-Si, after which the experiments are continued with the α-Si surface. The switch is also done since the DNA-assisted lithography (DALI) method requires silicon nitride (Si_3N_4) or sapphire (Al_2O_3) to be used as a base wafer for the silicon layer (see section 2.6).

2.4 Lattice assembly on a solid-liquid interface

A lattice in its basic meaning can be defined as a repeating arrangement of points, or more broadly, a repeating structure. In optics, different arrangements of slits and grooves are used as lattices that can be used to manipulate light by diffraction [52]. The dimensions of the lattice features need to be similar to the scale of the phenomena affected. The DNA origami method can be harnessed to create easily programmable shapes and lattices on flat 2D surfaces with feature sizes of around 6 nm.

Depending on the symmetry of the used origami and interactions between the structures, different types of large-scale lattices can be achieved. The DNA origami structures can be assembled into lattices either by utilizing close-packing or joint

interactions as demonstrated in figure 7 [6]. Close-packing is based on maximizing the attractive forces between structures as well as surface coverage and the final lattice is greatly affected by the symmetry of the structures used. Another type of lattice can be assembled by joint interactions, which include strong sticky-end hybridization and weaker blunt-end stacking interactions [4].

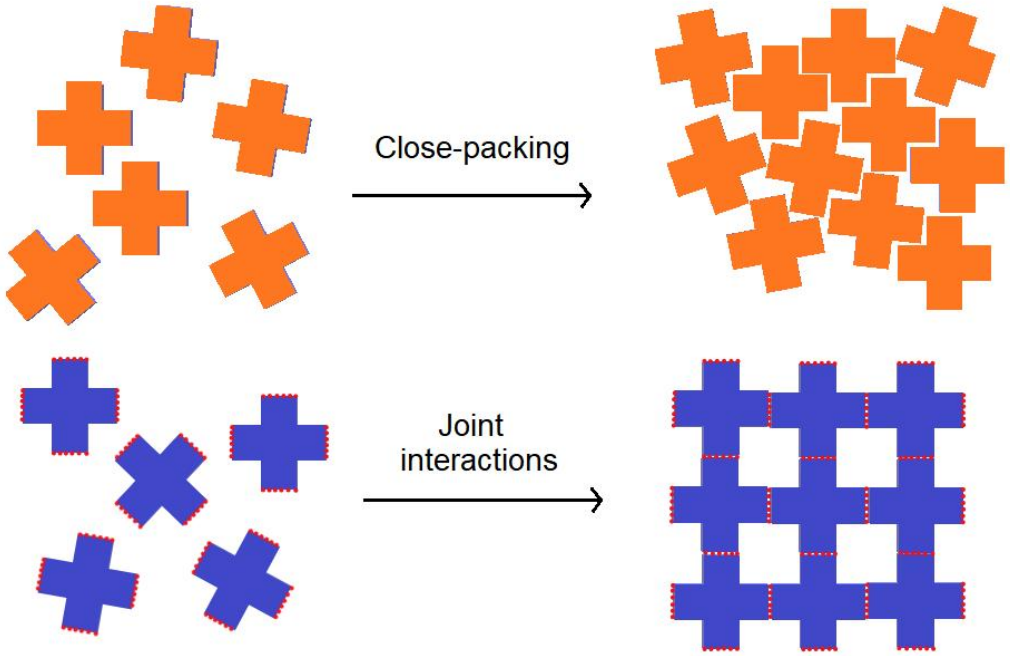

Figure 7. An example of using close-packing and joint interactions for assembling a lattice with the ST origami. Close-packing results in tightly packed structures, whereas joint interactions for the origami design result in a lattice resembling a fishnet. The orange structure represents a ST origami without interactions added on the ends of the four arms. The blue structure represents a ST with blunt-ends added on the arms. The red dots represent the protruding π-orbitals at the ends of the dsDNA helices. Similar lattice could also be assembled using sticky-ends between the origami.

As demonstrated by figure 8, sticky-ended connections are based on short, unhybridized ssDNA segments, usually at the edges of the DNA origami structure. Therefore, two origami can be hybridized together via complementary sticky-ends. On the other hand, blunt-end interactions are based on π-orbital stacking interactions between the aromatic rings of the nucleobases at the ends of the dsDNA helix as discussed in section 2.2.1. Blunt-end interaction as well as a third interaction type combining the two approaches are also shown in figure 8. In general, blunt-end inter-

actions are weaker interactions compared to sticky-ends since they utilize hydrogen bonding between nucleobases, as explained in section 2.1.

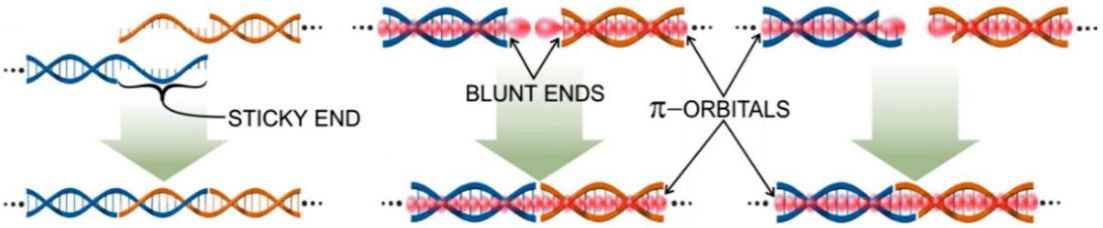

Figure 8. On the left, a demonstration of sticky-end hybridization between two DNA strands. Sticky-ends consist of short complementary ssDNA segments at the ends of the DNA helices. In the middle, a demonstration of protruding π-orbitals at the ends of dsDNA helices forming blunt-end interactions between two strands of DNA. Both of these approaches can be combined into a third type of interaction shown on the right, using only a few unbound bases at the ends of DNA helices to also include the effect of the π-orbitals on the interaction. Adapted with permission from [4]. © 2021 Molecules.

DNA origami lattice assembly is typically achieved by drop-casting the origami on a solid 2D surface [53]. Solid surfaces facilitate the growth of 2D DNA lattices by providing a suitable interface for binding [54]. In addition to the type of interactions used between origami, lattice assembly is also affected by the ionic conditions on the solid-liquid interface. Solid-liquid interfaces are able to control the ionic densities and thus the interactions between surface and origami [54]. Since DNA is a negatively charged molecule, positively charged cations can be used to further stabilize the helical structure as discussed in section 2.1.1. DNA origami are typically deposited on a negatively charged surface with the help of divalent cations, *e.g.*, Mg^{2+}. Divalent cations are able to form salt bridges, a combination of ionic interactions and hydrogen bonds, between origami and the substrate surface as shown in figure 9. In addition, monovalent cations, *e.g.*, Na^{+} can be used to screen some of the surface charge decreasing the amount of formed salt bridges [6]. As a result the origami are bound more loosely which increases origami mobility on the surface as demonstrated in figure 9. The addition of monovalent cations often improves the lattice quality significantly on mica for blunt-ended origami designs [6].

In addition to surface adsorption by the creation of salt bridges, divalent cations are known to lower the electrostatic repulsion between origami [6]. A continuous addition of divalent cations will ultimately lead to aggregating depletion forces to

become dominating [55]. Also, increasing the concentration of multivalent cations can lead to partial or total charge inversion of the DNA molecule resulting in attractive coulombic forces between origami and DNA condensation [5, 56–58]. In comparison, monovalent ions mainly neutralize the backbone charges without increasing the attractive forces between individual origami. Most likely, the electrostatic repulsion between DNA origami can be further decreased by introducing ions that bind both binding sites, phosphates as well as the bases, by increasing the number of bound ions in the structure. The higher the amount of binding sites in DNA, the stronger the charge inversion. Therefore, potassium and nickel are likely to promote origami-origami interactions and formation of multilayered structures [5].

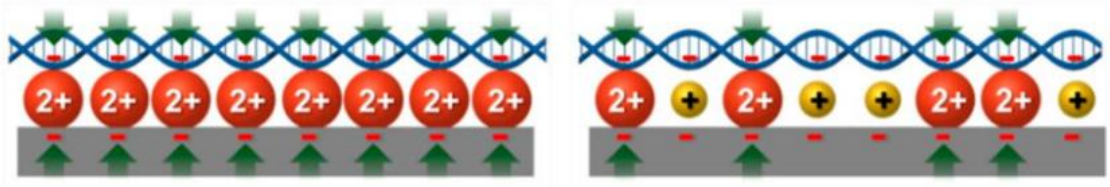

Figure 9. As shown on the left, DNA origami can be deposited on a negatively charged surface using divalent cations [4]. The green arrows represent a formation of a salt bridge between the origami and the surface. On the right, the effect of adding monovalent cations is able to decrease the amount of salt bridges formed between the origami and the surface. Therefore, monovalent cations are able to decrease origami adsorption and increase the origami mobility on the surface [4]. Adapted with permission from [4]. © 2021 Molecules.

Low concentrations of divalent cations (5 mM) are already able to stabilize DNA origami. Although, if DNA is stored for long periods of time it is more commonly immersed in buffers containing monovalent cations, *e.g.*, NaCl and is typically frozen [59]. For short periods of time DNA origami are commonly stored in buffers containing magnesium at concentration of 12.5 mM. As discussed in section 2.3, mica is an inherently negatively charged surface commonly adopted for DNA origami deposition. The ST origami introduced in section 2.2.1 uses blunt-end interactions to form a fishnet lattice. This approach has been previously used to assemble fishnet lattices on mica as shown in figure 10 resulting in a polycrystal resembling formation of small, ordered lattices in an area of 15 µm×15 µm. Furthermore, the sticky-end hybridization approach has also been adapted for the ST origami, as shown in figure 11. With this approach, well-ordered lattices of about 2 µm×3 µm can be achieved. Although, bigger structures of even 10 µm were reported to have been found, the one

presented was the cleanest out of all imaged lattices. When sticky-ends are used, any forming lattice defects are more likely to remain in the structure. The main advantages of introducing blunt-end interactions between origami include a higher rate of spontaneous lattice corrections and better prospects of using external stimuli to control the origami attachment scheme and therefore lattice assembly.

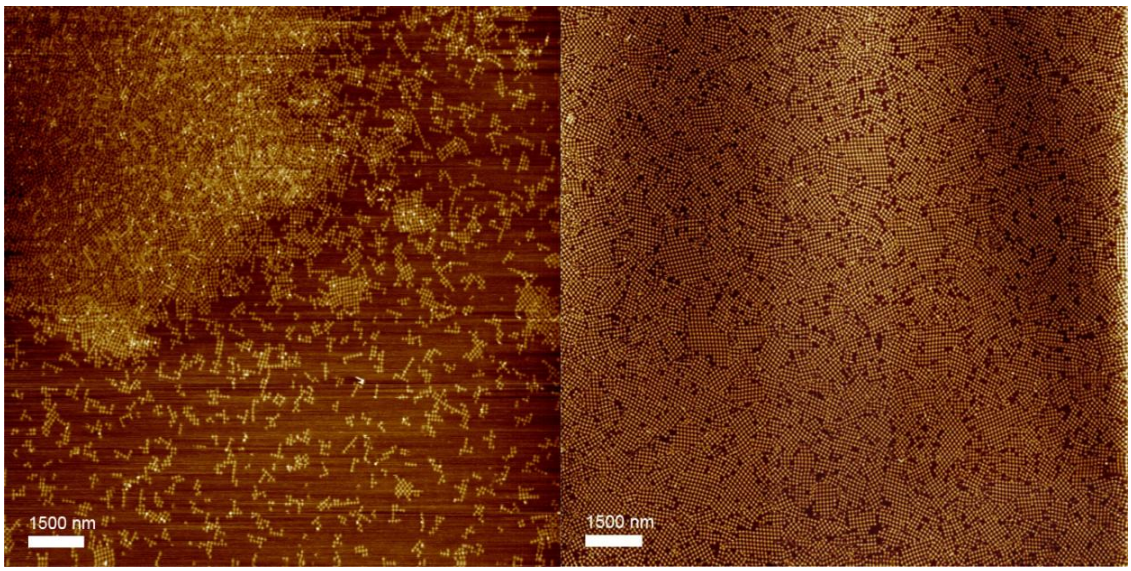

Figure 10. From literature, ST origami fishnet lattice on mica surface utilizing blunt-end interactions between origami [6]. Both samples have magnesium concentration of 12.5 mM. On the left, a sample with sodium concentration of 130 mM. On the right, a sample with sodium concentration of 250 mM. Adapted with permission from [6]. © 2014 Angewandte Chemie.

Few interesting known properties of the ions introduced in section 2.2.1 include the commonly used ability of nickel to fix or freeze origami structures on mica, whereas magnesium is mostly used for origami adsorption. Most likely, this ability arises from the stronger origami binding ability of nickel due to the increased amount of binding sites in DNA as discussed in section 2.1. Also, an ion combination of calcium and sodium was found to have the highest lattice order on mica [6]. Keeping these ions in mind, factors having an impact on the lattice assembly kinetics in addition to the attachment scheme (type and number of interactions between structures), ionic conditions (ions and their concentrations) and substrate surface roughness include incubation time, origami concentration and temperature. All of these factors are studied for efficient and optimized assembly of a fishnet lattice out of the blunt-ended ST origami on top of silicon surfaces. Although, it is relatively easy to create DNA

origami lattices on mica already with low magnesium concentrations (12.5 mM), lattice optimization on the silicon surface is required since mica is unsuitable for further lithographic processing required for DALI and therefore the creation of metamaterials (see sections 2.6 and 2.7).

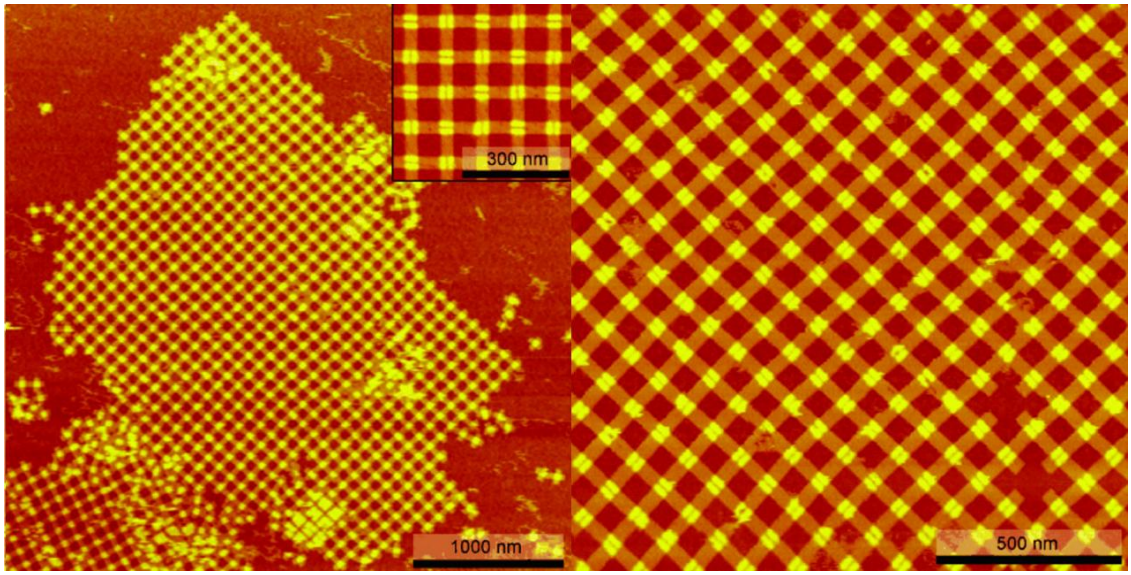

Figure 11. A fishnet lattice with dimensions of around 2 µm×3 µm were assembled using sticky-ends and two alternating forms of the ST origami [9]. Lattices of sizes up to 10 µm can be achieved, although, the lattice in the figure is one of the cleanest obtained using this approach. Adapted with permission from [9]. © 2011 Angewandte Chemie.

2.5 Surface treatment

To utilize other surfaces for DNA origami lattice assembly, *e.g.*, silicon they might require additional treatment to gain a negative surface charge. Two type of methods are introduced, which are both commonly used by the microelectronics industry to clean organic compounds and photoresist materials from silicon wafers and for lithographic etching [60].

As discussed in section 2.3, silicon wafers need to be treated hydrophilic to utilize them in DNA origami lattice assembly. Commonly, this is done using oxygen (O_2) plasma treatment with reactive ion etching (RIE), which is a dry-etching technique. RIE generates a reactive plasma by an electromagnetic field under vacuum. The reaction chamber is filled with a gas, in this case O_2, out of which the plasma is created and the wafer is bombarded with high-energy ions of the plasma. The

addition of hydroxyl (-OH) groups results in a negative surface charge on the wafer.

Another approach for a similar type of surface treatment for silicon or other substrates is the piranha treatment, which is a wet-etching technique. A transformation of the original reaction with similar features is referred to as the basic piranha that uses a mixture of ammonium hydroxide (NH_4OH) and hydrogen peroxide (H_2O_2) to clean and treat a surface hydrophilic by hydroxylation (addition of -OH groups) [61, 62]. Most organic matter is decomposed as the piranha mixture is a strong oxidizer.

2.6 DNA-assisted lithography (DALI)

DNA-assisted lithography (DALI) is a fabrication method developed by Shen *et al.* to transform the shapes of DNA origami deposited on a silicon surface into metallic nanostructures [8]. The original DALI method consists of in total eight lithographic steps, which are demonstrated in figure 12. In step one, either a transparent sapphire (Al_2O_3) or a silicon nitride (Si_3N_4) wafer is chosen as the base substrate for the process. Although, some adaptations of DALI, *e.g.*, the biotemplated lithography of inorganic nanostructures (BLIN) also enable the use of transparent substrates like glass [63]. Silicon nitride is cheaper out of the two DALI substrates which is why it is used to optimize the steps of DALI. Switching to the transparent sapphire substrate provides an advantage for optical measurements [8]. The chosen substrate wafer is cut into smaller chips which are cleaned with acetone and isopropanol (IPA). In step two, a layer of amorphous silicon (α-Si) is grown on the chips using plasma-enhanced chemical vapour deposition (PECVD). In step three, the surface of the silicon chip is treated with O_2 plasma using RIE, as discussed in section 2.5, and the DNA origami are deposited on the surface. The origami deposition is done by drop-casting the solution on the surface of the chip under 100 mM $MgCl_2$ concentration. In step four, a layer of silicon dioxide (SiO_2) is grown selectively everywhere else except on top of the origami using CVD [64], leaving behind approximately 10 nm deep, origami-shaped holes. SiO_2 is grown in 50 % humidity with a reaction between teraethyl orthosilicate (TEOS, $Si[OC_2H_5]_4$), ammonium hydroxide (NH_4OH) and the Si wafer. The reaction takes the form [64]

$$Si[OC_2H_5]_4 + 2H_2O \xrightarrow{NH_3} SiO_2 + 4C_2H_5OH. \tag{2}$$

In some cases the SiO_2 can slightly grow on top of the origami. This unwanted

growth can be removed by a short selective etching process with RIE. Etching refers to the selective removal of a material from a wafer, which is based on plasma enhanced evaporation of the etched material when reacting with the chosen gases of the plasma. To achieve a selective etch of SiO_2, reaction gases of CHF_3 (25 sccm = 25 cm^3/min) and Ar (25 sccm) should be used for the plasma [8]. In step five, the silicon layer is etched away through the origami shaped holes using isotropic RIE etching. The base substrate stops the isotropic etch as it is a harder substance. Selective Si etching is achieved by using a mixture of O_2 (8 sccm) and SF_6 (100 sccm) gases [8, 65]. The silicon etching is achieved due to the creation of mainly SiF_4 [65, 66].

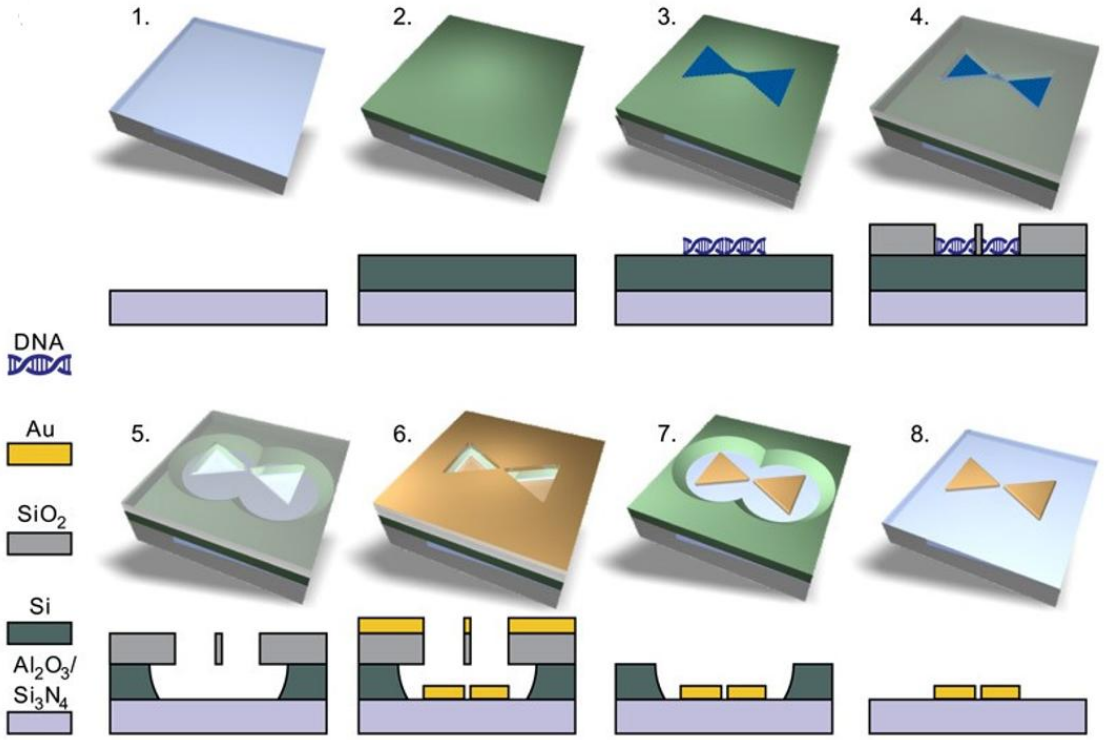

Figure 12. Steps for the original DNA-assisted lithography (DALI) method. Step 1: Base substrate, either (Al_2O_3) or (Si_3N_4), is chosen and cleaned with acetone and IPA. Step 2: An α-Si layer is grown on the substrate using PECVD. Step 3: Origami is deposited on the silicon after O_2 plasma treatment with RIE. Step 4: An SiO_2 layer is grown selectively on the silicon. Step 5: The α-Si layer is etched away through the origami shaped holes with RIE. Step 6: A gold layer is deposition with PVD in ultrahigh vacuum. Step 7: SiO_2 layer is removed by HF based lift-off. Step 8: Rest of the α-Si is removed by RIE etching. Adapted with permission from [8]. © 2018 Science Advances.

Because of the isotropic nature of the etching process, removal of material also in

the lateral direction from the surface, some level of undercut does occur. Therefore, some of the amorphous silicon is also etched away from under the SiO_2 mask, leaving behind circular holes around the origami, which become visible when imaged with the scanning electron microscope (SEM). Too much undercut can leave small details in the mask collapsed, losing information in the wanted shapes. To avoid undercut, more anisotropic etch profiles could be achieved through the use of inductively coupled plasma reactive ion etching (ICP-RIE) [67]. For ICP-RIE, the plasma is created using a radio frequency (RF) powered magnetic field [68]. Also, a separate RF bias is induced near the wafer to acquire directional electric fields for a more anisotropic etch profile [67, 68]. In step six, a layer of gold is grown using physical vapour deposition (PVD) under ultrahigh vacuum. In step seven, the SiO_2 layer is removed using a hydrogen fluoride (HF) based wet etching lift-off process. In step eight, the rest of the α-Si is removed by RIE etching. In the end, we are left with origami shaped gold nanostructures on the base substrate, which can be imaged using the SEM.

2.7 Optical metamaterials

In definition, a metamaterial is any type of material having a property that does not naturally occur in materials encountered in nature [1]. Rather than deriving new features from the base materials, optical metamaterials typically acquire new properties as a result of newly designed structural components on the nanoscale. Electromagnetic or sound waves can be manipulated by creating materials with new type of shapes, sizes, orientations and arrangements, which can influence the absorbance, blocking, bending or enhancement behavior of the waves [2]. Although, the fabrication and control of features in small length scales in general remains a challenge.

Mainly, the new properties arising from metamaterials are obtained through negative permittivity and/or the negative permeability of the material [1]. Especially, metamaterials exhibiting both of these properties resulting in a negative refractive index for certain wavelengths have gathered special attention [2]. A negative-index metamaterials or NIMs would enable the production of superlenses, capable of imaging features and fine structures much smaller than the wavelength of light [3]. Other exciting applications for metamaterials include the optical camouflage and invisibility metacoatings, acoustic metamaterials for the purpose of medical imaging and cancer

therapy, artificial magnetism, superior antennae, optical nanolithography, nanocircuits, optical filters, seismic applications, sensors, high-frequency communication and many more [1–3].

As metamaterials are typically made from metals, at least two types of metasurfaces can be produced with the metallized fishnet lattice created with our chosen ST origami. A layered yellow-light negative-index metamaterial could be formed with the fishnet mold by layering two 43 nm thick layers of perforated silver (Ag) between 45 nm thick layers of alumina (Al_2O_3) [69]. With small modifications to the ST origami design a broadband metamaterial filter could also be achieved [70].

2.8 Atomic force microscopy (AFM)

Atomic force microscopy (AFM) is an imaging technique developed for imaging structures of nanoscale dimensions that conventional, optical microscopes are unable to reach due to the optical diffraction limit. The AFM technique can also be referred to as scanning force microscopy (SFM) and is a type of scanning probe microscopy (SPM) [71]. A simplified configuration of an AFM is presented in figure 13. In AFM imaging, a sample is scanned by detecting the interactive forces between an ultrasharp tip (or probe, 3) and the sample surface (4), which deflects the cantilever (2) according to Hooke's law [72]. The AFM cantilevers are typically manufactured out of either Si or Si_3N_4 and have a tip radius on the order of nanometers [72]. The measured height with AFM is always accurate, but due to the finite, nominal radius of the tip, other dimensions of the imaged structures can get elongated. The sample surface is scanned line by line to create a contour plot of the wanted features. Ultimately, resolutions of even a single atom can be achieved [72]. The height differences on the surface can be converted into electrical signals by reflecting a laser (7) from the tip cantilever into a photovoltaic detector (8) [71]. Other sample properties like the modulus, dissipation, adhesion and deformation can also be measured, *e.g.*, by utilizing the quantitative nanomechanical mapping (QNM) mode [71]. The deflections of the cantilever, due to interactive forces between the sample and the tip, are mapped as displacement of the laser location on the photovoltaic detector [71]. The electric signal gained is typically set to a constant value that is maintained through a feedback loop [71]. This corresponds to a constant probing distance on the sample or a constant force that is maintained between the tip and the sample. All of the small, precise movements of the probe are achieved through

the use of piezoelectric materials incorporated in the tip holder (1) or sometimes in the sample holder [73].

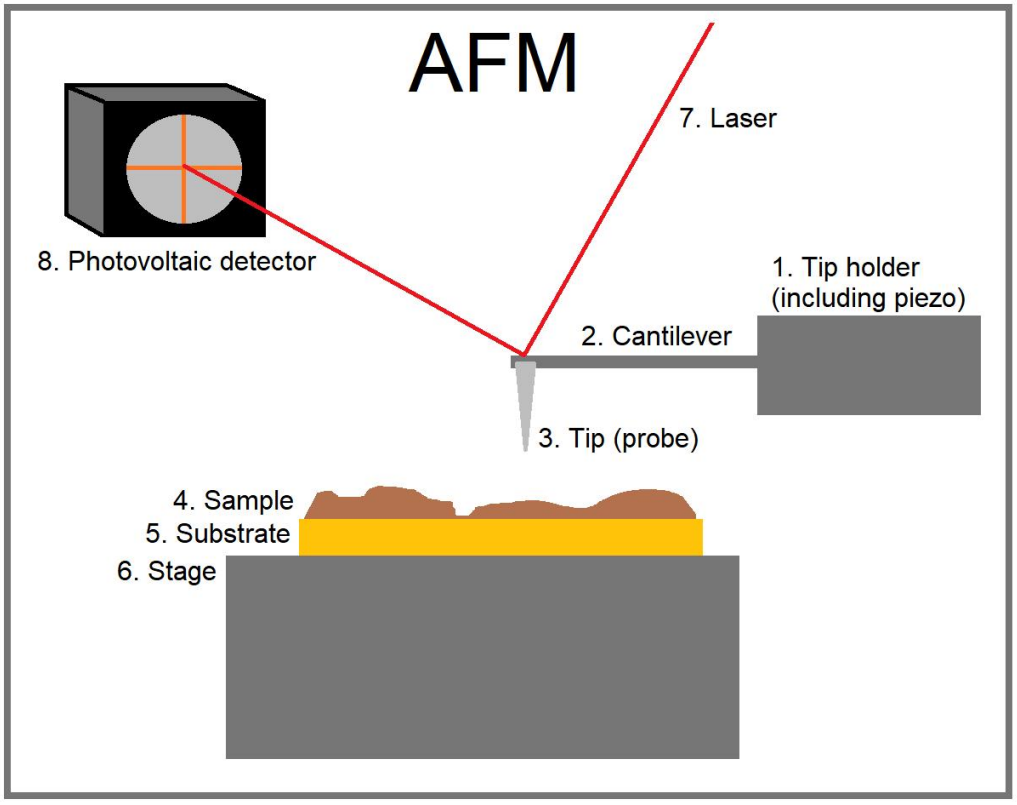

Figure 13. A simplified AFM configuration. A typical AFM setup includes: 1. A tip holder containing the piezoelectrics. 2. A cantilever of the tip. 3. The tip (or the probe). 4. A sample to be scanned. 5. A Substrate on top of which the sample was prepared, *e.g.* mica (see section 2.3). 6. The stage that holds the sample. 7. A laser that is reflected off the cantilever. 8. A photovoltaic detector.

Generally, three different approaches to AFM imaging exist: the contact mode, the tapping mode and the non-contact mode. The choice for a proper mode is dependent on the imaged sample. In contact mode, the tip is dragged across the surface and the contour is measured either from the deflection of the cantilever or the feedback signal [71]. Contact mode is mainly used for samples expressing overall repulsive forces, *e.g.*, hard solid materials to avoid damage to either the sample or the tip. Tapping or intermittent contact mode was developed to avoid the tip from getting damaged or sticking to more softer samples during imaging. The detection of short range forces without a direct long term contact is achieved by oscillating the cantilever up and down near its resonance frequency [72]. Experienced electrostatic

and Van der Waals forces as well as dipole-dipole interactions near the sample are able to change the amplitude and frequency of the oscillating signal that is otherwise kept constant [71]. The PeakForce tapping mode for AFM allows the control of the maximum normal force, *i.e.*, the peak force that is applied on the sample, instead of just controlling the damping of the cantilever oscillation [74]. Control over the peak force enables the determination of other useful surface properties with the QNM mode as mentioned above. Non-contact mode is the preferred approach for imaging fragile biological samples and organic thin films as the tip is never in direct contact with the sample. Again, the cantilever is oscillated at the resonant frequency which is affected by any long-range forces, *e.g.*, Van der Waals interactions resulting from the sample [71]. One non-contact variant of AFM is the kelvin probe force microscopy (KPFM) or scanning kelvin probe microscopy (SKPM) that measures the contact potential difference (CPD) between a tip and the sample which are capacitively coupled together [75]. This approach can be used to map the work function or surface potential of a sample [75].

Liquid AFM imaging is also possible using a specialized holder and tips [76]. A liquid pillar is formed between the sample and the liquid holder leaving the probe inside a liquid column. Sealed liquid holders also exist to avoid drying of the liquid pillar, which would result in losing of the AFM signal required for imaging [76]. Most likely, the liquid used to form the pillar between the sample and the tip holder has a different refractive index compared to ambient air, resulting in refraction of the laser beam at the edge of the liquid. Therefore, alignment of the laser on the cantilever needs to be adjusted manually when imaged in liquid.

Although, some imaging techniques are significantly faster in taking images, *e.g.* the SEM, they usually require complicated sample preparation procedures and only allow imaging of specific types of samples [72]. Also, samples containing biological compounds often present a challenge due to the harsh preparation protocols and imaging environments. In conclusion, AFM imaging, both in dry and liquid states, enables the direct, high-resolution imaging of a plethora of different types of samples with nanometer and atom sized features in reasonable time and costs.

3 Methods and materials

The method section begins with general details about the materials and methods used in this study. More detailed versions of the sample protocols used in results sections 4.2, 4.3 and 4.4 are given in sections 3.1, 3.2 and 3.3, respectively. The details for the blunt-ended, twist-corrected Seeman Tile (ST) design can be found in the following article [6]. The circular, single-stranded M13mp18-scaffold that was used to fold the ST origami was ordered from Tilibit Nanosystems (Munich, Germany). In total, the scaffold consisted of 7249 base pairs (type p7249) and the concentration of scaffold in the ordered solution was 100 nM. The staple strands for the TC-ST design were ordered from ThermoFisher (Waltham, Massachusetts, USA) and for the NTC-ST from IDT (Coralville, Iowa, USA). Each oligo staple had a concentration of 100 µM and was ordered in TE buffer, frozen and desalted. In total, there are 210 oligo staples in the design out of which 24 are used to form the edges of the arms of the origami structure.

For convenience, all of the used chemicals are listed in table 3 in appendix A. The ST origami was folded in 1×TAE/12.5 mM $MgCl_2$ buffer where TAE is a mixture of Tris base, Acetic acid and EDTA. The recipe for preparing a 50×TAE buffer can be found from this article [77]. Sodium hydroxide in table 3 was used to set the pH of TAE to 8.0. As the folding procedure has evolved during the study, details for the folding mixtures, the thermal annealing protocol for the PCR thermocycler as well as purification details are given in the following sections. Also, the method for treating the silicon surface to have it negatively charged was changed after section 4.2, since both methods give very similar results. Details about these protocols are given in the later method sections.

The origami concentrations were measured using Thermo Fisher Scientific NanoDrop One C Microvolume UV-Vis Spectrophotometer. The device was set to measure the concentration of either double- or single-stranded nucleic acids and blanked using the origami folding buffer (1×TAE/12.5 mM $MgCl_2$). A volume of 1-2 µl of solution was pipetted on the measurement stage and at least three individual measurements were taken for the same droplet. The measured values given in ng/µl

were averaged together and the average was converted into the nanomolar units (nM = nmol/l) using the following conversion,

$$\frac{(\text{concentration in ng/µl}) \cdot 10^{-6}}{660\,\text{g/mol} \cdot 7249} = \text{concentration in nM}, \tag{3}$$

where 660 g/mol is the assumed average molar mass per base. Mica substrates used in the experiments were purchased from Caspilor Aktiebolag and had the highest quality grade V1 (Ted Pella Inc, Redding, California, USA). The round mica chips were glued on glass slides to ease the sample preparation. Mica samples were prepared by pipetting 10 µl of folded, unpurified origami solution straight on the freshly cleaved mica surface and incubated for 5 min. After the incubation on a cleanroom paper and under a glass cover, approximately 60 µl of Milli-Q H_2O was pipetted back and forth 3-4 times on the corner of the mica. Fresh water was collected and the step was repeated two more times. The washing procedure was continued by pipetting 60 µl of Milli-Q H_2O on the mica and gently tapping the liquid off the chip on the cleanroom paper (glass slide is tapped on the table in a 90° angle). Finally, the chip was dried using nitrogen (N_2) flow. Typically, origami concentrations of 3-5 nM are sufficient for mica chips, but larger concentrations can be applied.

The silicon substrates, sc-Si and SiN wafers, were acquired from Si-Mat (Viktor-Frankl-Str, Kaufering, Germany). The sc-Si wafers had an orientation of <100>, a silicon thickness of 525±25 µm, resistivity of 1-10 Ωcm, a diameter of 100 mm, had only one side polished, were P/boron doped and type SEMI standard flats. The SiN wafers had the same orientation of <100> and consisted of a 525 µm layer of silicon which was covered with 300 µm of polished SiN on both sides of the wafer. Both wafers were cut into 7 mm×7 mm pieces using a diamond cutter. Both surfaces were cleaned in ISO 5 cleanroom facilities using the following procedure. The chips were immersed in boiling acetone for a few minutes, after which the upmost side of the chips was rubbed clean with a cleanroom cotton swab. The chips were turned around and they were boiled in acetone again for a few minutes. The second side of the chips was then cleaned with the cotton swab and the acetone was boiled again. In total, the chips should be immersed in boiling acetone for approximately 15 min. Next, the chips were rinsed with room temperature (RT) acetone and immersed

into fresh isopropanol (IPA). The chips in IPA were treated with the FinnSonic M3 Ultrasonic cleaner (Lahti, Finland) in 30 °C for 3 min. Finally, the chips were dried using N_2 flow.

A layer of 50 nm of amorphous silicon was grown on the cleaned SiN chips using PECVD with Oxford Plasmalab 80 Plus (Abingdon, Oxfordshire, England). The growing process treats the surface with a gas flow of 500 sccm of 5% SiH_4 in 95% Ar with a pressure of 100 mTorr, RF power of 15 W, temperature of 250 °C for a duration of 1.5 min.

Samples were imaged using the Bruker Dimension Icon AFM combined with the Nanoscope V Controller software. The PeakForce QNM imaging was applied for both liquid and air imaging. Samples/line values between 256-768 were used for scanning sizes of 1-20 µm. The peak force setpoint was kept at 1 nN, the peak force amplitude at 150 nm and the peak force freqency was 2 kHz. ScanAsyst air silicon tips on a nitride cantilever from Bruker (Billerica, Massachusetts, USA) were used for AFM imaging in air with a cantilever spring constant of 0.4 N/m and tip radius of 5 nm. For liquid imaging the ScanAsyst liquid (nitride coated silicon tips on a nitride cantilever) and liquid+ (silicon tips on a nitride cantilever) from Bruker were used with a cantilever spring constant of 0.7 N/m. Next, the more detailed sample preparation protocols for each result section are given.

3.1 Sample protocol for dry samples in section 4.2

Details for calculating the amounts of scaffold, oligo staples in the middle of the origami and edge staples on the edges of the origami structure for the relative ratio of $1 : 1.4 : 5.6$ and a concentration of 20 nM are given in appendix B. The recipe for the folding mixture is given in appendix C. The annealing temperatures and times for the pcr machine are given in appendix D. Our folding protocol was adjusted based on the protocol used in Aalto university [78]. The theoretical maximum concentration for the folded origami solution is 20 nM.

The spin-filtering purification technique was used to get rid of excess staple strands in the folded origami solution [79]. The purification selectivity is achieved by using Millipore Amicon Ultra YM-100 500 µl centrifugal filters that have a molecular weight cut-off at 100 kDa. A volume of 100 µl of folded origami was mixed with 400 µl of folding buffer (1×TAE/12.5 mM $MgCl_2$) in a filter unit. The mixture was centrifuged with 14 000 rcf for 3 min with Heraeus Megafuge 16 centrifuge from

Thermo Scientific. The flowthrough was discarded and 400 µl of fresh folding buffer was added in the filter. The centrifugation and addition of folding buffer was repeated three more times with an increased spinning time of 5 min for the last round. After the last round, the filter was turned upside down in a fresh collection tube and centrifuged for 2 min with 1000 rcf. The volume of the collected solution was brought back to around 90 µl, taking into account the reported yield of the purification method of approximately 90 % [80] to obtain a purified origami solution of about 20 nM concentration. Finally, the precise origami concentration for the purified solution was measured as described in the previous section.

The sc-Si and α-Si chips were treated with O_2 plasma using RIE with Oxford Plasmalab 80 Plus right before origami deposition. An O_2 flow of 50 sccm was ran for 20 min with a pressure of 40 mTorr, RF power of 200 W and temperature of 30 °C. The sample liquid was pipetted on the treated chips usually within 30 min after the treatment has ended. The total sample volume should be from 10 µl to 20 µl, depending on the length of the incubation time to avoid drying of the sample.

A volume of 10 µl is still sufficient for incubating samples under a glass cover that have an incubation time under one hour. Otherwise the sample volume was increased to 20 µl to avoid drying of the sample during incubation. The concentration of origami was fixed to 10 nM using the folded and spin-filtered ST origami solution (20 nM). The wanted ionic conditions were set for the sample by pipetting the required amounts individually from 0.5-2 M concentrated salt solutions ($MgCl_2$, $NiCl_2$, $CaCl_2$, NaCl, KCl, LiCl). The salt solutions were first combined in a 1.5 ml eppendorf tube and 1×TAE was added to adjust the volume to the final target volume. The origami was mixed last and the ready sample solution was pipetted shortly on the treated Si chip. After incubation on top of a cleanroom paper and under a glass cover, the samples were washed by pipetting a volume of 45 µl of Milli-Q H_2O back and forth on the corner of the chip approximately 5 times (or 10 times for longer washing cycles). This step was repeated with fresh Milli-Q H_2O for 3-5 times. Longer washing cycles were used when experimenting with high ion concentrations (over 400 mM) and especially samples containing nickel.

Two-step incubation samples are presented in sections 4.2.2 and 4.2.3. Two-step incubation for samples with two different ions includes incubating the origami under the influence of the first ion for X amount of minutes. The second ion was introduced by adding a required concentration on the sample droplet and incubating for a period

of Y minutes. Also, some concentration of the first ion needs to be present in the added liquid to keep its concentration fixed on the sample. Afterwards, the sample was washed normally, as presented in the previous paragraph. Two-step incubation for samples experimenting with three ions, works similarly. These kind of protocols are referred to as "wash" samples, where the name of the ion introduced last is used in combination with the word wash, *e.g.*, nickel wash. Two of the ions (or all except the last ion) were introduced first and incubated for an amount of X minutes. The ion doing the "washing" is introduced last and incubated for a period of Y minutes.

The cryogenic electron microscopy (cryo-EM) samples introduced in section 4.2.3 were prepared at Aalto University by Ashwin Natarajan using the following sample procedure. A sample with a 50 mM magnesium, 5 mM of nickel and 250 mM of sodium concentration was mixed a day before the cryo-EM imaging following the steps described above. A volume of 5 µl of this sample was dropped on a plasma cleaned R3.5/1 quantifoil grid in a Leica plunger, which was kept at 22 °C and 90 % relative humidity. After blotting for 2.8 s, the sample was immersed immediately into liquid ethane. The grids were imaged using a JEOL JEM-3200FSC field emission cryogenic transmission electron microscope (cryo-TEM), which was operated at 300 kV in bright field mode with an Omega-type Zero-loss energy filter.

Also, a tilt series was done in cryo conditions for the same sample using the Serial EM-software package. The tilt series was acquired by tilting the sample between angles of $-69°$ and $69°$ with an increment step of 2.5-3°. The low-dose mode with an average e-dosage of 1 e-/A2 for 15kx magnification and 2 e-/A2 25kx magnifications was used. Alignment of the tilt series was done using patch tracking in IMOD and was binned twice. Reconstruction for the tomogram was acquired using Simultaneous Iterative Reconstruction Technique (SIRT) over 10 iterations. For image analysis and video generation the UCSF ChimeraX 1.2.5 was used.

3.2 Sample protocol for liquid imaging samples in section 4.3

The thermal annealing procedure was simplified and applied for the samples introduced in section 4.3. The procedure was started from 80 °C and the folding time for each 1 °C drop was 16 min until 20 °C was reached. After the sequence was finished the product was stored at 10 °C, until the sample was purified. A volume of 100 µl

was folded by combining 10 µl of 10×TAE/150 mM $MgCl_2$ buffer, 80 µl of staple master mix (equal amount of each staple mixed together, ∼0.5 µM per oligo) and 10 µl of M13mp18 scaffold in a PCR-tube. The ratio between scaffold and all staples was 1 : 38.

Also, the spin-filtering purification protocol was optimized. 1-3 PCR tubes of folded origami (100 µl-300 µl) was combined with 200 µl-400 µl of Milli-Q H_2O inside a Millipore Amicon Ultra YM-100 centrifugal filter so that the total volume of solution in the filter was 500 µl. The solution was shaked briefly by hand and spinned with 8867 rcf (9000 rpm with Thermo Scientific Fiberlite F15-6x100y Rotor) for 5 min (Heraeus Megafuge 16 centrifuge, Thermo Scientific). The flowthrough was discarded, 450 µl of Milli-Q H_2O was added back in the filter and after a brief shake the solution was spinned again with 8867 rcf for 5 min. This step was repeated in total three times. After the last spin, the filter was turned upside down into a fresh tube and a collection spin with 109 rcf (1000 rpm) for 2 min was done. Since this protocol uses Milli-Q H_2O for purification instead of storing buffer, to avoid higher concentrations of magnesium inside the filtered solution, a buffer exchange needs to be performed as a final step. Amount of the final collected volume from the filter was divided by nine and the specified volume of 10×TAE/125 mM $MgCl_2$ buffer was added in the purified solution in order to adjust the origami solution to 1×TAE/12.5 mM $MgCl_2$. The final concentration of origami was measured as normal with the Thermo Fisher Scientific NanoDrop One C Microvolume UV-Vis Spectrophotometer as described earlier, which was usually around 20-40 nM for successful purification.

To treat the silicon chips for origami deposition the basic piranha solution was prepared by pipetting 5 ml of Milli-Q H_2O, 1 ml of 25 % NH_4OH and 1 ml of 30 % H_2O_2 into a glass container inside a laminar cabinet [61]. The glass container was placed on a hotplate set to 200 °C under a glass cover. When the solution started to boil, the heat was decreased to 150 °C and the chip was placed in the solution by gently pushing it fully under the surface using tweezers. A timer was set to 15 min and the chip was kept fully immersed in the basic piranha solution during the whole procedure. After 15 min the chip was taken out of the piranha solution and immersed for a few seconds in fresh Milli-Q H_2O. The chip was immersed into a second fresh Milli-Q H_2O solution for a few seconds and afterwards dried using N_2 flow. The chip was used shortly after the surface treatment, usually within 30 min of drying the chip.

A volume of 10-20 µl of sample solution was prepared by mixing nine parts of the purified origami solution (diluted with 1×TAE/12.5 mM $MgCl_2$ buffer) with one part of buffer having ten times stronger ionic concentrations than what were wanted on the final sample solution (10× buffer). The origami were stored in 1×TAE/12.5 mM $MgCl_2$ buffer and these conditions should always stay present unless the storing buffer was completely switched during spin-filtering purification. As an example, preparing a sample from 1×TAE/12.5 mM/1 M NaCl, will bring the sodium concentration to 100 mM when mixed with origami. Furthermore, a mixing buffer of 1×TAE/37.5 mM/2.5 M NaCl will set the magnesium concentration to 15 mM and sodium concentration to 250 mM. The origami tile concentration was usually fixed to 10 nM in the final sample solution.

When the sample solution was mixed, it was rapidly pipetted on the treated silicon substrate and incubated as before under a glass cover. The sample washing procedure was made more gentle to avoid detaching any loosely bound origami. The incubated chip was tilted at a 45° angle, supported on a cleanroom paper and a volume of 60 µl of Milli-Q H_2O was continuously streamed down the chip from the middle of the top edge. Finally, the chip was dried gently using a soft N_2 flow. The pressure of the flow should be as low as possible, but high enough to not leave any coffee stain resembling drying marks on the chip.

Sample solutions for the liquid AFM imaging were prepared as described above for dried samples. The sample should be mixed right before imaging. If the sample starts drying during imaging, more of the same sample solution can be pipetted carefully on the liquid column (tip needs to be withdrawn from the surface when liquid is added).

3.3 Sample protocol for temperature controlled samples in section 4.4

The experiments in section 4.4.1 were performed using the Asylum Research Cypher ES Environmental AFM (Abingdon, Oxfordshire, England). For the temperature controlled liquid AFM experiments, a solution with a total volume of 100 µl was prepared. A volume of 90 µl of origami solution was diluted with 1×TAE/12.5 mM $MgCl_2$ to obtain a final origami concentration of 12 nM. The diluted origami solution was mixed with 10 µl of the 10× buffer (1×TAE/12.5 mM $MgCl_2$/1.5 M NaCl). The

final sample solution was injected on the chip and AFM liquid imaging was started using a 5 Hz scanning frequency per line. The imaging was started from 25 °C and increased in increments of 5 °C. One temperature was held for approximately 1678 seconds for the same sample, after which the temperature was increased by 5 °C.

For dried samples, the sample solution was prepared by combining the folded ST origami with the 10×Na buffer (*e.g.*, 1×TAE/12.5 mM $MgCl_2$/3 M NaCl) so that the final origami and sodium concentrations are those wanted. The final sample liquid should have a total volume of 20 µl, which was filled using 1×TAE/12.5 mM $MgCl_2$ buffer if needed, to keep the magnesium and TAE concentrations the same as in the storing buffer. The sample solution was injected on a basic piranha treated (15 min, details given in section 3.2) silicon chip with dimensions of 7 mm×7 mm and the chip was sealed in a 3 cm petri dish using parafilm.

The temperature controlled dried samples were incubated inside an environmental chamber from Weiss Technik (Reiskirchen, Hessen, Germany) for used temperatures in the range of 30-50 °C and humidity between 30-35 %. After the incubation period the sample was taken out of the petri dish and a volume of 5 µl (per 20 µl of origami solution) of 100 mM $NiCl_2$ was pipetted on the chip for 30 s, bringing the final nickel concentration down to 20 mM.[9] After 30 s the chip was tilted in an 45° angle, supported on a sheet of cleanroom paper, and a volume of 100 µl of Milli-Q H_2O was pipetted in a continuous flow from the top edge of the chip through the sample surface. This tilted washing was repeated in total three times and dried afterwards using gentle N_2 flow. The pressure of the N_2 flow should be high enough to not leave coffee stains on the chip when the liquid dries, but gentle enough to leave behind as many origami as possible. Occasionally, incubating multiple samples inside the same petri dish might lead to drying of some of the chips before nickel fixing and sample washing was performed. Therefore, not more than three chips should be incubated together in the same dish.

[9] After the experiments presented in section 4.4, the nickel washing parameters were optimized to having a 10 mM final $NiCl_2$ concentration on the chip for 20 s.

4 Results

The experimental results are divided into four sections. The first section introduces important experimental details about the ST origami structure as it is imaged in air conditions with AFM. The second section describes experiments with the different ionic conditions and presents the most favourable ion combinations for efficient lattice assembly. The third section continues the discussion of experimenting with the ionic conditions in liquid environment (liquid AFM) to study the lattice assembly further. Also, the effect of blunt-end interaction strength on lattice assembly is studied. The fourth and final section introduces experiments with the impact of temperature on lattice formation for different number of blunt-end interactions.

4.1 Seeman tile design

The cross-tile is formed of two 100 nm long rectangles that are on top of each other and attached from the middle as discussed in section 2.2.1. This creates two smaller rectangles of double-layered helices in the middle of the origami which are clearly visible when imaged with AFM. The cross-section of a single ST origami acquired using AFM imaging in air is shown in figure 14. Also, a schematic drawing of an ST origami with rough dimensions is provided in the same figure. The M13mp18 scaffold is in total 7249 bases long. The number of bases used for all of the staple strands for the ST is 6624. There are also a few spots in the design where parts of the staples do not pair with the scaffold (*e.g.*, around the edges of the hole of the top rectangle). In total, there are 132 such bases and 14 bases in the scaffold that do not bind any staples. Therefore, 6506 bases of the scaffold are used to fold the cross-tile shape leaving 743 bases of the scaffold without a binding site. When comparing the base sequences of the staples to the sequence of the scaffold, a section with a length of 701 bases was found that is not used to bind the shape of the ST origami. This section forms a looped 'tail' of scaffold for each origami. The looped tail can be seen as a repeating unit between one pair of arms for each origami in figures 14, 16 and 17. The unused scaffold loop in the caDNAno design provided by

this article [6] was determined to be between the coordinates 0[255] and 0[256] (helix index [base index]). This corresponds to a base sequence in the M13mp18 scaffold given in appendix E.

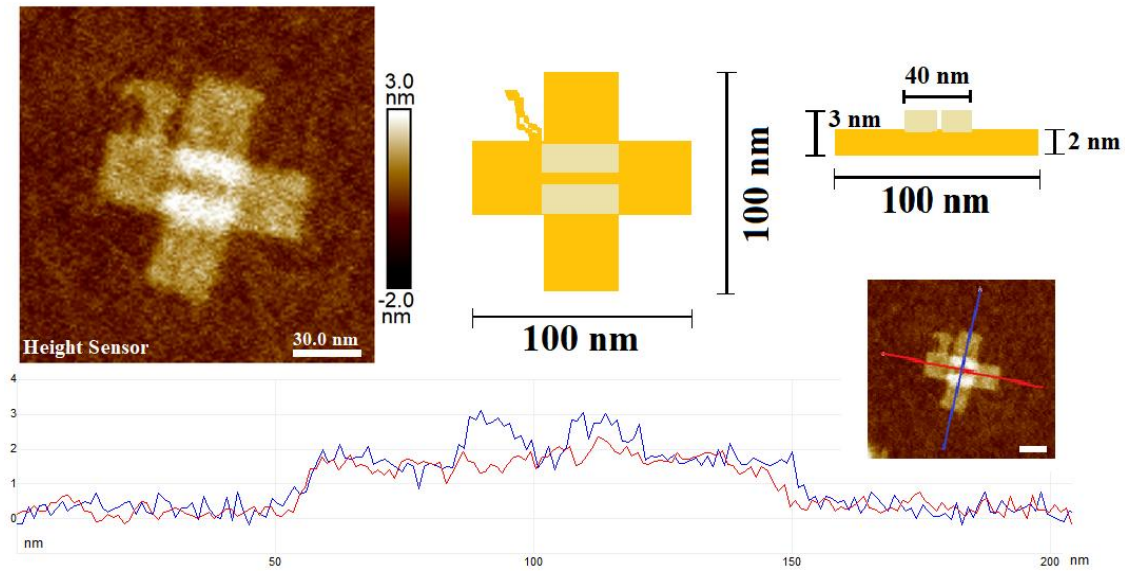

Figure 14. On the left, an air AFM image of a single blunt-ended, TC-ST origami on the sc-Si surface is presented. The cross-sectional height of an origami in dry conditions and schematic drawings of an ST origami with dimensions are presented on the right. The red and blue cross-sections correspond to the same colored lines on the AFM image on the right. The drawn loop in between one of the pair of arms on the schematic drawing presents an excess of the M13mp18-scaffold that was not used by the design. This loop has the length of 701 bases.

The later experiments done with nickel, in section 4.2.3, reveal that the scaffold overhang is especially prone to salt build-up. Nickel is a good indicator for the salt build-up property as it seems to bind DNA more strongly. Frequently, samples with nickel tend to have more highlighted, higher tails compared to samples with other ions. An example sample with 5 mM nickel concentration is shown in figure 15, where every origami has a highlighted tail with height of about 6 nm. This tail height is more than double the height of a single origami.

The ST origami are attracted to each other because of the blunt-end interactions on each arm of the design. These interactions bring the origami together and combine them into larger fishnet lattices. There seems to be a preferential orientation at which the cross-tile origami attach together when forming the lattice structures. In larger lattices the smaller rectangles in the middle of each origami often point in the

same direction. For example in figure 16, judging from the rectangles in the middle of each origami, all of the structures are attached in parallel to each other in the main lattice structure on the top of the image. This only changes in the lower left corner (marked with a blue line) where the direction is changed from horizontal to vertical (90° turn of the structure). All the origami on the left side of the blue line are still in parallel to each other. This suggests that the whole lattice is formed of two smaller lattices that came together in different orientations. This idea is strengthened when looking at the lower right corner of the same image. Two origami that are attached to each other are about to connect to the larger lattice (inside the red circle). The

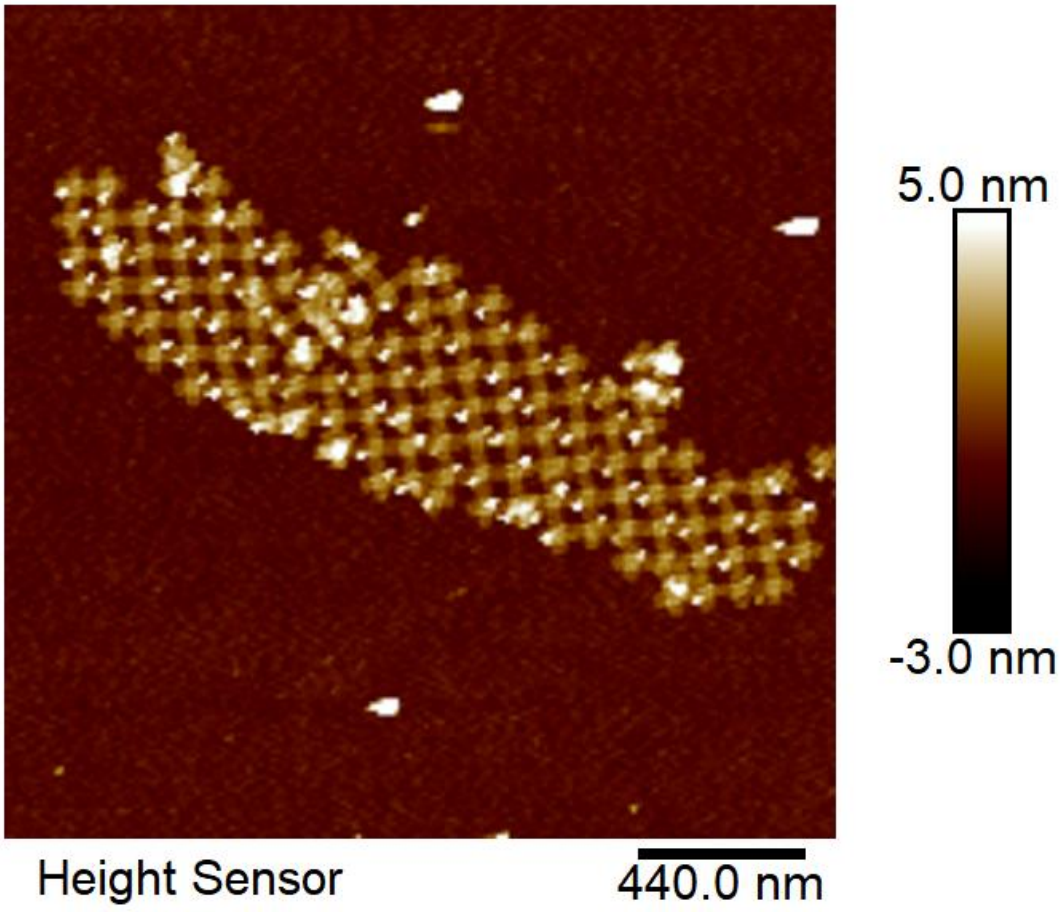

Figure 15. An example sample with 5 mM nickel concentration on sc-Si to demonstrate the build-up of nickel on the scaffold tails of the TC-ST origami.

origami can attach from every arm to each other, but inside bigger lattices one direction seems to be preferred. This kind of preferred orientation was also reported to happen on mica [6]. Further liquid imaging, discussed in section 4.3, has also

shown that the origami can reorient themselves repeatedly especially on the sides of lattices but larger, connected structures are less mobile. In conclusion, the tiles prefer a parallel orientation coming to a larger lattice structure. Most likely, this results from the preferred binding energies of certain blunt-ends in the design as discussed in 2.2.1.

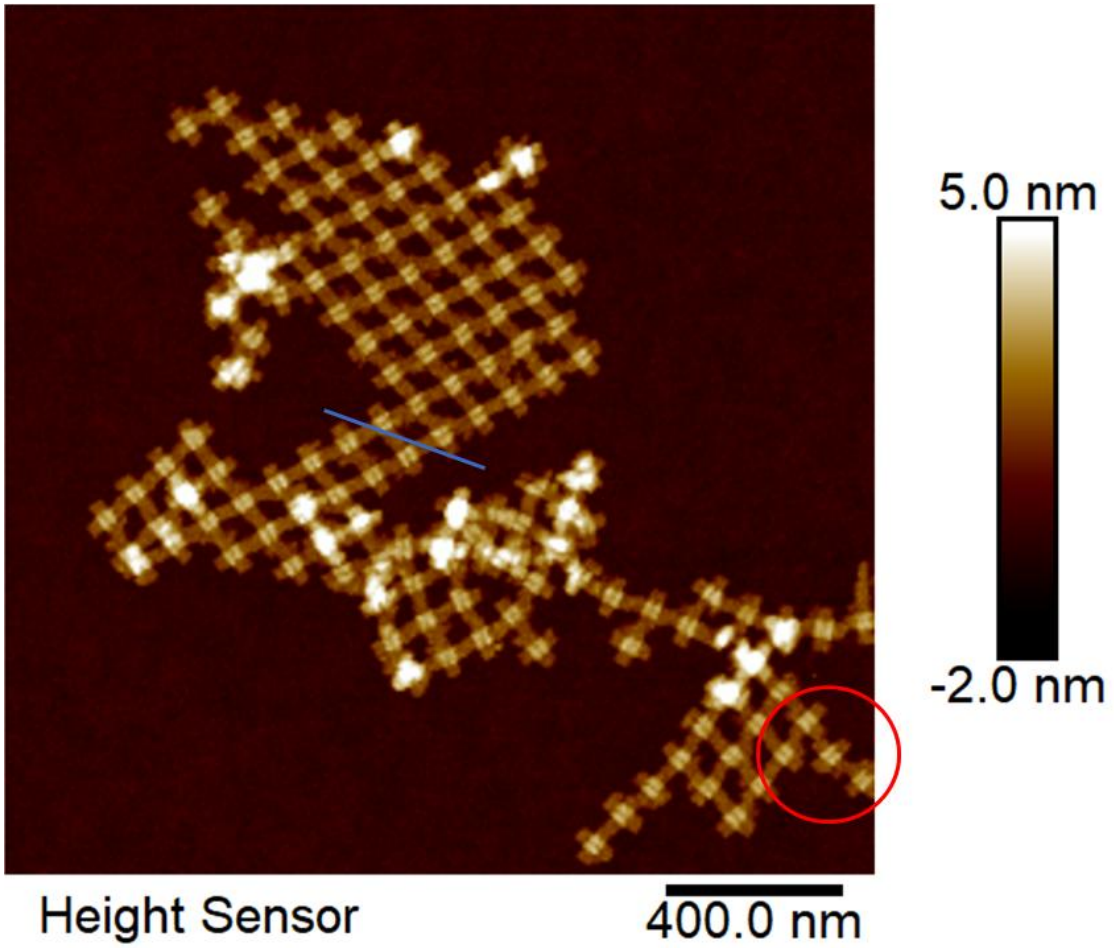

Figure 16. An example of a TC-ST origami lattice showing a typical orientation or alignment between connected origami on sc-Si. The origami concentration for this sample was 10 nM, the concentration of magnesium was 150 mM, the concentration of sodium was 100 mM and the concentration of nickel was 6 mM. The blue line indicates where lattice orientation is turned 90°. The red circle surrounds a pair of origami attaching on the bigger structure.

As demonstrated in figure 17, there is a 180° turn between neighboring origami judged by the placement of the scaffold tails in each structure, assuming the origami do not bind to the surface on different sides. As described in section 2.2.1, the twist-correction of the ST makes the structure more rigid. As discussed in the

beginning of this section, the ST design is build out of two rectangles placed on top of each other. Possibly, the slight height difference between the arms of the structure determine which arms are able to attach. This might explain why the middle rectangles are pointing always in the same direction, but it does not explain the placement of the scaffold tails between neighboring structures. Either, the symmetry of the designed blunt-end interactions at the ends of the arms of origami prefers the observed orientation or an additional attractive force arises from the scaffold overhangs guiding this type of attachments.

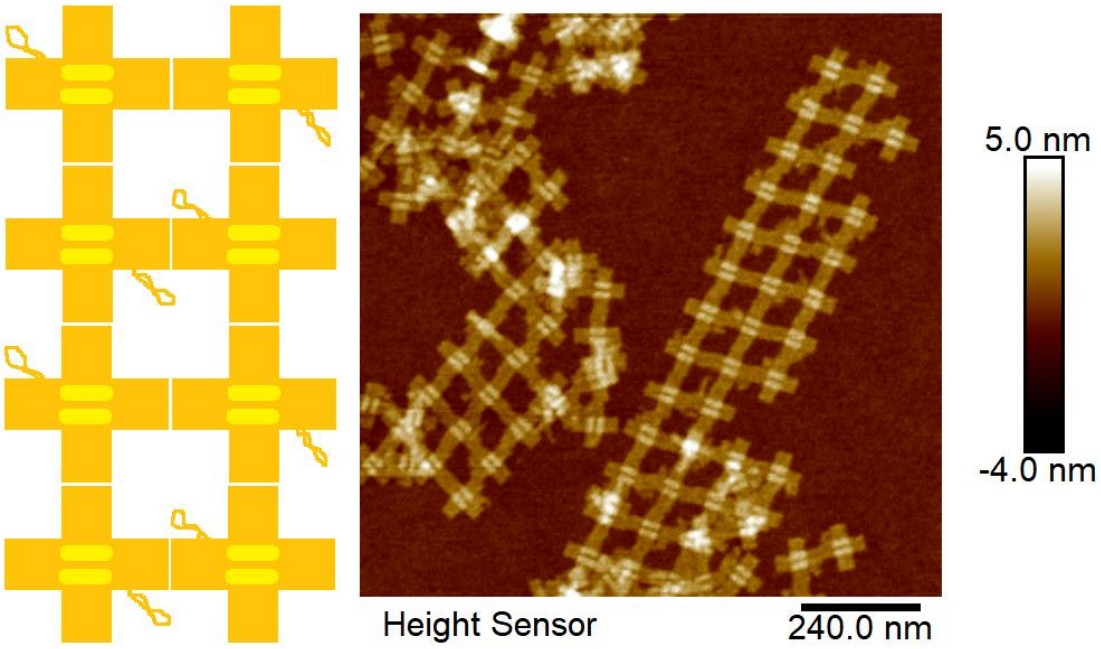

Figure 17. On the left, a schematic drawing of the orientation and placement of scaffold overhangs for a formed TC-ST origami lattice. Each structure is rotated 180° compared to the neighboring origami. On the right, a closer AFM figure of the TC-ST origami to demonstrate the unused scaffold loops or "tails" between the pairs of arms of each structure.

When looking at the leftmost lattice structure on the bottom of the AFM figure (in figure 17), it is clear that not all neighboring origami connected into lattices have a 90° angle between the arms of the origami. Apparently, the origami structures are prone to a certain level of stretch or shift in respect to each other when assembling into lattices. Unlike the 90° square-shapes between the origami drawn in the schematic in figure 17, the shapes or empty spaces inside the lattices resemble more of a diamond. Also, as shown in figure 18, the origami lattices like to grow in strings rather than growing evenly in all directions. As reported in literature, for some structures this

preferred string-like growth might arise from the twist-correction of the origami design [81]. Although, as discussed in section 4.4.2, the opposite seems to be true for the ST origami as the string-like growth gets enhanced when the NTC-ST design is imaged in liquid. Therefore, some other property of the design is able to influence the growing direction, *e.g.*, the aforementioned level difference between the two rectangles of the cross-tile or the preferred energy differences between certain blunt-end base sequences between the origami arms might be to blame.

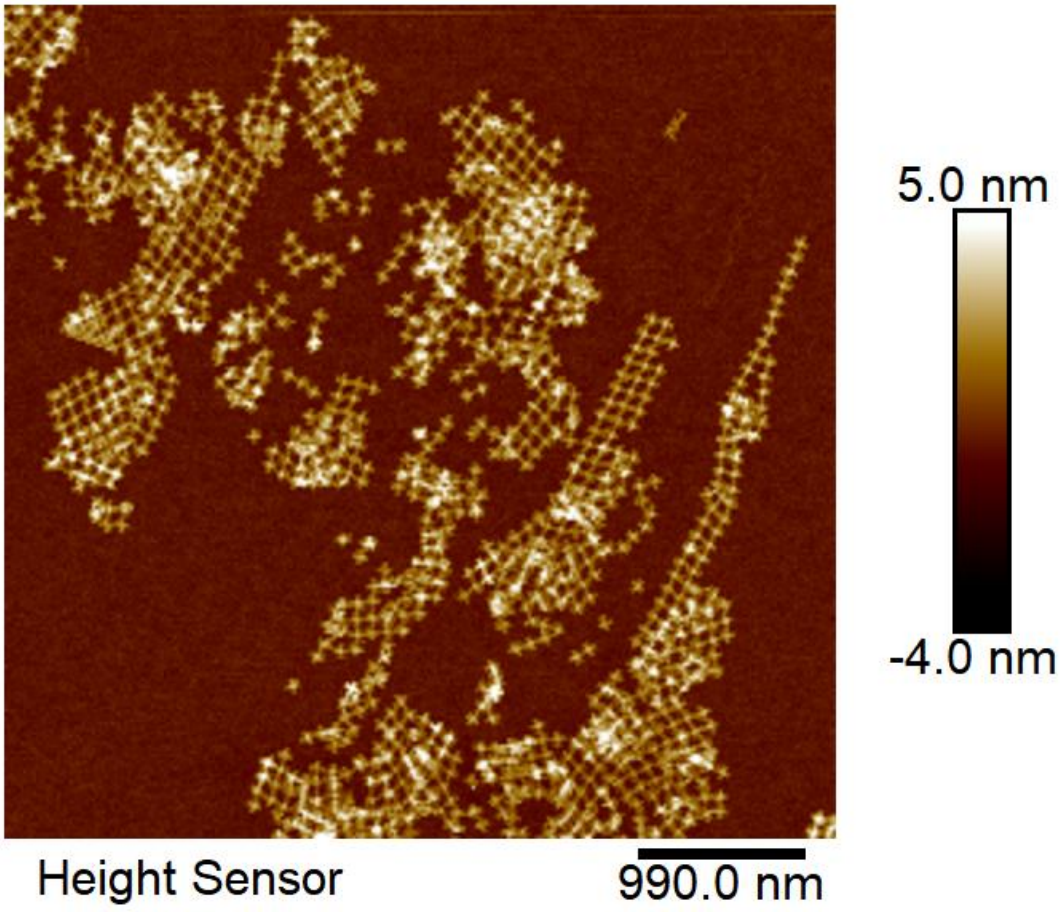

Figure 18. A representative demonstration of TC-ST lattice growth in the preferred direction, forming lines or strings of origami. The origami concentration for the sample was 10 nM, the concentration of magnesium was 150 mM, the concentration of sodium was 100 mM and the concentration of nickel was 10 mM.

The integrity of the folded origami was verified by preparing a mica sample from the folded, unpurified origami solution. This kind of mica sample is presented in figure 19. As DNA binds to mica more strongly compared to silicon, even the excess staples and unfolded scaffold can be seen on the background. Typically, it is rare to

encounter excess ssDNA on silicon.

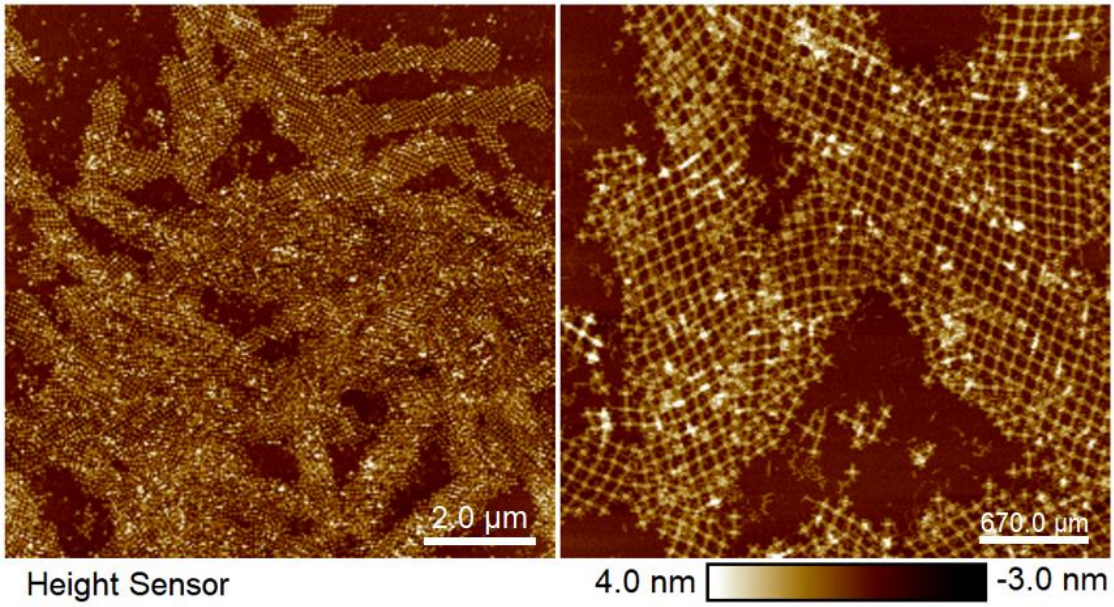

Figure 19. A mica sample with folded, unpurified TC-ST origami. The origami tile concentration is approximately 20 nM for an incubation time of 5 min.

4.2 The effect of different ions and incubation time on lattice assembly: AFM imaging in air

This section experiments with different ionic conditions and incubation times for achieving an efficient lattice assembly protocol for dried samples on the silicon surface. The aim is to produce a single layer of ordered origami lattice with minimal amount of lattice errors throughout the whole silicon surface. Divalent cations, in this case magnesium ions Mg^{2+}, are used to first attach origami on the silicon surface. After the sufficient level of attachment is achieved, the effect of monovalent (Na^+, K^+, Li^+) and other divalent (Ni^{2+}, Ca^{2+}) cations on lattice formation is studied to optimize the conditions for efficient lattice growth. The effects of different ions are presented individually in sections 4.2.1-4.2.5. Also, the effect of incubation time on lattice assembly is presented in section 4.2.6.

Multiple areas were imaged for all samples using QNM air AFM imaging. Larger scan sizes from 10 µm up to 40 µm were used to find structures on the surface. Smaller scan sizes down to 1 µm were used to image details of more interesting structures. Based on the following section, it is clear that for an individual sample separate areas can appear quite different. A single sample might have areas where the origami are concentrated into piles or neat lattices, whereas another area might only have single origami, small lattices or can be completely empty. Since finding spots with more concentrated areas of origami from the chip is based on luck (although multiple areas were imaged) the consistency of analyzing the dynamics of the system gets more difficult. Therefore, it is more important to study the trend for each sample rather than blindly draw conclusions from an individual image.

4.2.1 The effect of Mg^{2+} ions on lattice formation

The first experiments were conducted using magnesium ions to get origami to attach on the negatively charged silicon surfaces. For dried samples and with the current sample protocol, a magnesium concentration of 12.5 mM is not enough to attach cross-tile origami on a silicon surface (sc-Si or α-Si), although it is enough for mica. Most of the air AFM 10-20 µm scans are completely empty and it takes time and effort to find any origami in this low concentration of magnesium. Around 100 mM magnesium concentration, a reasonable amount of origami have attached on the surface. Magnesium concentrations below 100 mM are not sufficient to attach the

origami tightly enough to the surface. This finding, that elevated salt concentrations are needed to attach origami on silicon compared to mica, was also reported earlier by the DALI group [8]. Although, as discussed in section 4.3, liquid AFM imaging reveals that lower amounts of magnesium can be used to image origami in liquid media but this is not true for dried samples and imaging in air. Therefore, most of the origami are too loosely bound on the surface for this low concentration of magnesium and are washed away by the sample washing procedure. This obstacle is revisited in section 4.4, where the information provided by the current experimental section allows the current sample washing technique to be improved.

Larger scan sizes were used to study the amount of attached origami for each magnesium concentration. The amount of attached origami on the surface increases gradually with the increasing concentration of magnesium for both sc-Si and α-Si surfaces as shown in figures 20 and 21. The trend for increasing the magnesium concentration generates more lattices but in the end starts clumping origami into big piles. This is expected since magnesium neutralizes the charges in the DNA backbone and therefore lowers the repulsion between individual origami and glues them together, building aggregations. When the concentration of magnesium becomes too high it most likely starts to build up on top of the origami as the lattices seem to be covered with something high (compared to origami height of 2.5 nm-3 nm). This build-up also starts interfering with AFM imaging as the images are condensed with many artifacts. Even with our enhanced 10× washing procedure (see section 3.1) this starts happening around 500-700 mM magnesium concentration. Therefore, increasing and using only magnesium ions is not sufficient to form large-scale lattices on silicon. Concentrations above 700 mM should not be used unless the washing procedure or other aspects of getting rid of the salt aggregations are improved. To be on the safer side, total salt concentrations above 500 mM should be avoided.

Since magnesium concentrations above 300 mM strongly aggregate origami together, close-up images were only taken for lower magnesium concentrations to study the differences between the two surfaces. The lattice structures grow in size when the magnesium concentration increases. As shown in appendix F in figure 44, at 100 mM magnesium concentration the origami are already starting to attach to each other to form small lattices. Connected origami of around 2-6 units (one unit being a single origami) can be found at this concentration. The further increase in magnesium concentration supports the lattice formation of cross-tiles. Bigger

lattices start forming around 200-300 mM concentration of magnesium. At 300 mM magnesium concentration 2-4 µm lattices form.

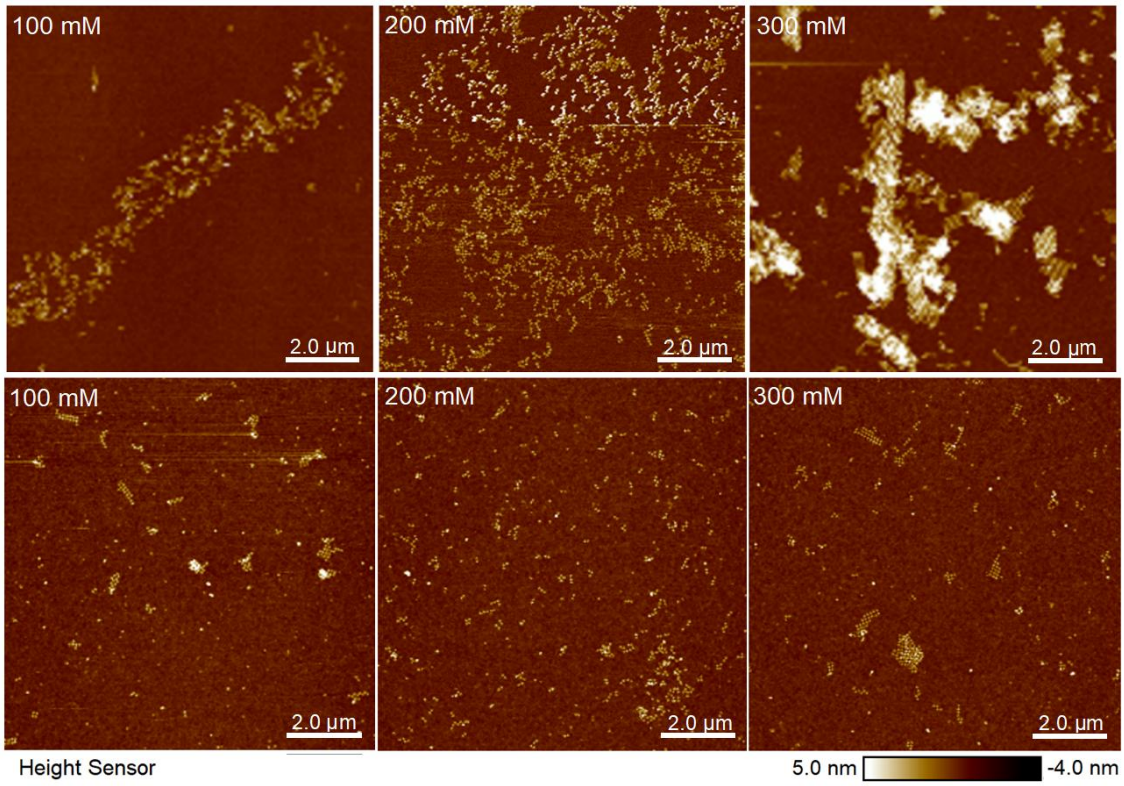

Figure 20. The effect of increasing the magnesium concentration for sc-Si (upper row) and α-Si (lower row) surfaces. Each AFM image represents a different sample with incubation time of 40 min and magnesium concentration specified on the top left corner. The TC-ST origami concentration for each sample is 10 nM. The samples on the top-left and -right were cropped from a larger image resulting in lower resolution compared to the other samples. Also, some imaging problems were encountered with the sample on the middle of the top row.

Compared to the sc-Si surface the α-Si surface has a relatively similar amount of origami attached with the magnesium concentration of 100 mM. Only the distribution of origami on the surface is a bit different. In comparing these two surfaces, the higher surface roughness of the α-Si surface changes the lattice formation properties to an extent. There are more isolated, slightly larger and more defined lattice structures on the α-Si surface. There also seems to be more single origami in between the small lattice structures (around 5-15 units). Most likely, a rougher surface is more inclined to grow lattices from separated nucleation spots, whereas on sc-Si adjacent, small lattices are pulled together and rearranged into bigger lattices. This implies that a

rougher surface requires more origami mobility to overcome the energy barrier and attach the separately growing units. Although, it is not clear why the origami on the sc-Si surface are not always connected to neighboring origami, if the lower surface roughness creates more energetically favorable environment for lattice formation.

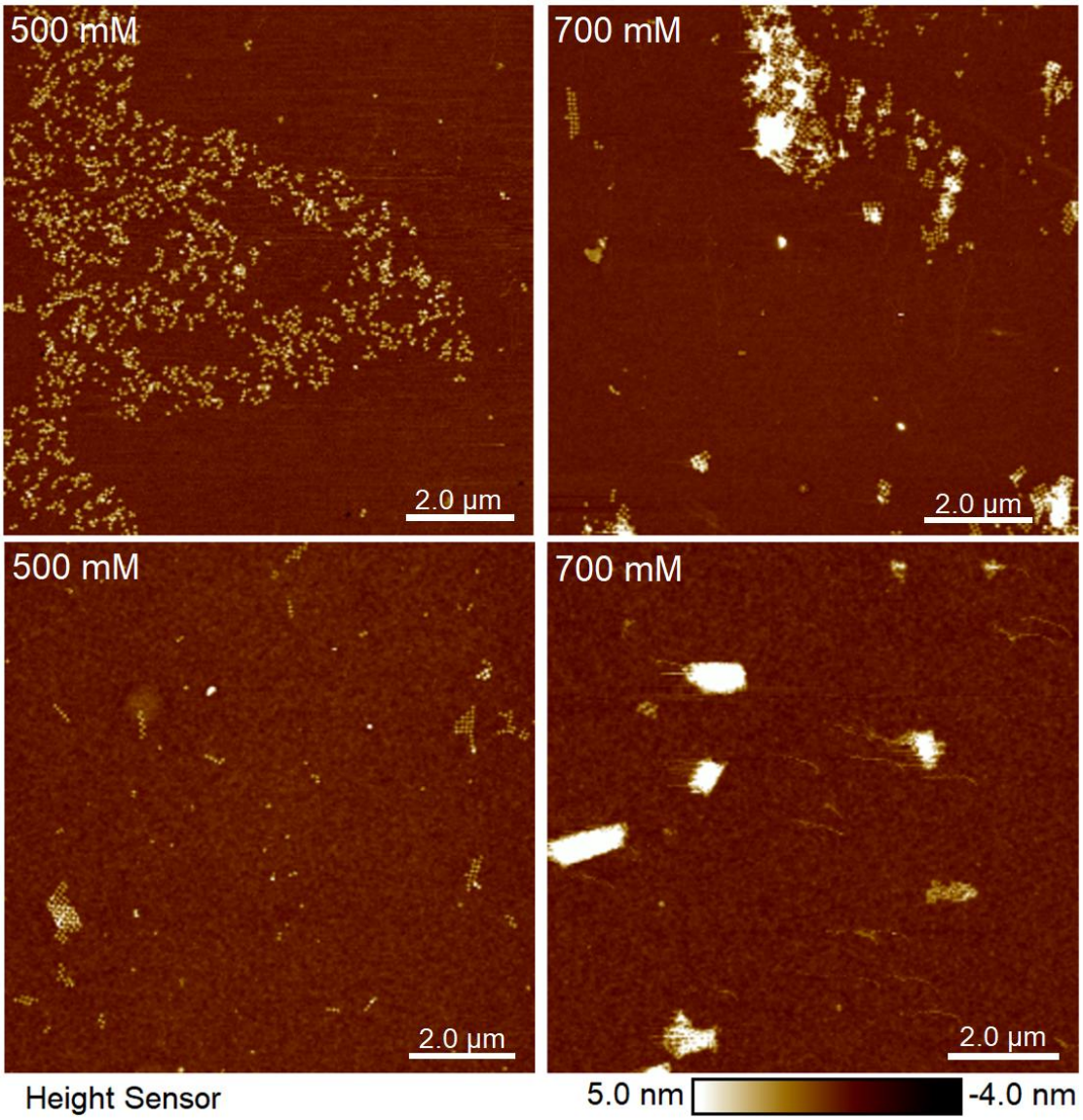

Figure 21. The effect of increasing the magnesium concentration for sc-Si (upper row) and α-Si (lower row) surfaces. Each AFM image represents a different sample with incubation time of 40 min and magnesium concentration specified on the top left corner. The TC-ST origami concentration for each sample is 10 nM for the 500 mM samples and 6 nM for the 700 mM samples.

Based on these experiments, it is clear that to form bigger uniform lattices some

other ion (or another energy source) should be incorporated on the interface to increase surface mobility, since the origami that are closer together are not always attached. Since monovalent ions are used to tweak surface interactions by screening some of the surface charges to loosen the origami, the effect of sodium ions on lattice assembly is studied next. Also, since the difference between sc-Si and α-Si surfaces regarding origami attachment on the surface and lattice assembly kinetics seems minor, the differentiation of silicon surface type is mostly omitted in the future sections.

4.2.2 The effect of Na^+ ions on lattice formation

Since the magnesium concentration of 200 mM is sufficient for binding a reasonably good amount of origami on the surface for both silicon types, it was chosen for further experiments. When adding increasing amounts of sodium ions, the amount and size of origami lattices decreases gradually. More single origami are observed rather than connected structures even when they are in close proximity to each other. Surprisingly, the connections between origami seem to be disassembling for increasing the amount of sodium ions. The complete opposite result was expected since high sodium concentrations, *e.g.*, 400 mM are used with mica surfaces to improve lattice quality and monolayer formation [6].

Figures 22 and 23 showcase the decrease in lattice growth for increasing sodium concentration. The samples with highest sodium concentrations have defined areas of disconnected origami "islands" with clean surface around them. The origami are usually not attached inside the islands although they are very close to each other. The formation of these islands was found to be the trend for high monovalent cation concentrations combined with sufficiently long incubation times (here 40 min).

As discussed in section 2.4, monovalent cations are known to screen charges and can therefore lower the repulsion between origami, but unlike with divalent cations attraction between origami is not increased. In the experiments, almost any amount of sodium is able to inhibit the formation of lattices as the attractive interactions between origami have also decreased. For higher sodium concentrations more of the surface charges are screened to a point where more origami are detached in the washing step of sample preparation. The origami might need to be bound using a more efficient divalent cation to retain the attractive forces between origami before the repulsive element can be adjusted. Very high sodium amounts can also completely

saturate the surface making the origami unable to move through the salt

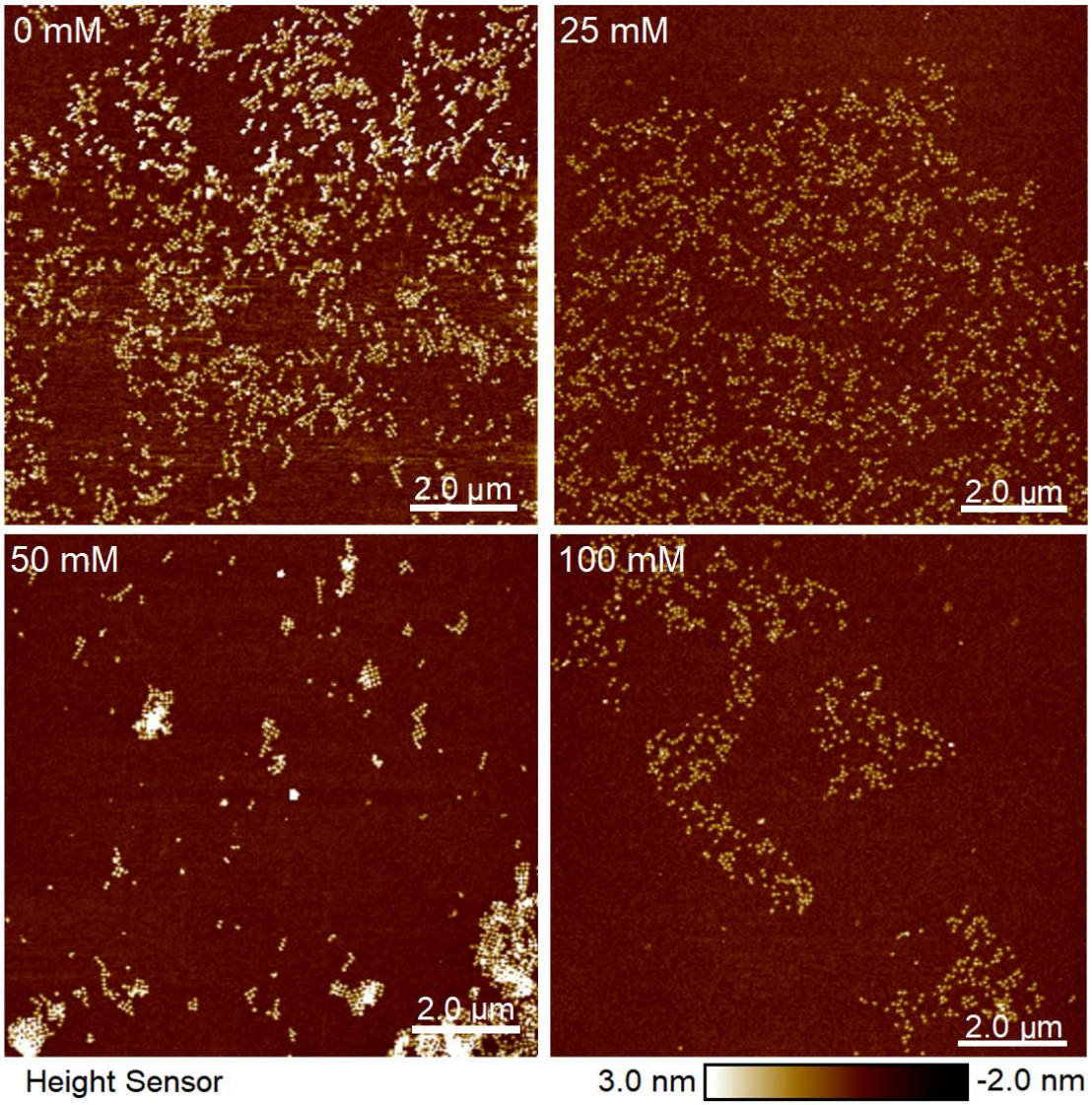

Figure 22. The effect of increasing the sodium concentration for sc-Si surface. Each AFM image represents a different sample with incubation time of 40 min and has a fixed magnesium concentration of 200 mM. The TC-ST origami concentration for each sample is 10 nM.

aggregations, but this could not explain the origami behaviour in low sodium concentrations. Increasing the concentration of sodium to very high amounts (*e.g.*, 1.6 M and above) again starts generating more salt buildups but not as excessively as increasing the magnesium concentration. With high sodium samples, lattices do not form anymore and therefore, do not act as platforms for the salt to build up on. Although, the aggregation of salt is not as extensive as with magnesium, some level

of imaging problems are encountered for sodium concentrations above 600 mM.

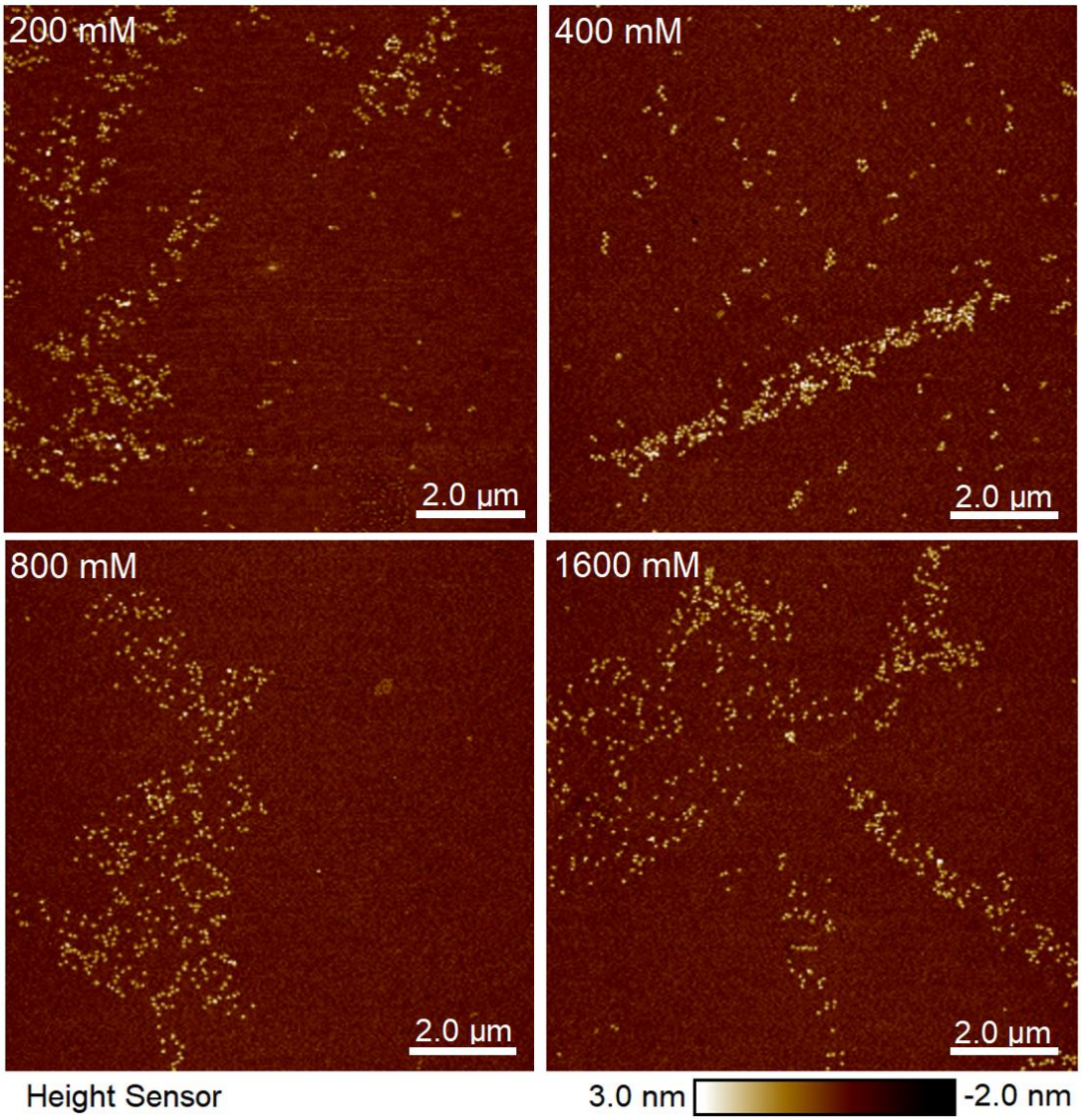

Figure 23. The effect of increasing the sodium concentration for sc-Si surface. Each AFM image represents a different sample with incubation time of 40 min and has a fixed magnesium concentration of 200 mM. The TC-ST origami concentration for the samples on the top row is 10 nM. On the bottom row, the 800 mM sample has an origami concentration of 9.1 nM and the 1600 mM sample has an origami concentration of 7.7 nM.

Two-step incubation was also tested for the pairing of magnesium and sodium. The results are presented in appendix F figure 45, but no substantial improvement in lattice formation was achieved using a two-step protocol where sodium and magnesium were incubated separately on the sample. In conclusion, compared to

mica surfaces, the salt concentrations need to be considerably higher to even attach the origami on the silicon surface. Although different salt concentration combinations were extensively studied between magnesium and sodium ions, considerably larger and uniform lattice-structures were not obtained. This suggests that other ions should be yet researched to obtain a better result. Especially, two other divalent cations (Ni^{2+} and Ca^{2+}) will be studied in effort to obtain stronger attractive forces between origami.

4.2.3 The effect of Ni^{2+} ions on lattice formation

The experiments with nickel ions were started with very low concentrations, under 5 mM, as its effect on origami is believed to be very strong. As shown in appendix F figure 46, when only nickel is added, already a 1.5 mM concentration is able to aggregate all of the origami together into large 40 nm high clumps having no separate origami on the surface. Since nickel can not be used by itself to create monolayers of lattices, it was used for samples which already had varying amounts of magnesium and sodium ions. To study the effect of nickel on lattice formation the concentrations of magnesium and sodium were initially kept low. From figure 24 we can deduct that for a fixed concentration of 50 mM of magnesium and sodium, increasing the nickel concentration improves lattice formation but also, nickel gets heavily aggregated on top the origami and even enhances the formation of multilayered structures. Only increasing the concentration of nickel is therefore not able to saturate the whole chip surface with a single layer of lattice but rather enhances lattice growth in one direction creating "ribbon" shaped structures. Additionally, too high concentrations of nickel tend to inhibit lattice growth by having the structures bound too strongly on the surface and each other. It is also a special property of nickel that it strongly aggregates on the unbound freely hanging tail-structures of each origami when the concentration is increased too high, as discussed previously in section 4.1.

Since nickel clearly is a stronger binding divalent cation compared to magnesium, most likely for having preferred binding sites in the phosphates as well as the bases (see section 2.1), and exhibits stronger attraction between origami, increasing the amount of monovalent cations with sodium was tried again. From figure 25 we can see that for a fixed magnesium concentration of 50 mM and nickel concentration of 5 mM, there exists a valley of preferred sodium ion concentration of around 250 mM, where elongated, multilayered origami assemblies are formed. For lower or higher

sodium concentration the lattices are smaller, more spread out or less consistent. It is clear, that adding nickel does improve lattice formation as long as the other ion conditions are also favorable.

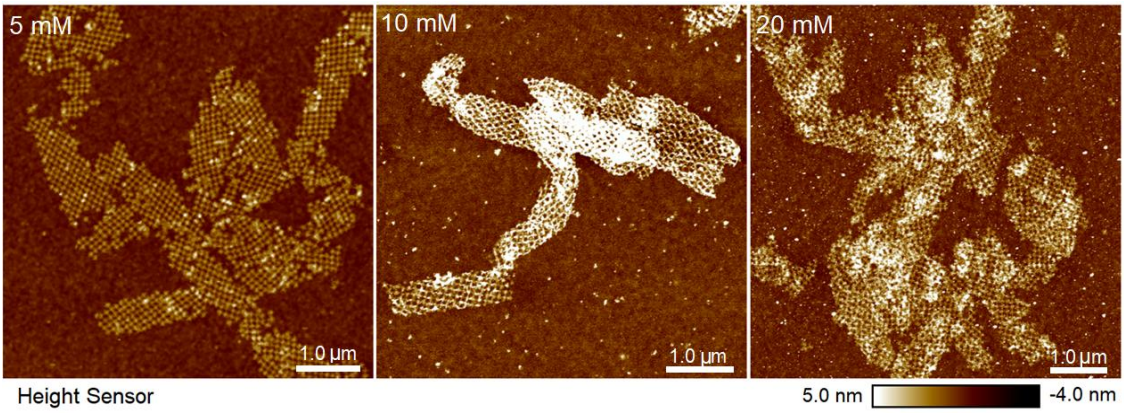

Figure 24. The effect of increasing the concentration of nickel for fixed magnesium and sodium concentrations of 50 mM for silicon surface. Each AFM image represents an individual sample with incubation time of 30 min and nickel concentration specified at the top left corner. The TC-ST origami concentration for each sample is 10 nM.

Interestingly, the nickel experiments induced a very clear preferred direction or shape of lattice growth for our ST structure. Nickel endorses the formation of ribbon-like structures that mainly grow in length rather than width. Since the ribbon-like structures are also visible on the mica sample of figure 19 (section 4.1) the ribbon type growth is probably not only a feature of nickel ions but has something to do with our ST design. Most likely, nickel is able to improve the lattice growth into high enough level for the ribbon-like growth to become evident. Clearly, since the ST origami expresses this type of unidirectional growth also on the mica surface without the presence of nickel, something about mica also enables lattice assembly in liquid. It is mentioned by Liu *et al.* that a corrugation strategy, alternating two type of ST origami to cancel each others bending, should be used to avoid tube formation [9]. The ribbon structures have a rather consistent width of about 0.5 µm and a varying length of a few micrometers. The longest ribbons are usually partially connected to other neighbouring ribbons, as was seen in the sample set of figure 25. The precise width was determined to be 522±72 nm by averaging the widths of multiple ribbons, where the error is in the order of a single origami.

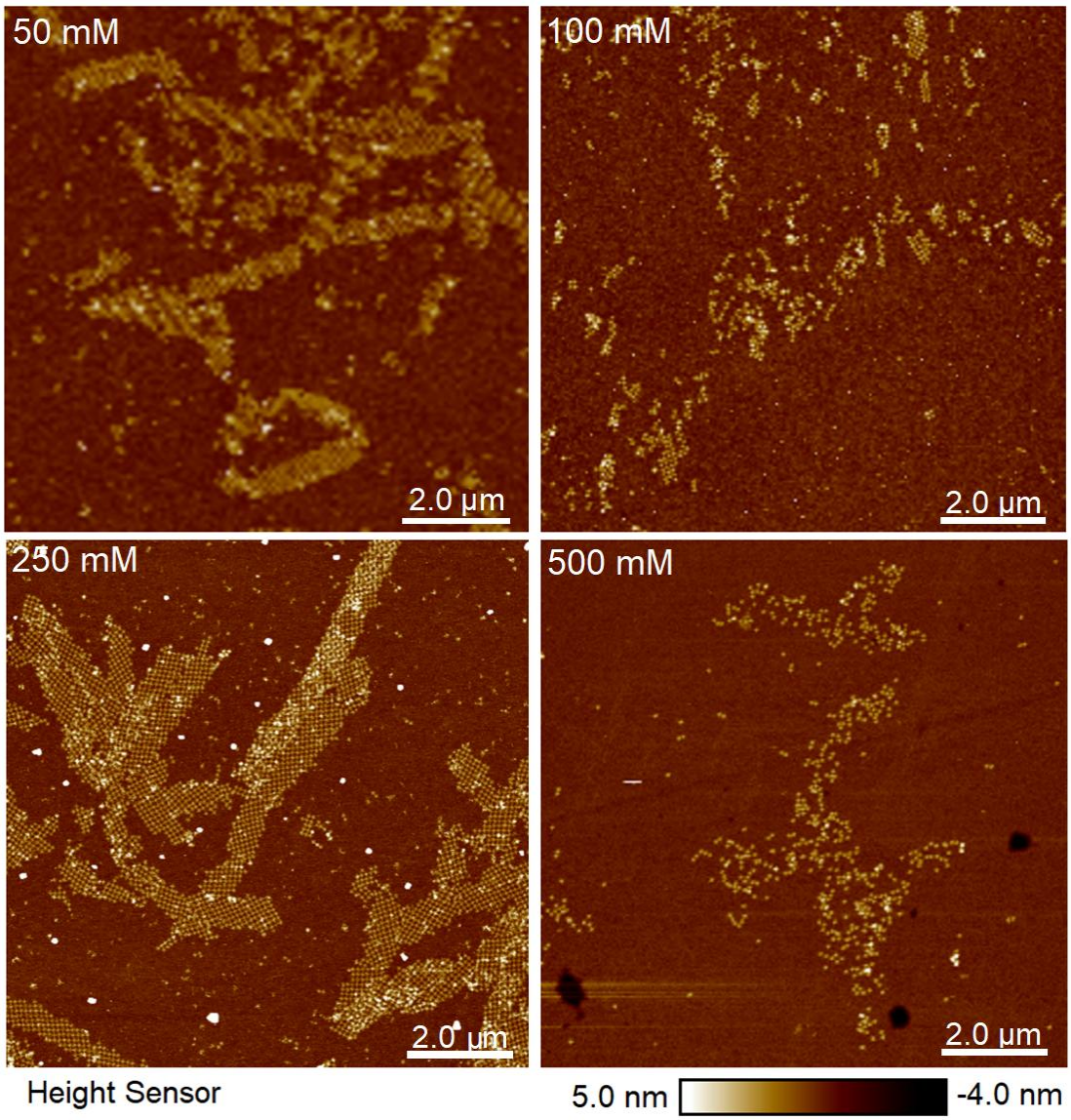

Figure 25. The effect of increasing the concentration of sodium for a fixed magnesium concentration of 50 mM and nickel concentration of 5 mM for silicon surface. The sample at the top-left was imaged with lower resolution than the rest of the samples. Each AFM image represents a different sample with incubation time of 30 min (45 min for the bottom-right sample). The sodium concentration is specified at the top left corner of each image. The TC-ST origami concentration for each sample is 10 nM.

The approximately 45° tilt of origami inside the ribbons is rather interesting. Figure 26 presents almost a perfectly sharp edged, double-layered structure where the bottom and top layers are turned in an angle of exactly 45°. Because of the consistent width of these structures, it is possible that lattices and the ribbon structures are

forming already in the sample liquid by growing into a tubular shape. The assembly in liquid might allow the lattice to start turning onto itself forming a tube or a wire structure, which collapses on the surface during incubation. If this is the case, the formation of these tubules should be studied further to restrict the lattice growth only to the wanted surface.

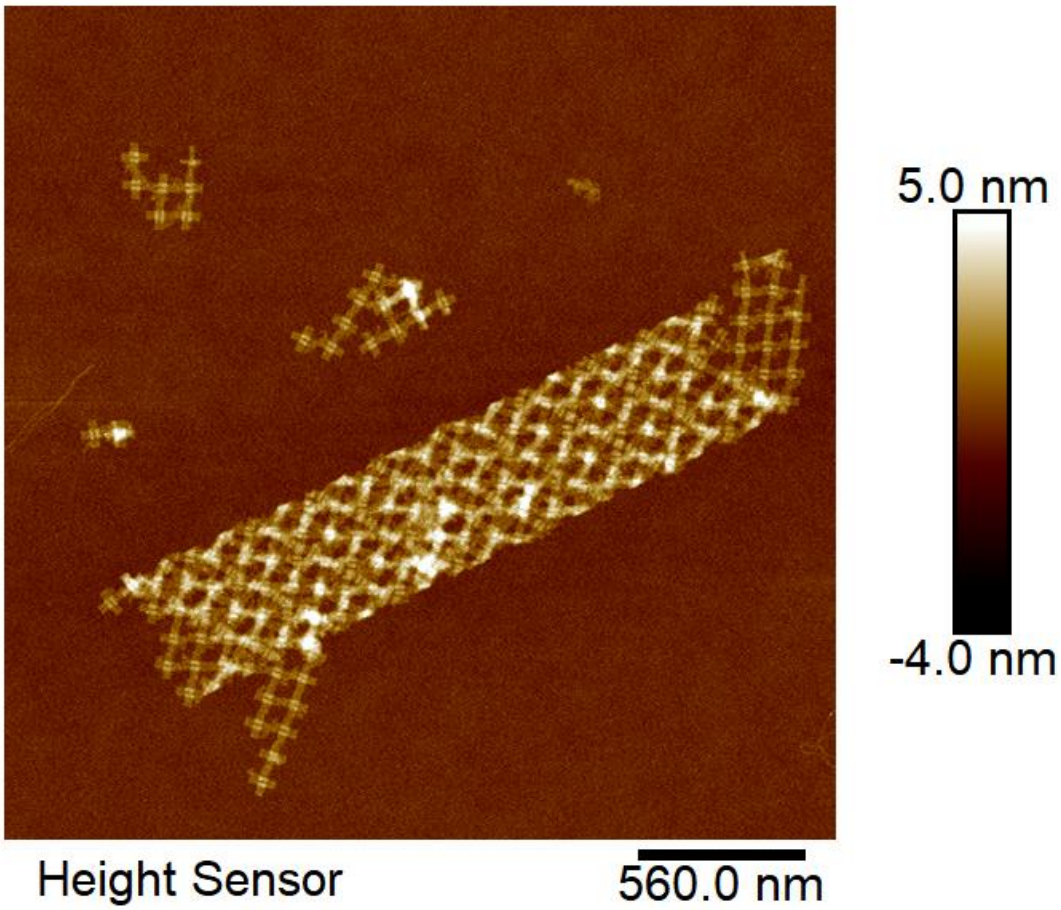

Figure 26. A double-layered, sharp-edged, tubular lattice structure with 45° tilt, *i.e.*, shift in orientation between layers. Sample conditions included TC-ST origami concentration of 10 nM, magnesium concentration of 50 mM, nickel concentration of 5 mM, sodium concentration of 250 mM and incubation time of 30 min on sc-Si surface.

Double-layered ribbons are observed in certain ionic conditions. The relative concentrations between the divalent cations were alternated as shown in figure 27. As the concentration of nickel is increased compared to magnesium, also the double layering of the ribbon structures keeps growing. Therefore, the ribbon- to tube-like morphology can be adjusted by changing the relative concentrations of the divalent

ions. This effect can arise from the base binding ability of nickel as it enforces origami-origami interactions.

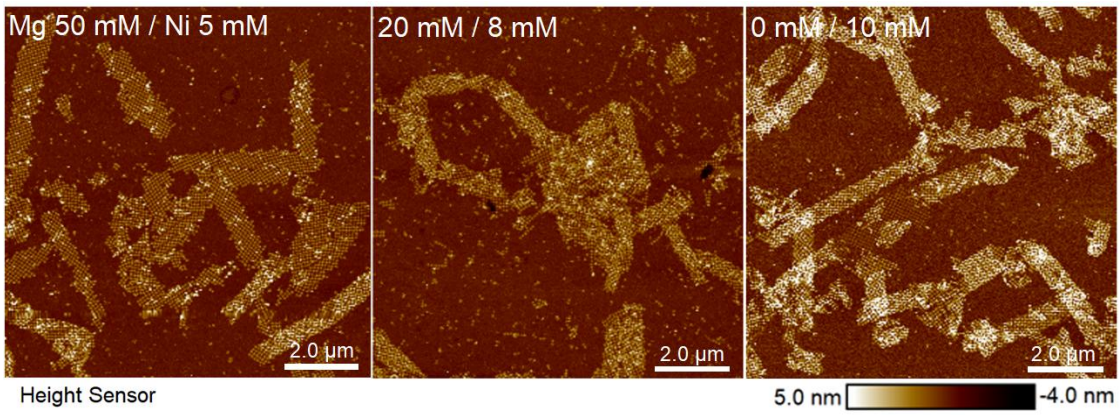

Figure 27. The relative concentration of divalent ions can adjust the level of double layering creating either ribbons or more tube-like structures in liquid. The sodium concentration was fixed to 250 mM, while varying the magnesium and nickel concentrations as indicated at the top-left corner of each figure, respectively. Each AFM image represents an individual sample with 30-45 min incubation time and TC-ST origami concentration of 10 nM.

To study further the tube-like structures and their possible lattice assembly already in liquid, cryogenic electron microscopy (cryo-EM) was performed in collaboration with Ashwin Natarajan and Assoc. Prof. Anton Kuzyk at Aalto University. The results for the 50 mM magnesium, 5 mM nickel and 250 mM sodium sample using cryo-EM imaging are presented in figure 28. Since there is no surface to aid in lattice formation, it was confirmed that the ribbon and tube-like structures (double-layered ribbons with sharp edges) already assemble in liquid.

The thickness of ice in cryo-EM is only 70-120 nm. Since the width of a collapsed tube structure in dry conditions, like the one presented in figure 26, is approximately 500 nm, the diameter of a fully rounded structure in liquid conditions should be below this value. If we assume that the tube gets fully flattened in dry conditions, the perimeter of the tube should be twice the width of the collapsed structure. For a circle with a perimeter of 1000 nm, we get the diameter to be

$$\frac{1000\,\text{nm}}{\pi} = 318.30988... \approx 320\,\text{nm}, \tag{4}$$

which is almost three times larger than the widest part of the frozen sample. Therefore, even if the structures appear as tubes in liquid they would be compressed by the

ice during freezing. Because of the compressed morphology, the tubular shape could not be undoubtedly verified with these experiments. Nevertheless, especially the tilt series, out of which the clearest capture is shown in figure 28, revealed two origami layers separated by an empty space. These results greatly support the hypothesis of tubules forming in liquid environment in higher ion concentrations. Dry state imaging was also tried, but due to excessive beam damage and destruction of origami by unfolding, this type of experiments could not be done with or without negative staining.

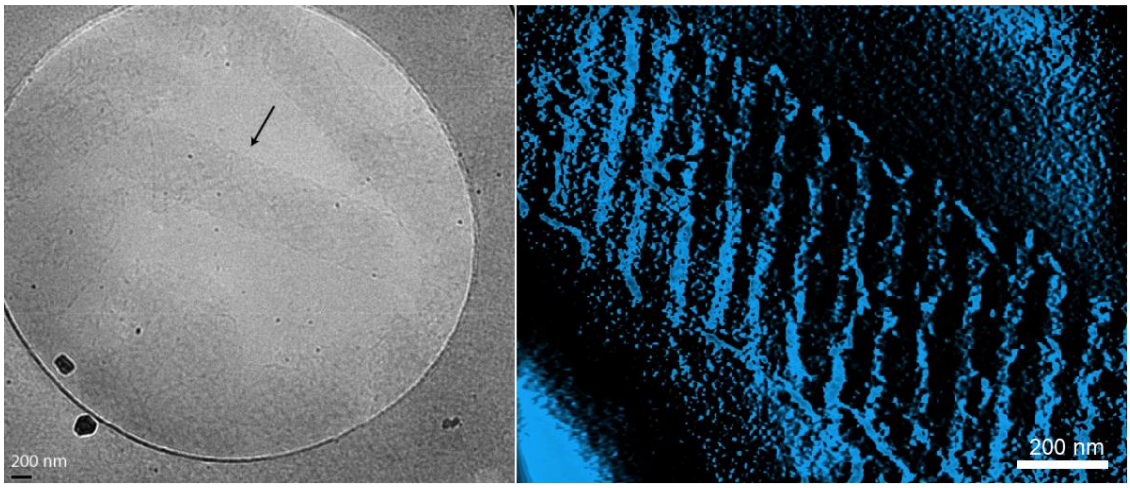

Figure 28. Cryo-EM imaging for tube-like origami structures. Sample conditions included TC-ST origami concentration of 10 nM, magnesium concentration of 50 mM, nickel concentration of 5 mM and sodium concentration of 250 mM. On the left, a tubular shape indicated with an arrow on a quantifoil grid in cryo conditions. On the right, a capture of a tilt series performed for the same sample.

Two-step incubation experiments were also performed with the three salt combinations of magnesium, sodium and nickel. Ionic conditions of 150 mM of magnesium and 100 mM of sodium were chosen for the two-step experiments as these conditions have a decent amount of origami attached. The two-step experiments were started with low amounts of nickel in 3 mM concentration. A noticeable improvement in lattice growth is achieved only when nickel is introduced last during incubation. This type of sample procedure is referred to as nickel wash also in the upcoming sections. The notation Ni^{2+} wash (X+Y min) means that all the other ions except nickel were introduced for the first specified incubation time of X minutes after which nickel was added for the second incubation time of Y minutes. After the ion washing steps, the normal washing procedure with Milli-Q H_2O and drying with N_2 was performed.

Figure 29 presents a variation in incubation times for two-step nickel wash samples. Out of the samples, best results are obtained with the shortest incubation time and equal duration for both origami deposition and washing. There is not a big difference between the rest of the samples. Nickel washing aids in lattice formation already in

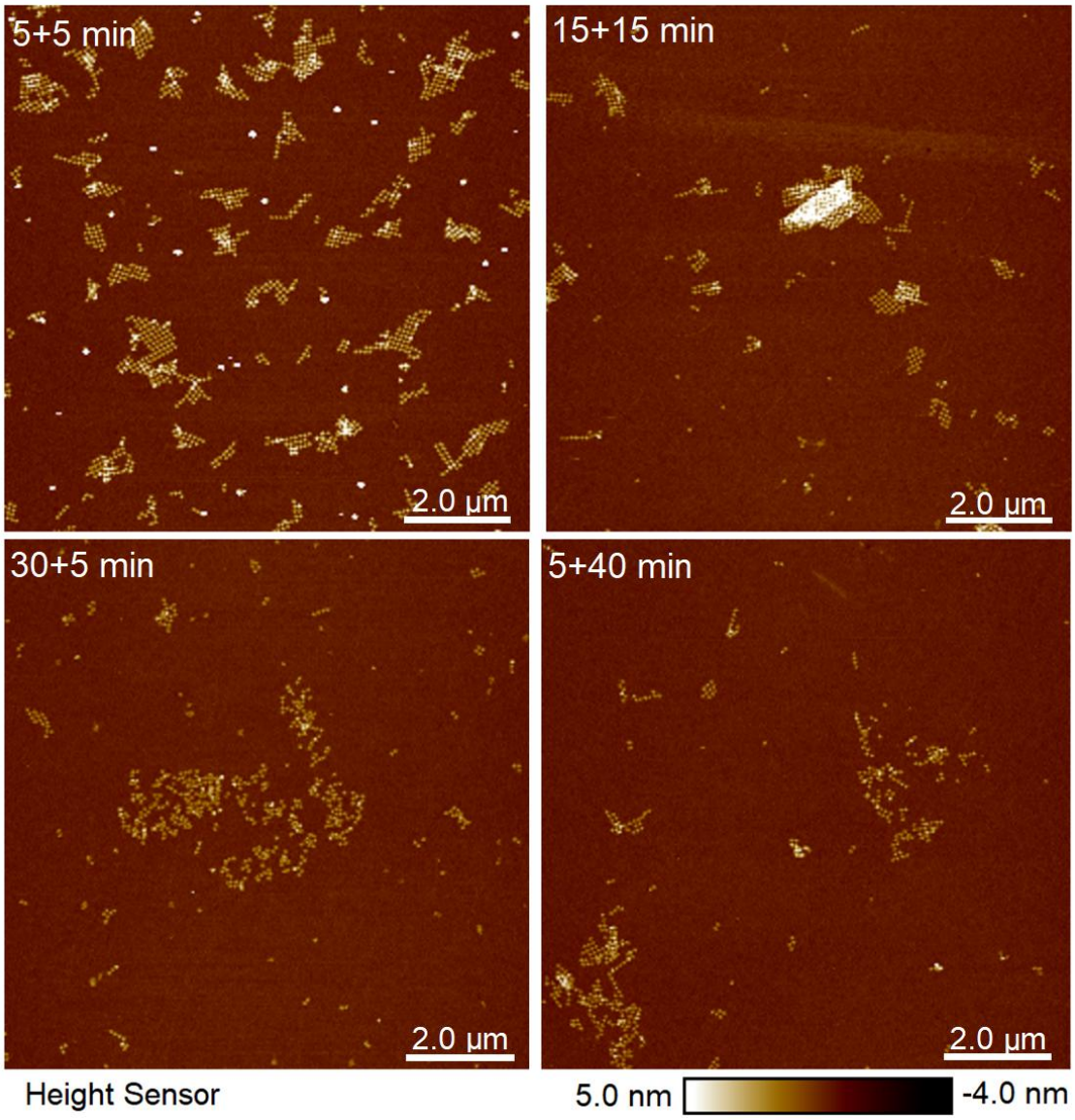

Figure 29. Two-step nickel wash time variations on sc-Si surface. Each AFM image represents an individual sample with 150 mM magnesium, 100 mM sodium and 3 mM nickel wash concentrations. The two-step incubation times for each sample are specified at the top-left corner of each image in X+Y min form. Magnesium and sodium were incubated on the sample for X min after which nickel was introduced on the sample for Y min. The TC-ST origami concentration for each sample is 10 nM.

small amounts but can easily inhibit the growth of bigger lattices by aggregating the origami together if too high concentrations are used. Increasing the nickel concentration to 5 mM helps to grow the size of the structures but also the amount of aggregations starts to increase as shown in appendix F figure 47. Although, an improvement in lattice assembly can be seen for two-step nickel washed samples, the one-step incubation is still giving preferable results with simpler protocol.

Although, lattice assembly under the influence of nickel helps in creating far larger connected structures in the shape of ribbons, the unidirectional growth in liquid creates a challenge for monolayer formation. Ideally, connected structures should only form in the presence of a surface to avoid the stacking of large structures landing on the surface as they might inhibit lattice corrections. The effect of potassium ions is studied next to see whether a base binding monovalent cation can compete with the binding sites with nickel. Also, the lattice assembly kinetics in liquid are studied in sections 4.3.2 and 4.4.1.

4.2.4 The effect of K^+ ions on lattice formation

The lattice assembly needs to still be optimized as the growth favors elongated tubular structures over 2D lattices. Potassium has similar hydration abilities compared to sodium ions, which makes it a good candidate for replacing the monovalent cation. Another advantage of using potassium is the affinity of the cation to bind to the nucleobases in DNA instead of the backbone phosphates, as nickel binds to both of these sites (see section 2.1.1). Comparing one of our best samples regarding surface coverage and origami adsorption with defined ribbons in figure 25 (with 50 mM Mg^{2+}, 5 mM Ni^{2+} and 250 mM Na^+), the ribbons assembled using potassium shown in figure 30 have more holes in them. Since potassium is a larger ion compared to sodium its charge density is lower. Therefore, potassium should bind the origami more weakly to the surface compared to sodium. A more weakly binding ion should increase the mobility of origami, which in this case can lead to more incomplete lattices. A larger ionic radius can also lead to steric hindrance interactions growing the distance between the origami and the surface. If potassium does not bind the structures strongly enough to the surface, they can detach more easily during the sample washing procedure, leaving behind more incomplete structures. At least in concentrations under 250 mM, potassium does not pile-up origami significantly as suspected by having the preferred binding site at the bases in DNA (see section 2.1).

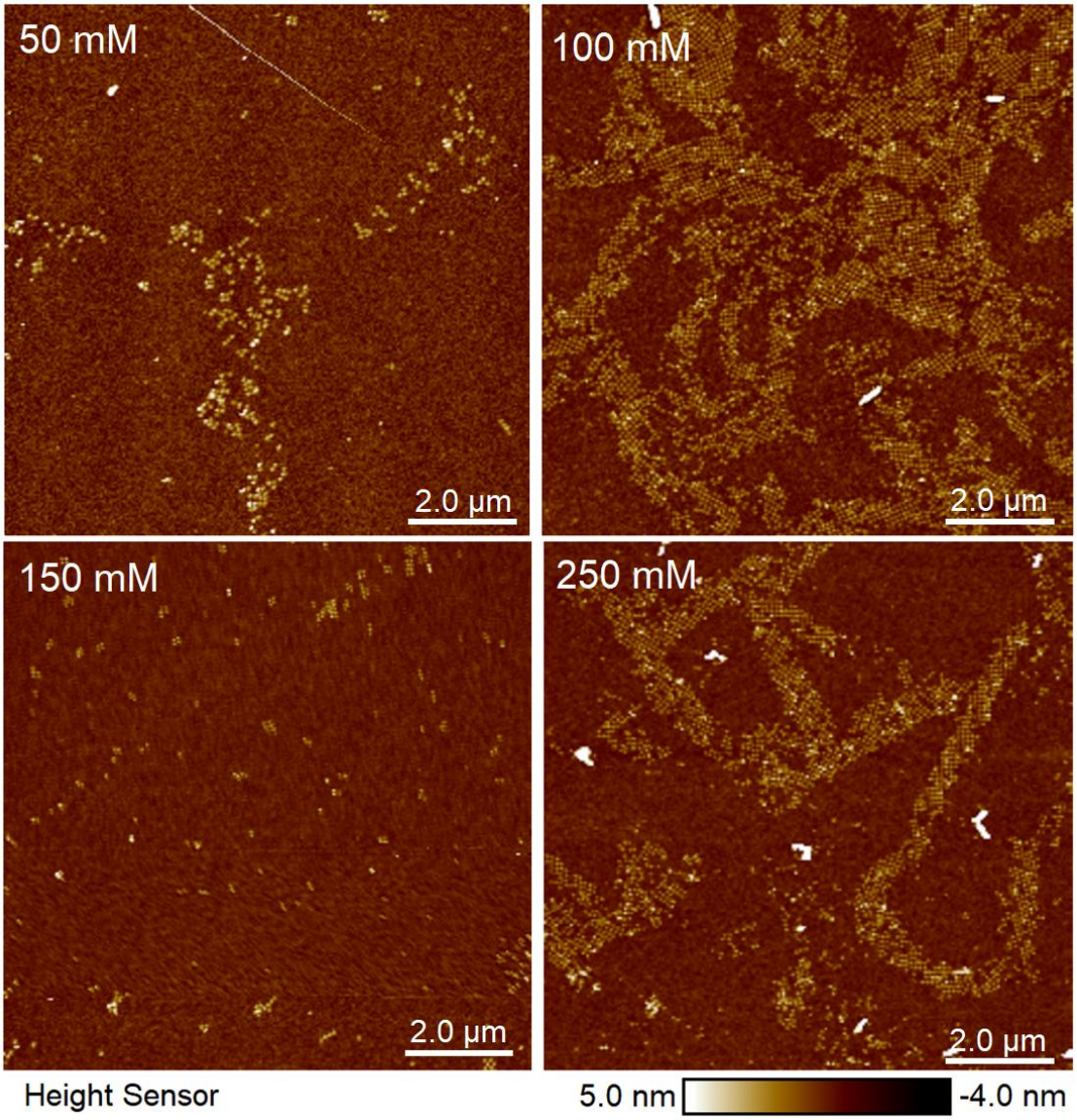

Figure 30. The effect of increasing potassium for a fixed 50 mM magnesium and 5 mM nickel concentrations on a silicon surface. Each frame represents an individual sample with potassium concentration indicated at the top-left corner. Incubation time for the 100 mM sample was 90 min and for the 250 mM sample 30 min. The two other samples were incubated for 45 min. The TC-ST origami concentration for each sample is 10 nM.

When the concentration of nickel is increased to 10 mM, omitting any added magnesium, we get a far better surface coverage for 100 mM of potassium as shown in figure 31. Although, few spots of stacked origami are forming, the multilayer formation is still less extensive than what was encountered with the nickel experiments already in 10 mM concentrations (see figures 24 and 27). Most likely, the large ionic

radius of potassium is able to disrupt some of the origami-origami interactions through steric hindrance in the nucleobase binding sites where nickel is displaced with potassium. Therefore, potassium ions can be utilized to lower the multilayering effects of nickel. Different monovalent cations could even be mixed to acquire the desired ionic environment. Furthermore, the effects of Ca^{2+} and Li^{+} are studied to discover more ways to guide the lattice assembly and to obtain different ionic properties as they do on mica [6].

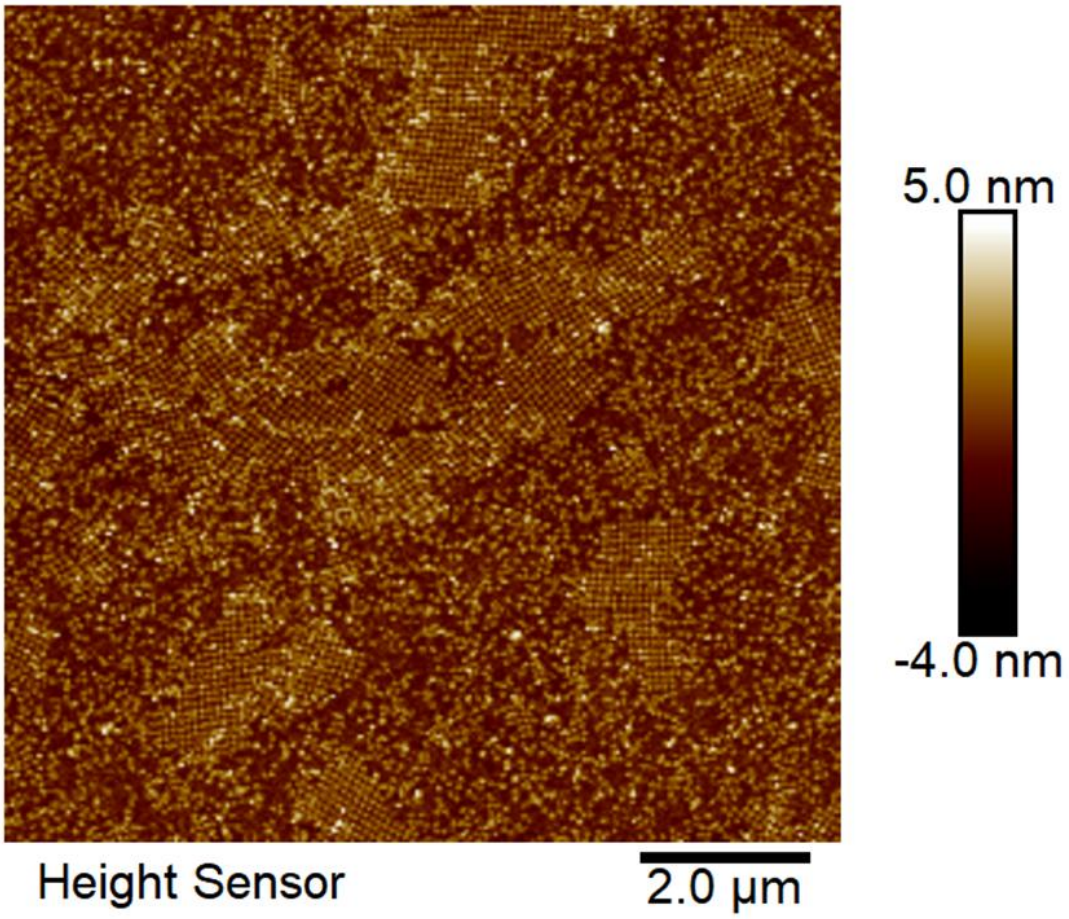

Figure 31. A sample with nickel concentration of 10 mM, potassium concentration of 100 mM and 45 min incubation time on α-Si. The TC-ST origami concentration is 10 nM.

4.2.5 The effect of Ca^{2+} and Li^{+} ions on lattice formation

Compared to magnesium, calcium is reported to be superior in forming higher-quality DNA origami lattices for the close-packing triangle origami on mica as it can be displaced from the DNA backbone more easily by sodium [5]. In our case, it became quickly apparent that longer incubation or storing times as well as higher calcium concentrations start to destroy the ST origami. Storing DNA origami in only calcium buffer starts degrading the origami already in a few weeks. Even when the origami were otherwise stored with the regular magnesium buffer, longer incubation times (around 2 h or more) also seemed to deform the origami.

Barely any origami were seen on the calcium containing samples with short incubation times (<60 min). Figure 32 shows four individual calcium experiments. As can be seen from the two first samples on the upper row, the total amount of attached origami is low and only few connections are made. Also, some of the origami get deformed, mushed, or thinner than usual. On the top-left sample, a low amount of magnesium (30 mM) was used in combination with calcium to ensure the attachment of at least some origami as using only calcium did not supply strong enough surface attachment. On the top-right, some nickel was added to help with surface attachment, but no real improvement can be seen. When the ionic conditions are slightly adjusted and the incubation time is increased to 240 min, shown on the bottom-left, large piles of ribbons with aggregations on top of them are suddenly observed. The silicon surface is also completely covered with small droplets as well as some unfolded scaffold not normally seen on silicon. The amount of attached origami increases dramatically, although they are all concentrated on a single spot and more unfolded origami are observed. Similar results are obtained for ionic conditions presented on the bottom-right for only 60 min incubation time. Although, the top-left sample has more than twice the calcium concentration of the bottom-right sample, no similar pile-ups can be seen. The Mg^{2+}:Ca^{2+} ratio keeps increasing from left to right and top to bottom in figure 32, having values 0.43, 1.00, 1.67, 2.40. The lower the ratio or the more we have calcium, the less the origami seem to attach on the surface.

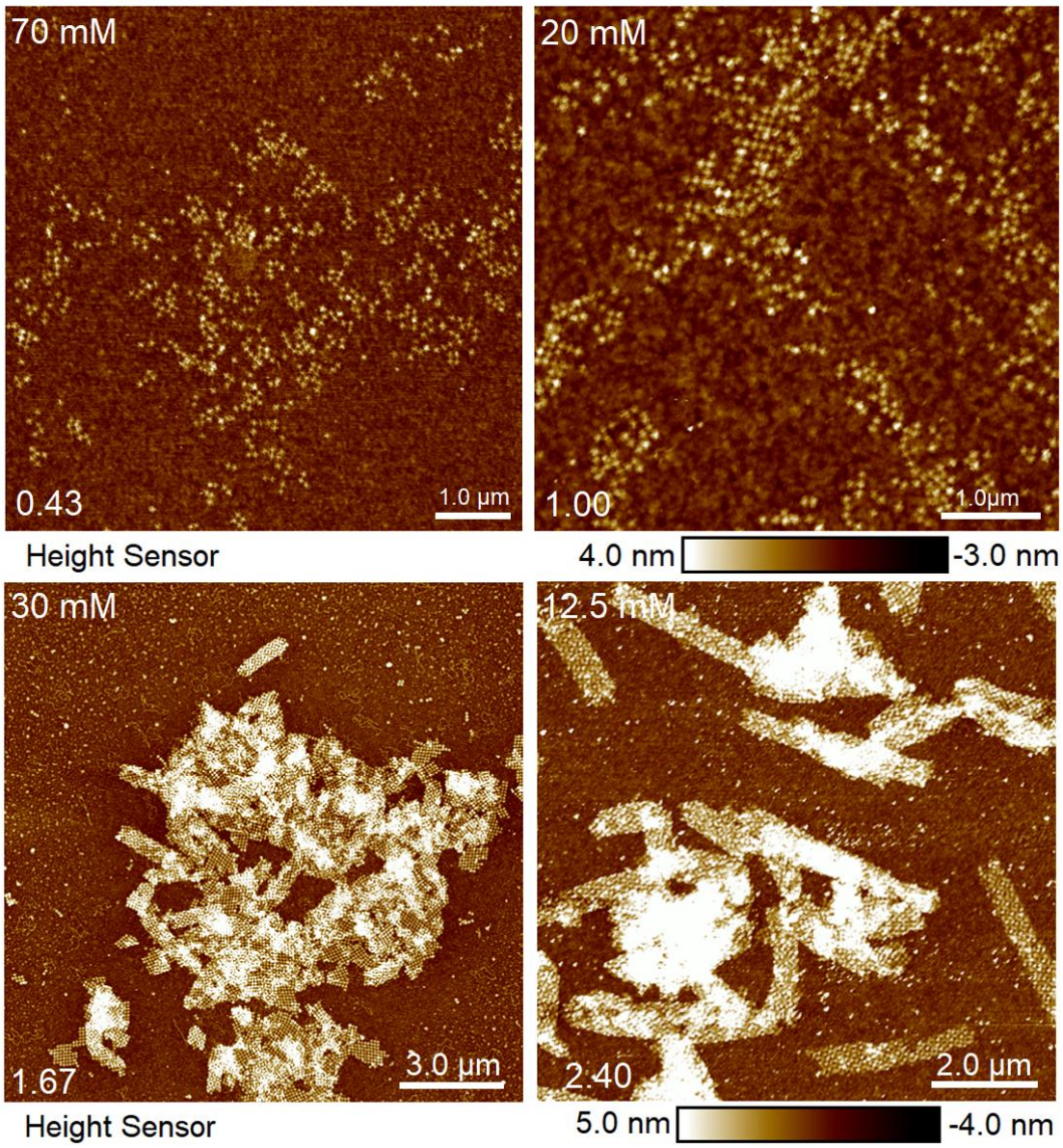

Figure 32. The effect of calcium ions for different magnesium, nickel and sodium concentrations on silicon surfaces. All samples have a calcium concentration indicated at the top-left corner of each AFM image. Also, the $[Mg^{2+}]$:$[Ca^{2+}]$ ratio is given on the bottom-left corner for each sample. On the upper row on the left, 30 mM of magnesium and 20 mM of sodium was used with an incubation time of 60 min. On the upper row on the right, 20 mM of magnesium, 6 mM of nickel and 50 mM of sodium was used with an incubation time of 120 min. On the bottom-left, 50 mM of magnesium, 2 mM of nickel and 20 mM of sodium was used with an incubation time of 240 min. On the bottom-right, 30 mM of magnesium, 7 mM of nickel and 150 mM of sodium was used with an incubation time of 60 min. A 10 nM TC-ST origami concentration was used, except for the rightmost sample on the bottom row, the origami concentration was 5 nM.

Although, some kind of ribbons were forming, no substantial improvement in lattice growth was obtained using calcium as the divalent cation. In conclusion, calcium ended up being hard to work with as only two type of samples could be prepared, either low amounts of origami or piled-up ribbons were obtained. Although, finding pile-ups from the chip can be based on luck as discussed in the beginning of this chapter. Also, deformed and unfolded origami were frequently encountered with increased incubation times, but barely any origami attached with shorter incubation. Possibly, a larger amount of origami have time to land on the surface with longer incubation times and, although, calcium seems to have a very poor surface binding ability on silicon, at least some origami get attached.

Very few lithium samples were prepared since none of the tried ionic conditions produced even reasonable connected structures. The smaller size of lithium compared to sodium makes the charge density higher but for a smaller area. Using lithium as the monovalent ion creates mostly separated origami and in total not many are attached to the surface, as shown in appendix F figure 48. Because of the smaller size of lithium, origami should be closer to the surface compared to, *e.g.*, potassium, but the smaller ionic radius might have led to more efficient screening of surface charge and therefore poor surface attachment for origami. Finally, the effect of incubation time on lattice formation is studied.

4.2.6 The effect of incubation time on lattice formation

The effect of incubation time on the 50 mM magnesium, 5 mM nickel and 250 mM sodium was studied as these ionic conditions produce easily a high amount of ribbons. The ribbons start already forming in 15 min with good enough conditions (salt combinations and concentrations) as seen from figure 33. The ribbons are the most intact around 30-45 min of incubation. Although, ribbons start forming already in 15 min, increased incubation times of around 30-45 min can help in fixing some of the lattice errors by, *e.g.*, creating more defined, smoother edges for ribbons, as judged from figure 33. A larger proportion of the origami will also have time to land on the surface to cover it, as discussed in the previous section (4.2.5) with calcium.

For some reason, the ribbons seem to disassemble around 90 min of incubation. Either the surface treatment of the chip could be wearing off, which is unlikely after binding has happened, or the ribbons might get broken and scattered because of added liquid on the sample during incubation to avoid drying. Although, lattice

assembly in liquid might also be affected when exposed to high ionic conditions for long periods of time. With increasingly long incubation times more salt build-up is encountered everywhere on the sample and on top of ribbons as can be seen from figure 33. The sample incubated for 240 min has more intact ribbons than the 90 min sample. It is likely that the aggregated salt in the 240 min sample attaches the origami more strongly on the surface and each other so the washing procedure is not able to detach as many origami as in the 90 min case. Also, the salt build-up is most likely restricting any further lattice assembly. Therefore, longer than 30-45 min incubation times should be avoided unless new energy sources are added to the interface, *e.g.*, by increasing temperature or vibration that would help avoid the formation of salt crystals on the surface.

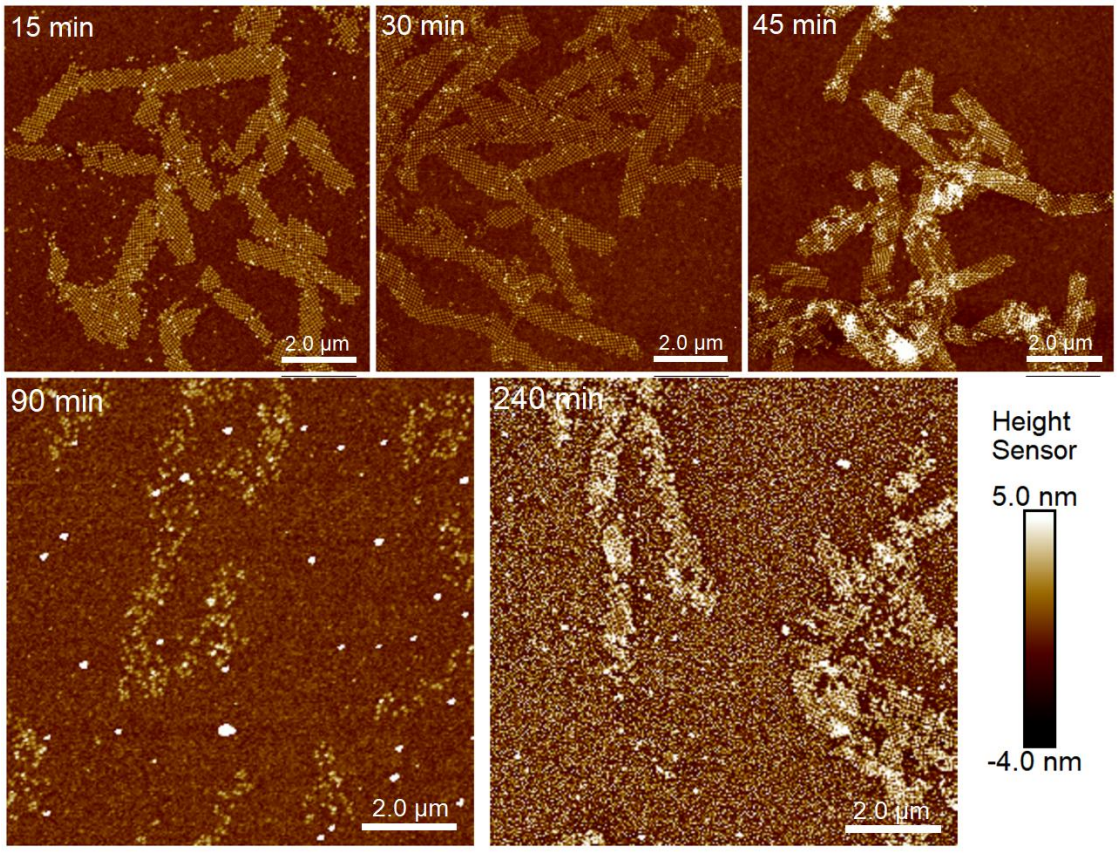

Figure 33. The effect of increasing the incubation time, given at the top-left corner of each image, for α-Si surface. Each AFM image represents an individual sample with 50 mM concentration of magnesium, 5 mM concentration of nickel, 250 mM concentration of sodium and 10 nM concentration of TC-ST origami tiles.

Figure 34 shows a similar set of samples for different salt conditions for increasing incubation times. Comparing the ionic conditions of 50 mM magnesium, 10 mM of nickel and 50 mM of sodium to those of figure 33, where the main difference is in the higher nickel concentration, we can see that the ribbons are well-defined and rather similar for every given incubation time. The only difference is that for the longest incubation times there is more salt build-up and the ribbons are more stuck together as well as multilayered, rather than single layered and evenly spread. We can not see a disassembling of ribbons at any stage as in figure 33. This observation suggests that increased nickel concentrations can be used to freeze origami structures on silicon.

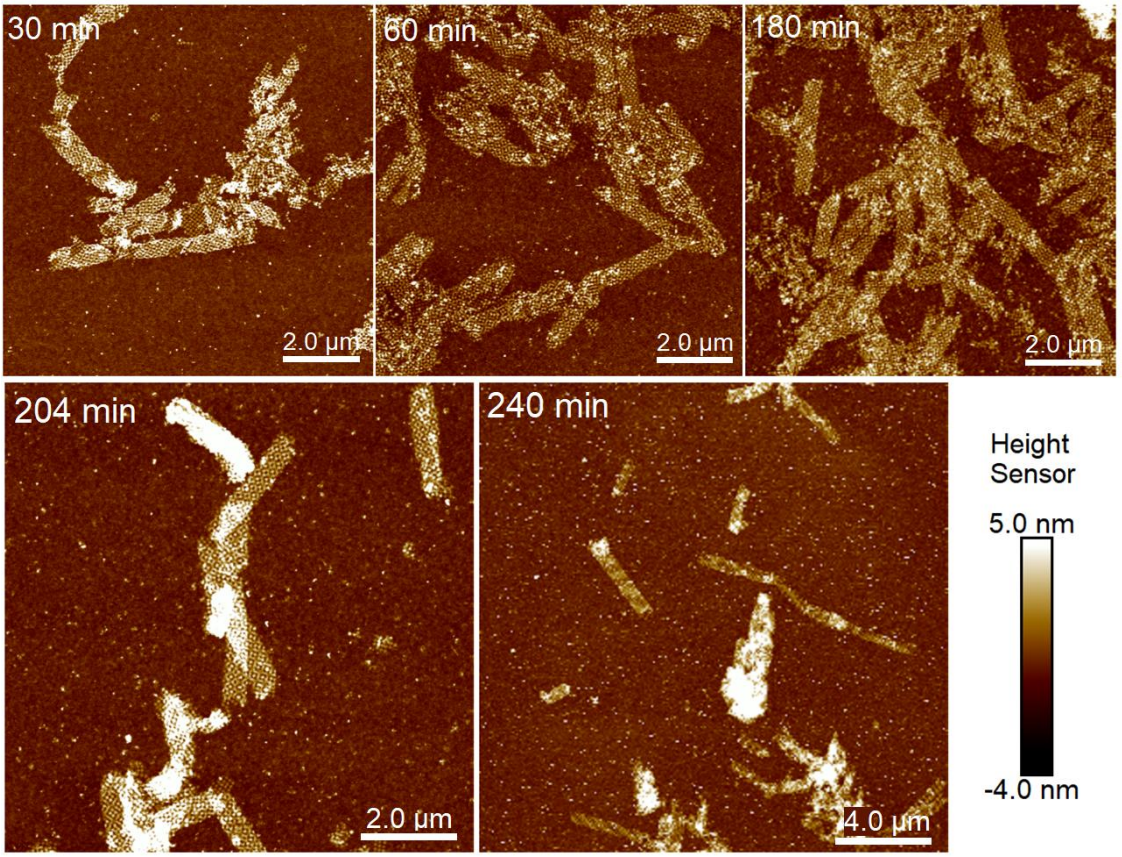

Figure 34. The effect of increasing the incubation time, given at the top-left corner of each image, on α-Si surface. Each AFM image represents an individual sample with salt concentrations of 50 mM of magnesium, 10 mM of nickel and 50 mM of sodium. The TC-ST origami concentration for each sample is 10 nM.

The agglomeration of lattices into drying patterns resembling shapes (of especially the 90 min sample) in figure 33 is also rather peculiar. Generally, longer incubation

times (with high enough mobility) make the origami drift into "islands" of separated origami rather than being uniformly distributed around the surface. This effect was also seen very clearly with the sodium experiments in section 4.2.2 in figure 23 for the samples with highest sodium concentration. In comparison, the lattice disassembly effect was not observed for the ionic conditions of figure 34. This is most likely because of the stronger binding ability of nickel and the aggregation of salts on the sample surface as well as on top of the ribbons.

Apparently, longer incubation time under the influence of monovalent cations can help in distributing origami on the silicon surface. A sample series of increasing the magnesium concentration for a fixed sodium concentration of 100 mM is presented in appendix F in figure 49. Comparing the sample with 200 mM magnesium, 100 mM sodium concentration and 40 min incubation time with a sample from section 4.2.2 figure 22 having the same ionic conditions with only 15 min incubation time, there is a clear difference. The sample with the longer incubation time has significantly less aggregated origami. Unfortunately, solely increasing the incubation time as well as monovalent cation concentration does not transform ribbons into neat 2D lattices, but only spreads the origami around with less connections between origami.

In general, longer incubation times (>60 min) endorse salt aggregation, the scattering of origami and formation of agglomeration patterns when combined with sufficiently high monovalent cation concentrations. If longer incubation times are needed, especially the nickel concentration should be kept low to avoid structures from getting too stuck on the surface. Since ribbons are most likely formed by lattice assembly in liquid, the next section is dedicated for studying the lattice assembly kinetics in the liquid environment. This is achieved using the liquid AFM. Furthermore, the number of blunt-end interactions is decreased to see if lattice assembly can be restricted only on the wanted surface by adjusting the interactions between origami.

4.3 The effect of the number of blunt-end interactions on lattice assembly

In storing conditions (low magnesium buffer), the blunt-end interactions between origami are not strong enough to begin full lattice assembly in liquid. Higher salt concentrations, stronger divalent cations, *e.g.* nickel, as well as some surfaces like mica can enable the liquid assembly. The aim of the thesis is to obtain single-layered, error-free 2D lattices, sometimes referred to as monolayers, that cover the whole silicon surface instead of the elongated ribbons that were encountered in the previous section. Therefore, the number of blunt-end interactions between origami were adjusted trying to restrict the lattice assembly happening without the presence of a surface, *i.e.*, the solid-liquid interface.

4.3.1 AFM imaging in air: the effect of blunt-end interactions

Section 4.2 showed that elevated salt concentrations are required to deposit origami on the silicon surface compared to mica. Different salt combinations and concentrations were tried for the origami designs having 0×4, 2×4, 3×4, 4×4, 5×4 and 6×4 blunt-ends on each origami arm. The preceding notation is explained in detail in section 2.2.1. As shown in figure 35, when nickel is excluded and the concentration of magnesium is brought down to 25 mM and the concentration of sodium to 100 mM, the lower the number of blunt-ends the more origami stick on the silicon surface. In these salt concentrations designs having 4×4 or more blunt-ends barely attach on the surface. To attach origami designs with a higher number of blunt-end interactions on a silicon surface, higher salt concentrations are needed as discovered in section 4.2.

As shown in appendix F in figure 50, decreasing the amount of magnesium from the concentration of 25 mM to 20 mM for the 3×4 design, has a similar effect as found earlier in section 4.2.1. Higher magnesium concentration leads to stronger origami-origami attraction and in the end more clumped structures have formed on the surface. The addition of sodium for the same design also behaves as expected, as shown in appendix F in figure 51. Sodium is able to screen some of the surface charge without increasing attractive forces between origami, ending up in a more scarcely covered surface, as discussed in section 4.2.2. One more incubation time studying experiment was done for the 3×4 TC-ST design, which is introduced in appendix F in figure 52. Here a longer incubation time of 30 min compared to

that of 10 min, leads to bigger assembled lattice structures. Although, the formed structures have grown in size, the surface coverage has also decreased, leaving a lot more empty space between the ordered structures. When the sodium concentration is increased to 200 mM, the surface is more covered already after 30 min of incubation. Increasing the incubation time to 60 min fills the surface completely, but has a rather similar amount and size of lattice structures between randomly oriented origami. Therefore, the surface coverage can be increased by adjusting the monovalent cation concentration as well as the incubation time.

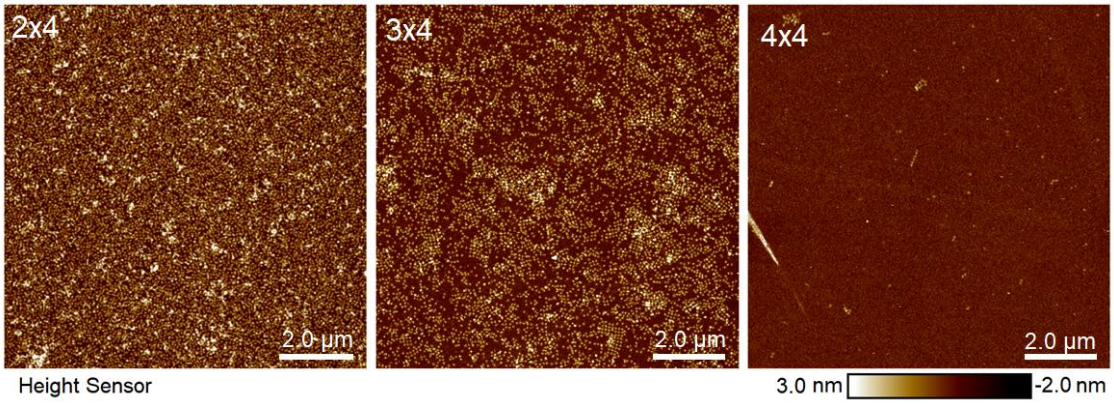

Figure 35. AFM imaging in air performed for the 2×4, 3×4 and 4×4 blunt-end TC-ST origami designs in 25 mM magnesium concentration and 100 mM sodium concentration with 10 min incubation time. The origami concentration for each sample is 10 nM.

4.3.2 AFM imaging in liquid: the effect of blunt-end interactions

Since a good coverage of origami on the silicon surface was obtained with a 20 mM magnesium and 100 mM sodium concentration for the 3×4 blunt-end design (see figure 50 in appendix F), these conditions were chosen for the first liquid imaging experiments. As shown in figure 36, in these conditions origami attach together in liquid and land on the surface in clumps that do not move significantly. Occasionally, single origami land on the surface but do not move at all. To increase origami mobility on the surface, and to enforce lattice assembly, the sodium concentration was increased in the following liquid imaging experiments to 200-300 mM. A minimal amount of movement is seen even with the single origami landing on the surface. After the surface has been covered with origami, they do not move further.

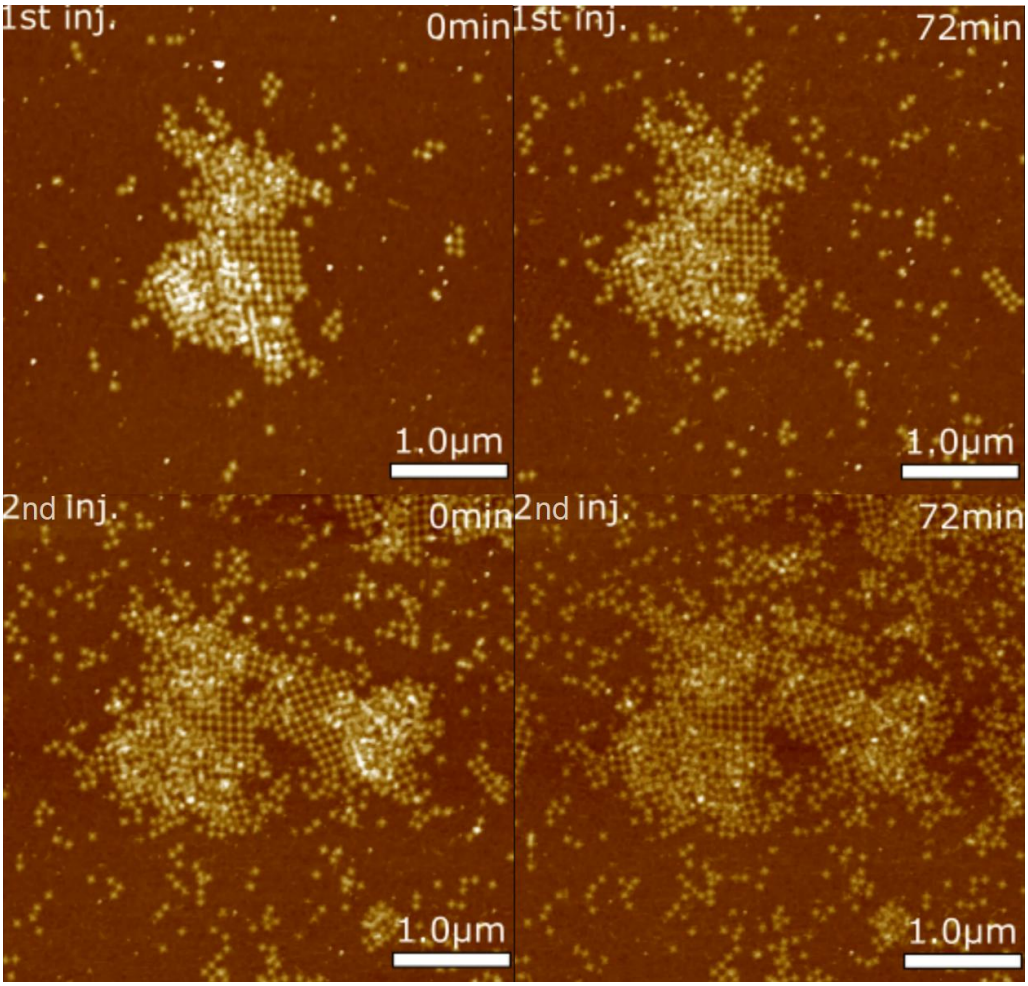

Figure 36. Liquid AFM imaging for the 3×4 blunt-end TC-ST origami design in 20 mM magnesium concentration and 100 mM sodium concentration. Origami was injected in total two times during imaging. The top row shows the results for the first injection (1st inj.) at a time of 0 min and 72 min after the injection. The bottom row shows the same time marks for the second injection (2nd inj.).

Although, the surface gets considerably more covered with a monolayer of origami, almost no lattice assembly is seen. For this reason, the magnesium concentration is lowered to initiate lattice assembly between individual tiles. In 17.5 mM magnesium and 300 mM sodium concentration the origami do not really move. A liquid AFM image in these conditions is provided in figure 37. When the magnesium concentration is brought down to 12.5 mM concentration with 300 mM sodium concentration, the origami do not attach on the surface anymore, but can be seen as lines or small parts of origami that disappear from the AFM screen after a few more lines are imaged. A higher sodium concentration is known to screen the surface of charge

rather than creating salt bridges to attach origami like magnesium does as discovered in section 4.2.2. Since 17.5 mM already glues the origami very tightly on the surface, the sodium concentration is again brought down to try to lower screening of the surface charge and get the origami to attach on the surface. When the sodium concentration is lowered to 100 mM, the origami are again able to attach and land on the surface. Similar experiments are conducted and continued in section 4.4.1 with controlled temperature.

Now the movement of origami has been optimized, but improvement in lattice assembly is still required as only small connected structures are forming. This is solved by switching to the 4×4 blunt-end design, having one additional pair of blunt-end interactions on each arm of origami to make origami attach more strongly to each other. Surprisingly, instead of enhancing lattice assembly, the origami detach again from he surface. This implies that the origami are again attaching together too strongly above the surface and that optimization of ion concentration is required for each blunt-end design individually. More magnesium (or less sodium) is needed to attach the origami on the surface for the 4×4 design compared to the 3×4 design. Table 2 was composed to express the best ionic ranges for the designs in liquid more conveniently.

Table 2. A table of the tried ionic conditions for the liquid imaged blunt-end TC-ST designs with descriptions of effects on lattice assembly and origami adsorption.

Design	**[Mg^{2+}]**	**[Na^{+}]**	**Description**
3×4	20 mM	100 mM	Clumps, no movement
	20 mM	200-300 mM	More coverage, no movement
	17.5 mM	300 mM	More coverage, no movement
	12.5 mM	300 mM	Do not attach on the surface
	12.5 mM	100 mM	Attach, but no connections
4×4	12.5 mM	100 mM	Do not attach on the surface

The liquid imaged chips were dried after each imaging session using the washing procedure described in section 3.2. As shown in figure 37, even the more gentle washing and drying protocol, compared to the used washing protocol introduced in section 3.1, is able to remove most of the origami from the silicon surface. A more

efficient washing procedure is needed to allow for preparation of dried samples with lower ionic conditions than what were used in section 4.2.

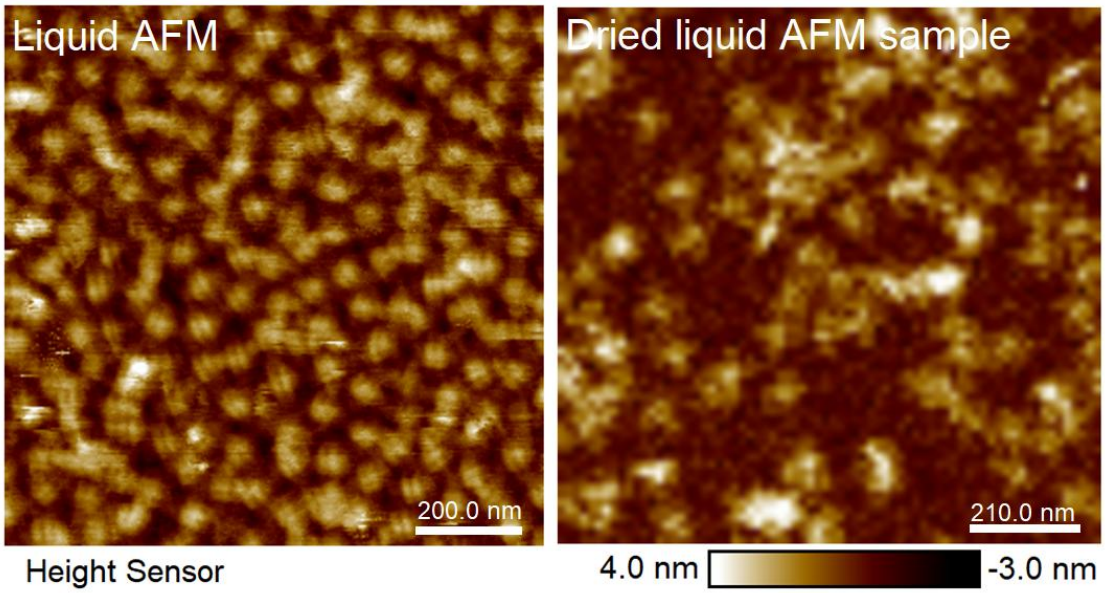

Figure 37. On the left, the final image of liquid AFM imaging done for the 3×4 blunt-end TC-ST origami design in 17.5 mM magnesium and 300 mM sodium concentration. On the right, image of the dried chip used during the liquid imaging. The sample was dried using the washing procedure described in section 3.2.

4.4 Temperature control for liquid and air AFM imaging

Based on the findings from section 4.3, the 0×4 and 2×4 designs are excluded from these sets of experiments. The 0×4 design is not able to produce a fishnet lattice because of the lack of any blunt-ends in the design and instead results in close-packing. We are more interested in the designs having more than 2×4 blunt-ends, since stronger and more stable connections between origami are wanted. The temperature-controlled liquid AFM imaging experiments presented in the following section were carried out by Dr. Charlotte Kielar from HZDR with Dr. Kosti Tapio.

4.4.1 AFM imaging in liquid: the effect of temperature on lattice assembly

Since this section contains many series of large figures with subtle differences between them, they are presented in the appendix. Liquid imaging was performed for designs having more than 2×4 blunt-ends in different temperatures to study the effect on lattice assembly. One thing to note with these experiments is that the liquid imaging interferes with lattice assembly when faster scanning frequencies are used. This effect is demonstrated in appendix F in figure 53. An area was scanned using 5 Hz, 10 Hz and 20 Hz scanning frequencies per line, leaving behind a more empty spot when the scan size is increased. To avoid interfering with the results, scanning frequencies above 5 Hz should be avoided. A sodium concentration of 150 mM was chosen for the following experiments after careful optimization at HZDR.

The temperature controlled liquid AFM results for the 6×4 blunt-end TC-ST origami design with 12.5 mM magnesium and 150 mM sodium concentration are shown in appendix G. A single sample with the 6×4 blunt-end design was incubated for approximately 1678 s in each temperature. Mainly, the first and last of the AFM figures are presented in each temperature to follow the main development in lattice growth. The images for the 6×4 design at 25 °C show small lattices and paired origami landing on the surface. Larger structures do not move on the surface, but some movement and reorientation can be seen with the single and paired origami, judging by any two images taken after one another. Some of the single origami are even detaching from the surface. When the temperature is increased to 30 °C, the surface starts to get more covered. The slightly bigger connected structures have frozen in arbitrary positions and angles compared to each other and do not move on the surface but stick to where they happen to land. The only movement on the surface is happening due to the single origami reorienting themselves, trying to find the most energetically favorable position between the bigger structures. Unattached origami keep floating on top of the origami that are stuck on the surface, but since the surface is mostly covered they do not get too tightly attached to build a second layer. The biggest difference in the 35 °C case is that the holes in the monolayer have been mostly filled up. Unattached origami are still trying to find a place to land on and some of them have even gotten stuck on top of the first layer of origami. There are a few spots where the unattached origami floating above the first layer have landed on the structures creating a double layer. These areas of double layered

origami can be seen as higher, whiter spots in the AFM figures that do not disappear anymore. These spots can also be the result of salt aggregation, but since there is a clear excess of origami floating around, the higher spots are most likely the result of double layering. Since the bottom most layer of origami has already been well established, increasing the temperature further to 40 °C and 45 °C, does not have a big effect on lattice assembly. The higher temperatures only have an effect on building the second layer of origami further. To avoid a double layer from forming, the origami concentration could be decreased.

The temperature controlled liquid AFM imaging results for the 5×4 TC-ST origami design with 12.5 mM magnesium and 150 mM sodium concentration are presented in appendix H. Compared to the results of 6×4 design at 25 °C, the 5×4 design creates significantly bigger lattice structures in the same conditions. A lot larger lattices are seen at the end of the 25 °C experiment set than what were seen with the 6×4 blunt-ended design. As observing bigger lattices for weaker interactions between origami seems counter intuitive, this observation might simply be the result of luck based place dependency on the chip, as discussed in the beginning of section 4.2. Again, the surface gets more covered in the 30 °C case. A double layer is already starting to form. Especially, on top of the larger lattices a second layer of origami is already well established. The surface is not quite as covered as for the 6×4 design with the same temperature, but a large portion of the surface is already full. At 35 °C the surface gets covered completely with no holes left between origami. The bottom layer of origami does not move on the surface, but an excess of origami is floating over the first layer, repeatedly attaching and detaching. The situation is very similar to that of the 6×4 design at 35 °C. The results at 40 °C for the 5×4 design, appear similar to those at 35 °C. The only difference between the 6×4 and 5×4 design at 40 °C is that the double layering of origami is not quite as excessive for the 5×4 design. The double layer does not start forming before there are big enough lattices with constant enough conditions and the most favourable binding positions on the surface are covered. Possibly, the lower amount of blunt-ends makes finding a favourable position on top of other origami more difficult. At 45 °C the double layer still has not formed remarkably.

Figure 38 demonstrates the difference in double layer formation between the 5×4 and 6×4 design at 45 °C. From the sample with the 6×4 design it is easy to see that the double layer forms by close-packing the middle parts of origami together. This

phenomena is also repeatedly seen with mica samples, as was also the case for the mica sample presented in section 4.1 in figure 19. Furthermore, the 6×4 design has slightly larger lattice structures present on the surface as well as cleaner connections between neighboring origami compared to the 5×4 design. Although, the quality of lattice assembly of both designs is rather poor and disordered in this temperature. Most likely, this results from introducing too much thermal energy at 45 °C as this no longer allows the blunt-ends to form lasting connections between origami.

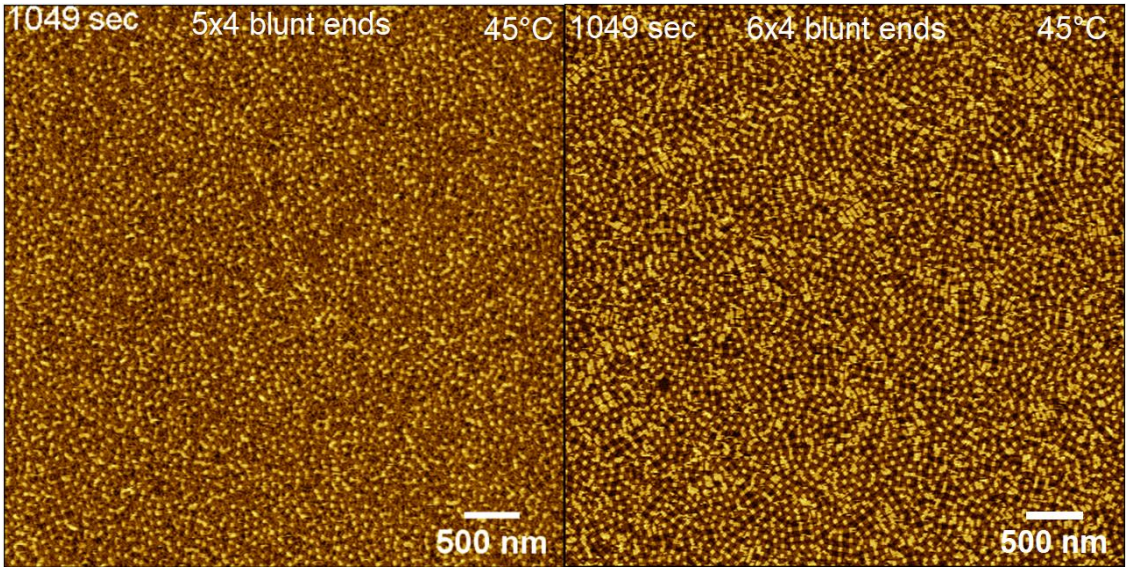

Figure 38. On the left, the final image of liquid AFM imaging done for the 5×4 blunt-end TC-ST origami design in 12.5 mM magnesium and 150 mM sodium concentration at 45 °C. On the right, the final image of liquid AFM imaging done for the 6×4 blunt-end TC-ST origami design in the same conditions. The close-packing of the middle parts of the STs in double layers can be clearly seen from the 6×4 design image on the right.

Since the lattice quality is easier to judge from closer images, the following experiments were imaged as 5 µm scans instead of 10 µm. Appendix I introduces the temperature controlled liquid AFM results for the 4×4 blunt-end TC-ST origami design with 12.5 mM magnesium and 150 mM sodium concentration. At 25 °C the surface gets covered almost fully before the final image for this condition is taken. As for the 6×4 and 5×4 designs, a minimal amount of movement on the surface is observed for the 4×4 design. The area imaged does not have larger than 10 origami containing lattices unlike the other two designs already presented in the same temperature. At 30 °C the surface gets a bit more covered, but other than a few holes on the monolayer changing places, not a lot is happening in this temperature.

In 35 °C the surface gets a bit more covered but all observed changes are minor. At 40 °C almost all of the holes in the monolayer have disappeared. Some small lattice connections can be seen, but overall the surface looks rather disordered and tightly packed. The situation stays similar at 45 °C and almost no double layering can be seen on the monolayer.

The temperature controlled liquid AFM results for the 3×4 blunt-end TC-ST origami design with 12.5 mM magnesium and 150 mM sodium concentration are given in appendix J. The results for the 3×4 design are very similar to those of the 4×4 design until temperature of 45 °C is reached. Until then, the 3×4 design has a little less crowded surface, has a bit more order in lattice assembly and has a few origami units larger structures forming. This can again be the result of area dependence, since there are less origami present than what was available for the 4×4 design. The 3×4 design does not achieve a monolayer fully covering the surface during the whole experiment set. Surprisingly, all origami completely detach from the surface when the temperature is increased to 45 °C. When the temperature is still increased to 50 °C the origami land back on the surface and continue forming a monolayer. If the origami had not completely detached from the surface at 45 °C, most likely, a better coverage of origami would have been achieved until the final point of the experiment. The unexpected detachment of origami might have something to do with the lowered number of blunt-ends. Although, depending on the origami design and buffer conditions, some structures have melting temperatures between 40-100 °C [82–85], the sudden detachment should not be the result of irreversible unfolding of the structure as the origami land back on the surface unharmed. Nevertheless, it is clear that too high temperatures should not be used to avoid the detachment phenomena as well as the formation of double layers on the first layer of origami. A rather good coverage of origami on the surface is achieved already in temperatures from 35 °C to 40 °C for all origami designs. When comparing the final images of all of the tested blunt-end designs, the 6×4 design possesses the highest lattice quality, order and largest structures. Based on these findings, the 6×4 design combined with a temperature range of 35-40 °C was chosen for further experimenting in dried conditions that is discussed further in section 4.4.3. Next, lattice assembly of the NTC-ST origami is studied in liquid conditions.

4.4.2 AFM imaging in liquid: NTC-ST

As discussed in section 4.1, the NTC-ST was imaged in liquid conditions to study the preferential growing direction of the ST origami. As shown in the top row of figure 39, under 12.5 mM magnesium and 150 mM sodium concentration, the NTC-ST design mainly forms short strings of origami. Also, it took a considerably long time for the origami to at-

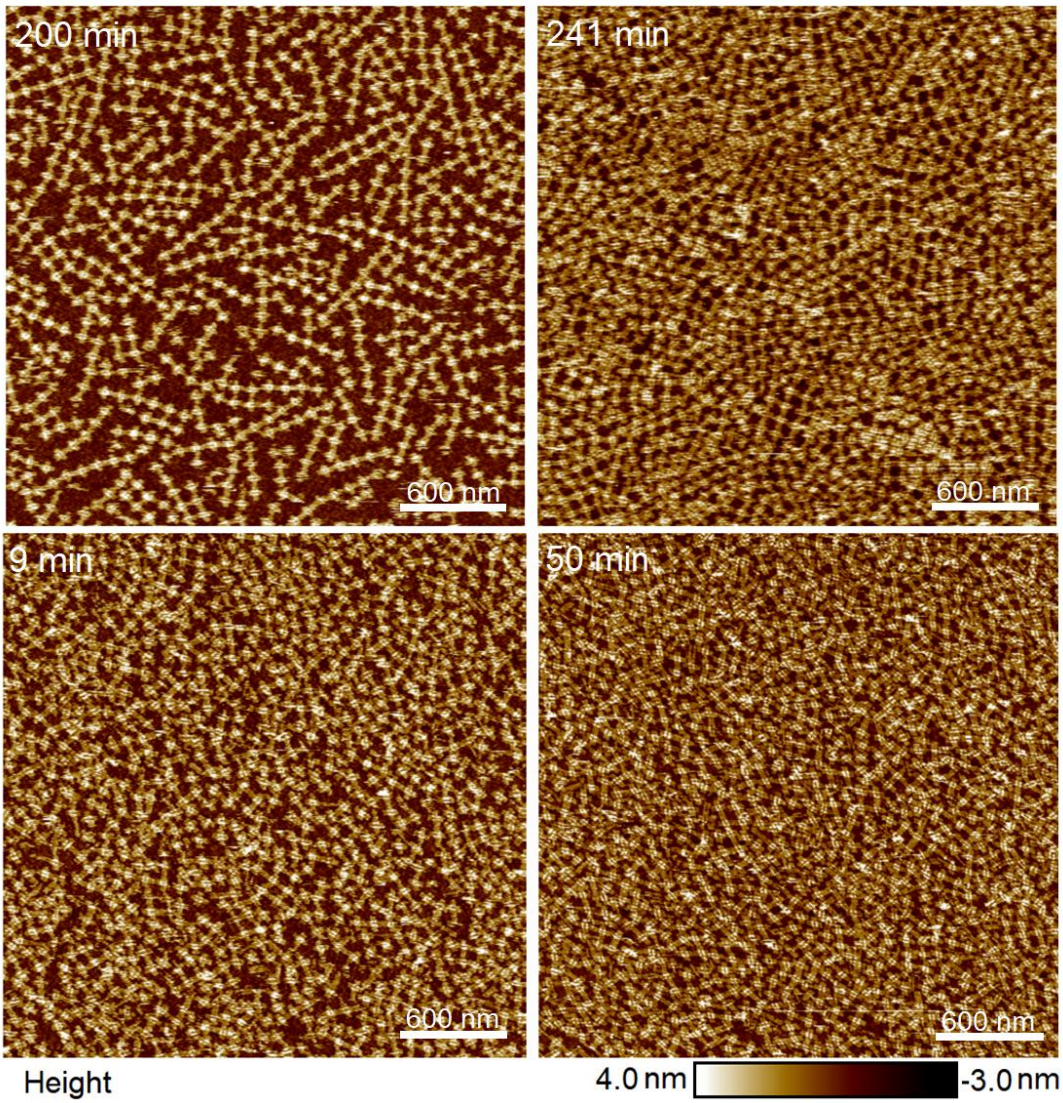

Figure 39. Liquid AFM imaging of the NTC-ST origami under 10 nM tile concentration. The top row shows the NTC-ST in 12.5 mM magnesium and 150 mM sodium concentration. The bottom row shows the NTC-ST in 25 mM magnesium and 150 mM sodium concentration. The times indicated at the top-left corner of each image represent the times that have passed after origami injection.

tach on the silicon surface. First structures were observed on the surface after 200 min of liquid AFM imaging. Growth in two directions is only observed when two strings of origami attach together side by side. Therefore, the structure exhibits even stronger affinity to unidirectional growth when the design is NTC. At the bottom row of figure 39, the magnesium concentration is elevated to 25 mM in order to get the origami to attach more strongly on the surface. In these conditions, barely any connected origami are seen. Although the surface gets packed faster. Since in general the NTC-ST design grows even more strongly in one direction and suggests weaker binding interactions between neighboring origami compared to the TC version, it is not studied further.

4.4.3 AFM imaging in air: the effect of temperature on lattice assembly

Since a good surface coverage of origami for the 6×4 blunt-ended design was already established in 35 °C, having still a minimal amount of formed double layering, it was chosen for the following experiments. Having the magnesium concentration fixed at 12.5 mM, the concentration of sodium, the concentration of origami and incubation time can be changed to drive lattice assembly into forming a tight monolayer on the silicon surface. It was also reported by Xin *et al.* that the DNA origami concentration plays a key role in the development of lattice order [5]. The dried samples were treated with nickel right after incubation to fix or freeze the formed origami structures on the silicon surface, as described in section 3.3. The effect of nickel fixing on the amount of adsorbed origami on the silicon surface is presented in figure 40. As can be seen, the sample without nickel fixing has almost no origami left on the surface whereas the nickel fixed sample is completely covered. Therefore, the nickel fixing step is crucial in preventing the origami from being washed away during the sample washing procedure.

For a fixed origami and sodium concentrations the incubation time can be increased to obtain a fully covered surface for almost any combination of concentrations. As shown in figure 41, for a combination of 10 nM tiles and sodium concentration of 225 mM the silicon surface gets fully covered around 200 min of incubation for the 6×4 design. If the sodium concentration is increased to 400 mM, as in figure 42, the incubation time needs to also be scaled upwards to cover the whole surface. Since a double layer starts to form on the monolayer, the incubation time should be kept under 8 h. Therefore, for 400 mM sodium concentration the surface gets fully

covered somewhere between 5 h and 8 h.

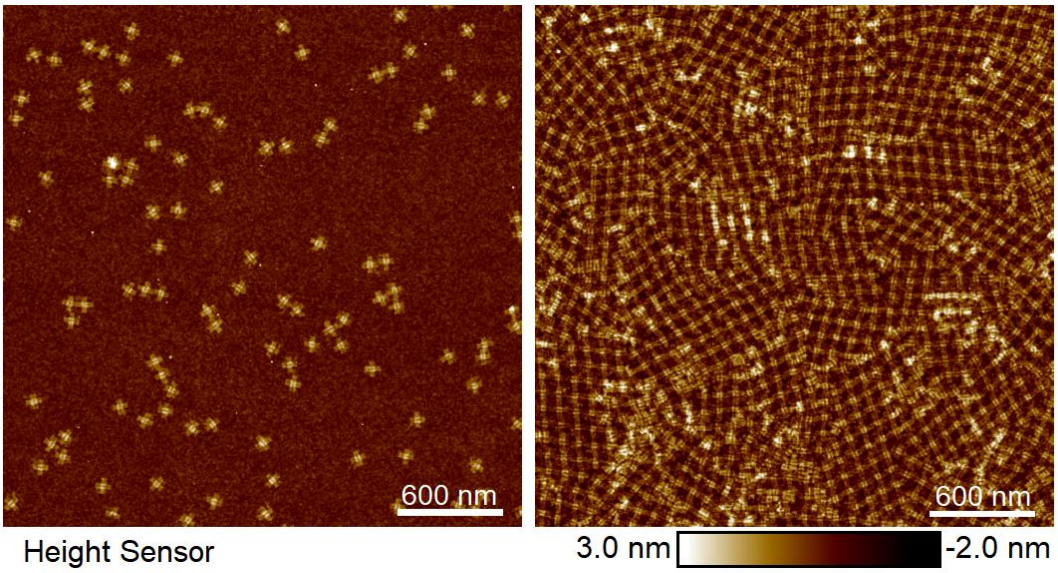

Figure 40. Demonstration of the importance of nickel fixing before drying for the amount of adsorbed origami on silicon. On the left, a sample without nickel fixing. On the right, a sample with the same parameters with nickel fixing. Both samples were prepared at the same time having a 6×4 TC-ST origami concentration of 10 nM, magnesium concentration of 12.5 mM, sodium concentration of 400 mM and incubation time of 5 h in 35 °C.

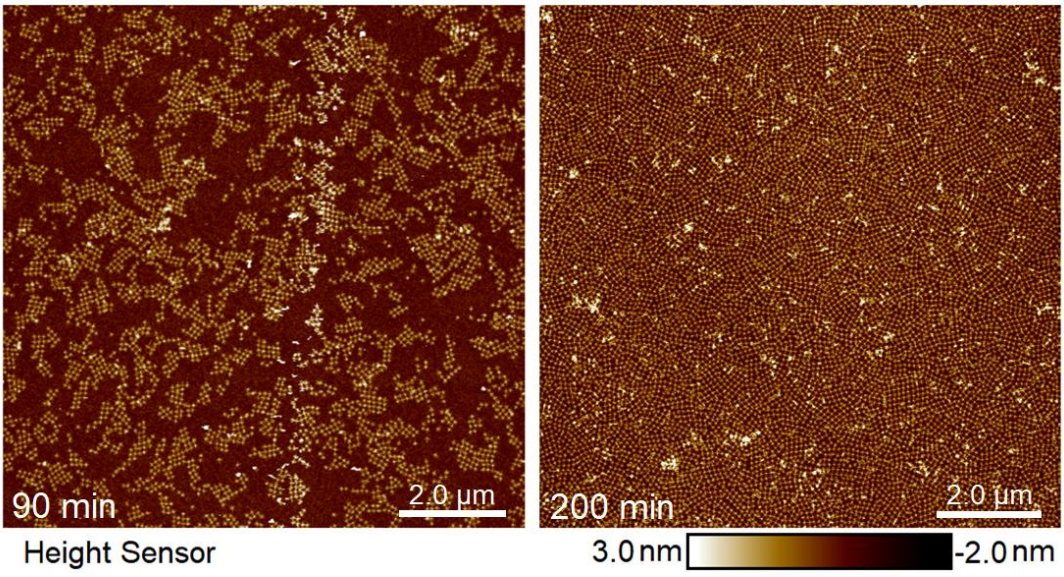

Figure 41. AFM imaging in air for the 6×4 blunt-end TC-ST origami with 10 nM tile concentration in 12.5 mM magnesium and 225 mM sodium concentration at 35 °C for 90 min and 200 min incubation times, specified at the bottom-left corner. Nickel fixing, described in section 3.3, was used for both samples.

Another option to fill up the silicon surface for a fixed sodium concentration and incubation time is to fill up the surface more quickly by increasing the origami concentration, as shown in figure 43. Here, increasing the origami concentration to 20 nM for a sodium concentration of 400 mM, the incubation time of only 200 min gets the surface fully covered. Therefore, increasing the origami concentration is required for a fixed sodium concentration if lower incubation times are needed. The 20 nM sample has high clumps on top of the surface covering monolayer, seen as higher spots in the AFM image. These can be the result of excess origami landing on the surface or an excess of nickel from the fixing step of the washing protocol as the amount of nickel used is yet to be optimized. Peculiarly, most of the high spots are found only at the edges of the fully formed lattice structures which have grown together resembling a polycrystal pattern.

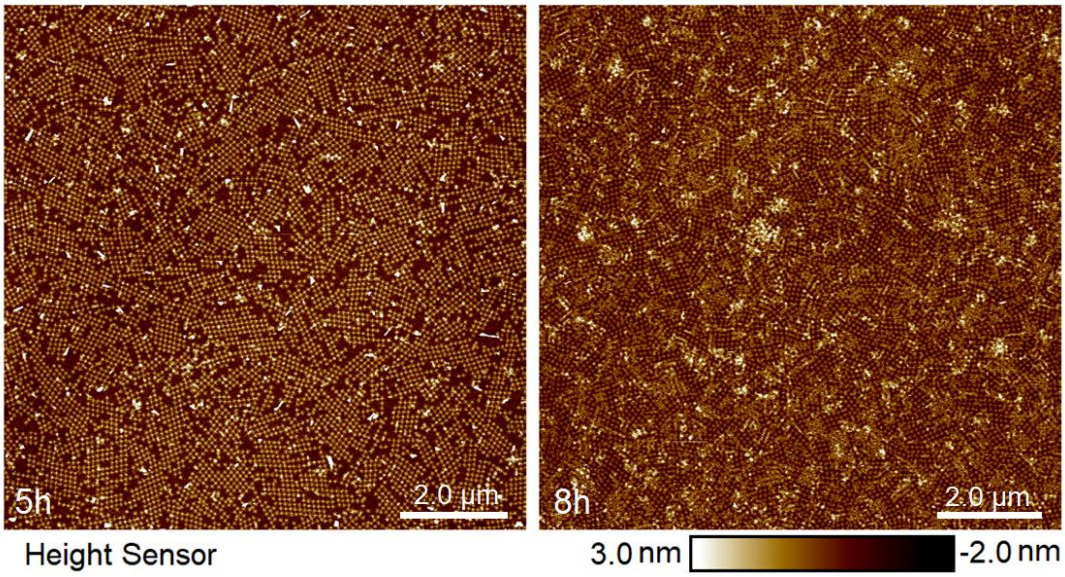

Figure 42. AFM imaging in air for the 6×4 blunt-end TC-ST origami with 10 nM tile concentration in 12.5 mM magnesium and 400 mM sodium concentration at 35 °C for 5 h and 8 h incubation times, specified at the bottom-left corner. Nickel fixing, described in section 3.3, was used for both samples.

The sample presented on the left in figure 42 is already very close to the coverage and quality of monolayered lattice that was produced earlier on mica as presented in section 2.4 in figure 10. Furthermore, the sample presented on the right in figure 43 has no space between the polycrystal domains than what are seen on mica. Although, the silicon surface is completely covered with conjoined polycrystals, each polycrystal edge has aggregations that are most likely the result of the nickel fixing step. Later,

the nickel concentration was optimized to avoid salt aggregating on the monolayer and obstructing further ordering of lattices. In the future samples, the effective nickel fixing concentration is brought down to 10 mM (from 20 mM) and the time is reduced to 20 s (from 30 s) to avoid formation of aggregations on the monolayer.

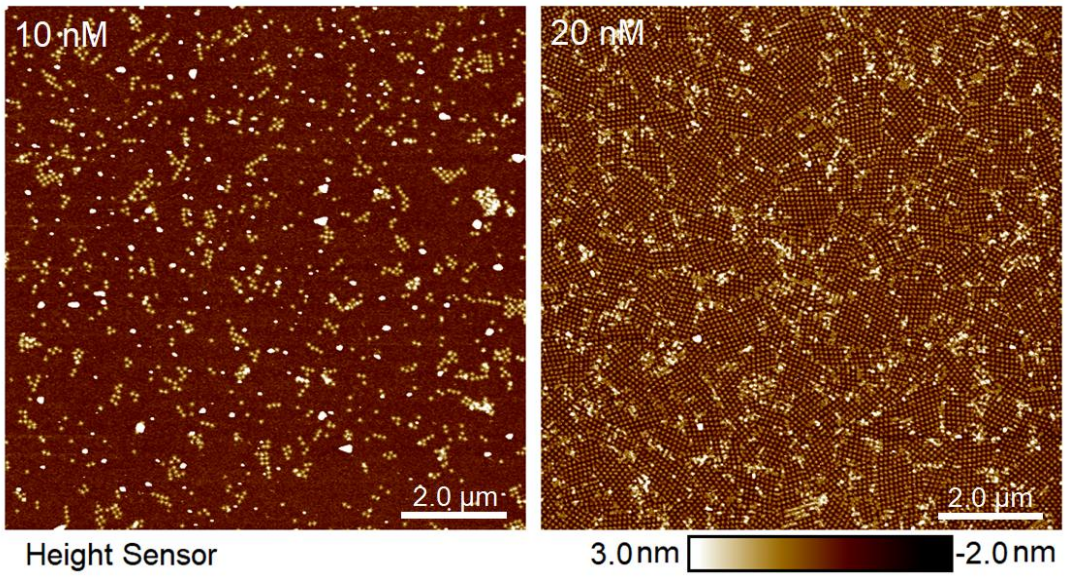

Figure 43. AFM imaging in air for the 6×4 blunt-end TC-ST origami in 12.5 mM magnesium and 400 mM sodium concentration at 35 °C for 200 min incubation time and tile concentrations of 10 nM and 20 nM, specified at the top-left corner. Nickel fixing, described in section 3.3, was used for both samples.

5 Conclusions

This thesis provides a full study of the fishnet lattice formation kinetics on a silicon surface with the blunt-ended TC-ST origami. Both, liquid and dry AFM imaging were utilized. In addition, a cryo-EM experiment was performed for determining the liquid assembly of the ribbon and tubular lattice structures in room temperature (RT), in higher ionic conditions and repeatedly in the presence of nickel. To our knowledge, similar studies have not been done on the silicon surface. Therefore, the thesis provides a lot of new information for the benefit of creating new negative-refractive index metasurfaces using the DALI protocol.

In total, the effect of eight parameters on lattice assembly were studied including the effect of ion type and concentration, incubation time, number of blunt-ends in the design, twist-correction of origami, surface roughness, origami concentration and temperature. Also, two different surface treatment processes were tested for silicon to obtain a negative surface charge: the O_2 plasma treatment with RIE and the basic piranha. Differences between treatments regarding surface attachment or lattice assembly were not observed. Two types of silicon surfaces, sc-Si and α-Si, were used to study the effect of surface roughness on origami attachment. Minor differences between the surface types were seen in the amount of attached origami and their distribution on the surface in the favor of the smoother sc-Si surface when only magnesium was introduced (see section 4.2.1). Nevertheless, any differences become indistinguishable when the optimized monolayer protocol, described in section 3.3, is used. Surface roughness can be an important factor in origami adsorption but for roughnesses between 0.2-1 nm any differences are neglectable.

Out of the tried ions, magnesium and sodium proved to be the most useful for the attachment of origami and for achieving the best lattice quality for the monolayer. In addition, nickel was found to be essential in the sample washing procedure since its absence results in decreased surface coverage and detachment of most of the origami. Calcium and lithium did not have a positive effect on lattice assembly on silicon as calcium deforms the origami after longer periods of time and samples containing lithium expressed poor origami adsorption. When sodium was replaced

with potassium, lattice structures were found to have a higher number of point defects or holes, *i.e.*, detached single origami in the middle of the fishnet lattices. Most likely, the larger size of the potassium ion resulted in steric hindrance interactions between origami and the surface leading to poor surface adsorption. Although, depending on the desired lattice structure, potassium could be utilized for obtaining a lower surface coverage of origami or for compensating some of the strong multilayering effects often caused by nickel.

In RT, generally higher ion concentrations and the presence of nickel during incubation are required to properly initiate lattice assembly. Although, this results in lattice assembly already in liquid instead of the surface and the formation of mainly ribbons and tubular structures. To avoid lattice assembly in liquid and to restrict it only on the surface, either the number of blunt-end interactions in the ST arms needs to be reduced or additional heating is required during incubation to achieve a single monolayer of lattice throughout the whole chip. Decreasing the amount of blunt-ends in the design leads to lowered binding strength between individual origami and therefore, lattice assembly on the surface becomes more energetically favourable. Increasing the temperature to about 35 °C during incubation combined with lower divalent salt concentrations also prevents liquid assembly, as the origami are less attracted to each other in lower concentrations of divalent cations, and in general have more thermal energy. Also, the thermal convection of the fluid prevents origami from being bound strongly together without the presence of a surface. In addition, the environmental chamber introduces slight vibration during incubation, which further increases the kinetic energy of the origami.

Regarding the sufficient ion concentrations of magnesium and sodium, similar amounts to those used on mica can also be used on silicon when proper heating is applied. Magnesium concentration of 12.5 mM is sufficient for creating similar monolayers on silicon than what are seen on mica [6] (see section 2.4 figure 10). Furthermore, there remains an interplay between the used sodium concentration, origami concentration and incubation time to acquire a fully covered monolayer of fishnet lattice as introduced in section 4.4.3. Specifically, one of the best parameter combinations consists of 400 mM sodium concentration, 10 nM origami concentration and a 5 h incubation (in 35 °C and with 12.5 mM magnesium). This combination is able to produce a tight fishnet monolayer throughout the silicon chip having a polycrystalline nature and a domain size similar to the one obtained on mica [6].

Some differences in between areas on the chip can still occur, as discussed in the beginning of section 4.2, but in general the current protocol provides rather consistent and uniform, monolayered fishnet lattices.

Also, the effect of twist-correction on the lattice assembly kinetics was studied. Although, the twist-correction of some origami designs can lead to a preferred direction of lattice growth [81], in the case of the blunt-ended TC-ST a completely opposite behaviour was detected. The used ST design expresses some level of preferred growing direction in both of the NTC and TC forms, but with the NTC-ST this behaviour gets emphasized. Most likely, the floppiness of the NTC-ST only allows certain orientations between origami, *e.g.*, a connection only between arms that form the top rectangle of the cross (see sections 2.2.1 and 4.1). When the TC-ST is applied, lattice assembly in all directions increases. Although, some preferred connections between arms are still noticeable (see section 4.1), likely because of the preferred binding energies between certain blunt-ends, the string-like growth for the TC-ST is less substantial. Also, the additional heating during incubation is able to lower the effect further by randomizing the connection orientation inside formed lattices through increased available energy. If this behaviour needs to be completely removed, the TC-ST origami can be redesigned to avoid more energetically favourable arm connections between origami, since they depend on the base sequences of the used blunt-ends as discussed in section 2.2.1.

The unused scaffold loop included in the ST origami design, referred to as a "tail", raises a concern about the possible loss of wanted spatial information in the final metallized metasurface. The existence of the loop deforms the shape of the square holes in the fishnet lattice. This might have an effect on the optical measurements and therefore the properties of the metasurface. It remains to be seen if a shorter scaffold should be utilized in the design. Of course, this would mean that the whole origami structure needs to be redesigned from scratch. Another solution to this problem would be to use a base sequence specific enzyme to cut off the unused scaffold loop.

In conclusion, similar monolayers can be achieved on silicon than what have been produced on mica to enable the use of DALI for the straightforward metallization of the fishnet lattices. Also, the quality of the obtained lattices is already high enough to continue on to optimizing the next steps of DALI. To further optimize the fishnet lattice, the size of the polycrystal domains could be increased, *e.g.*, by introducing

specific nucleation spots out of which the lattice domains can only start growing from. This would prevent the assembly of many small lattices all over the chip that quickly grow together in different orientations, preventing the formation of a larger, single lattice.

References

[1] G. Singh, Rajni, and A. Marwaha. "A Review of Metamaterials and its Applications". In: *International Journal of Engineering Trends and Technology* 19 (2015), pp. 305–310. DOI: 10.14445/22315381/IJETT-V19P254.

[2] D. R. Smith, J. B. Pendryand, and M. C. K. Wiltshire. "Metamaterials and Negative Refractive Index". In: *Science* 305 (2004), pp. 788–792. DOI: 10.1126/science.10967.

[3] V. M. Shalaev. "Optical negative-index metamaterials". In: *Nature Photonics* 1 (2007), pp. 41–48. DOI: 10.1038/nphoton.2006.49.

[4] J. Parikka *et al.* "Constructing Large 2D Lattices Out of DNA-Tiles". In: *Molecules* 26.6 (2021), p. 1502. DOI: 10.3390/molecules26061502.

[5] Y. Xin *et al.* "Self-assembly of highly ordered DNA origami lattices at solid-liquid interfaces by controlling cation binding and exchange". In: *Nano Research* 13 (2020), pp. 3142–3150. DOI: 10.1007/s12274-020-2985-4.

[6] A. A. Rafat *et al.* "Surface-Assisted Large-Scale Ordering of DNA Origami Tiles". In: *Angewandte Chemie* 53 (2014). DOI: 10.1002/anie.201403965.

[7] P. W. K. Rothemund. "Folding DNA to create nanoscale shapes and patterns". In: *Nature* 440 (2006), pp. 297–302. DOI: 10.1038/nature04586.

[8] B. Shen *et al.* "Plasmonic nanostructures through DNA-assisted lithography". In: *Science Advances* 4 (2018), eaap8978. DOI: 10.1126/sciadv.aap8978.

[9] W. Liu *et al.* "Crystalline Two-Dimensional DNA-Origami Arrays". In: *Angewandte Chemie* 50 (2011), pp. 264–267. DOI: 10.1002/anie.201005911.

[10] J. B. Reece *et al. Campbell Biology 10th edition.* Pearson, 2011. ISBN: 978-0-321-77565-8.

[11] L. A. Pray. "Discovery of DNA Structure and Function: Watson and Crick". In: *Nature Education* 1 (2008), p. 100.

[12] J. D. Watson and F. H. C. Crick. “The structure of DNA”. In: *Cold Spring Harbor Symposia on Quantitative Biology* 18 (1953), pp. 123–131. DOI: 10.1101/SQB.1953.018.01.020.

[13] K. Hoogstein. “The crystal and molecular structure of a hydrogen-bonded complex between 1-methylthymine and 9-methyladenine”. In: *Acta Crystallographica* 16 (1963), pp. 907–916. DOI: 10.1107/S0365110X63002437.

[14] E. N. Nikolova *et al.* “Transient Hoogsteen base pairs in canonical duplex DNA”. In: *Nature* 470 (2011), pp. 498–502. DOI: 10.1038/nature09775.

[15] Holtzclaw, Robinson, and Odom. *General Chemistry Ninth Edition*. D C Heath Co, 1991. ISBN: 978-0669244298.

[16] N. J. Tro. *Chemistry A Molecular Approach Third Edition*. Pearson, 2014. ISBN: 978-0321809247.

[17] D. W. Smith. “Ionic Hydration Enthalpies”. In: *Journal of Chemical Education* 54 (1977), pp. 540–542. DOI: 10.1021/ed054p540.

[18] G. Barone *et al.* “DNA-binding of nickel(II), copper(II) and zinc(II) complexes: Structure–affinity relationships”. In: *Coordination Chemistry Reviews* 257 (2013), pp. 2848–2862. DOI: 10.1016/j.ccr.2013.02.023.

[19] M. H. Shamsi and H.-B. Kraatz. “Interactions of Metal Ions with DNA and Some Applications”. In: *Journal of Inorganic and Organometallic Polymers and Materials* 23 (2013), pp. 4–23. DOI: 10.1007/s10904-012-9694-8.

[20] H.G.Hansma and D.E.Laney. “DNA binding to mica correlates with cationic radius: assay by atomic force microscopy”. In: *Biophysical Journal* 70 (1996), pp. 1933–1939. DOI: 10.1016/S0006-3495(96)79757-6.

[21] G. L. Eichhorn and Y. A. Shin. “Interaction of Metal Ions with Polynucleotides and Related Compounds. XII. The Relative Effect of Various Metal Ions on DNA Helicity”. In: *Journal of the American Chemical Society* 90 (1968), pp. 7323–7328. DOI: 10.1021/ja01028a024.

[22] C. A. Davey and T. J. Richmond. “DNA-dependent divalent cation binding in the nucleosome core particle”. In: *Proceedings of the National Academy of Sciences* 99 (2002), pp. 11169–74. DOI: 10.1073/pnas.172271399.

[23] S. M. Nilapwar *et al.* “Chapter four - Absorption Spectroscopy”. In: *Methods in Enzymology* 500 (2011), pp. 59–75. DOI: 10.1016/B978-0-12-385118-5.00004-9.

[24] K. L. Manchester. “Use of UV Methods for Measurement of Protein and Nucleic Acid Concentrations”. In: *Biotechniques* 20 (2018), pp. 968–970. DOI: 10.2144/96206bm05.

[25] D. F. Swineharf. “The Beer-Lambert Law”. In: *Journal of Chemical Education* 39 (1962), pp. 333–335. DOI: 10.1021/ed039p333.

[26] S. M. Douglas *et al.* “Self-assembly of DNA into nanoscale three-dimensional shapes”. In: *Nature* 459 (2009), pp. 414–418. DOI: 10.1038/nature08016.

[27] S. M. Douglas *et al.* “Rapid prototyping of 3D DNA-origami shapes with caDNAno”. In: *Nucleic Acids Research* 37 (2009), pp. 359–382. DOI: 10.1093/nar/gkp436.

[28] N. C.Seeman. “Nucleic acid junctions and lattices”. In: *Journal of Theoretical Biology* 99 (1982), pp. 237–247. DOI: 10.1016/0022-5193(82)90002-9.

[29] W. M. Shih, J. D. Quispe, and G. F. Joyce. “A 1.7-kilobase single-stranded DNA that folds into a nanoscale octahedron”. In: *Nature* 427 (2004), pp. 618–621. DOI: 10.1038/nature02307.

[30] P. Wang *et al.* “The beauty and utility of DNA origami”. In: *Chem* 2 (2017), pp. 359–382. DOI: 10.1016/j.chempr.2017.02.009.

[31] Y. Ke *et al.* “Scaffolded DNA Origami of a DNA Tetrahedron Molecular Container”. In: *Nano Letters* 9 (2009), pp. 2445–2447. DOI: 10.1021/nl901165f.

[32] E. S. Andersen *et al.* “Self-assembly of a nanoscale DNA box with a controllable lid”. In: *Nature* 459 (2009), pp. 73–76. DOI: 10.1038/nature07971.

[33] E. S. Andersen *et al.* “Semiautomated improvement of RNA alignments”. In: *RNA* 13 (2007), pp. 1850–1859.

[34] S. M. D. Henrik Dietz and W. M. Shih. “Folding DNA into Twisted and Curved Nanoscale Shapes”. In: *Science* 325 (2009), pp. 725–730. DOI: 10.1126/science.1174251.

[35] Y. Ke *et al.* “Three-Dimensional Structures Self-Assembled from DNA Bricks”. In: *Science* 338 (2012), pp. 1177–1183. DOI: 10.1126/science.1227268.

[36] D. Han *et al.* "DNA Gridiron Nanostructures Based on Four-Arm Junctions". In: *Science* 339 (2013), pp. 1412–1415. DOI: 10.1126/science.1232252.

[37] F. Zhang *et al.* "Complex wireframe DNA origami nanostructures with multi-arm junction vertices". In: *Nature Nanotechnology* 10 (2015), pp. 779–784. DOI: 10.1038/nnano.2015.162.

[38] W. Wang *et al.* "Complex wireframe DNA nanostructures from simple building blocks". In: *Nature Communications* 10 (2019), pp. 1–8. DOI: 10.1038/s41467-019-08647-7.

[39] V. Linko and M. A. Kostiainen. "Automated design of DNA origami". In: *Nature Biotechnology* 34 (2016), pp. 826–827. DOI: 10.1038/nbt.3647.

[40] H. Jun *et al.* "Automated sequence design of 2D wireframe DNA origami with honeycomb edges". In: *Nature Communications* 10 (2019), pp. 1–9. DOI: 10.1038/s41467-019-13457-y.

[41] H. Jun *et al.* "Automated Sequence Design of 3D Polyhedral Wireframe DNA Origami with Honeycomb Edges". In: *ACS Nano* 13 (2019), pp. 2083–2093. DOI: 10.1038/s41467-019-13457-y.

[42] H. Tadakuma, T. Masubuchi, and T. Ueda. "Chapter Five - RNA Study Using DNA Nanotechnology". In: *Progress in Molecular Biology and Translational Science* 139 (2016), pp. 121–163. DOI: 10.1016/bs.pmbts.2015.11.004.

[43] Z. Li *et al.* "Molecular Behavior of DNA Origami in Higher-Order Self-Assembly". In: *Journal of the American Chemical Society* 132 (2010), pp. 13545–13552. DOI: 10.1021/ja106292x.

[44] D. S. Ramakrishnan *et al.* "Real-Time Observation of Superstructure-Dependent DNA Origami Digestion by DNase I Using High-Speed Atomic Force Microscopy". In: *Chembiochem* 20 (2019), pp. 2818–2823. DOI: 10.1002/cbic.201900369.

[45] F. Kilchherr *et al.* "Single-molecule dissection of stacking forces in DNA". In: *Science* 353 (2016), aaf5508. DOI: 10.1126/science.aaf5508.

[46] R. Dietrich. "Mica". In: *Encyclopedia Britannica* (2021).

[47] K. A. Krylova *et al.* "Linking tracks in mica crystals with phase transitions in a bistable lattice". In: *The European Physical Journal B* 93 (2020). DOI: 10.1140/epjb/e2020-100565-0.

[48] D. Gray, A. McCaughan, and B. Mookerji. “Crystal Structure of Graphite, Graphene and Silicon”. In: *Physics for Solid State Applications* 6 (2009).

[49] T. Sinno *et al.* “Defect engineering of Czochralski single-crystal silicon”. In: *Materials Science and Engineering* 28 (2000), pp. 149–198. DOI: 10.1021/acsanm.0c02849.

[50] K. F. Jensen. “Silicon-Based Microchemical Systems: Characteristics and Applications”. In: *MRS Bulletin* 31 (2006), pp. 101–107. DOI: 10.1557/mrs2006.23.

[51] A. Müller *et al.* “Silicon for photovoltaic applications”. In: *Materials Science and Engineering: B* 134 (2006), pp. 257–262. DOI: 10.1016/j.mseb.2006.06.054.

[52] T. K. Gaylord and M. G. Moharamo. “Analysis and applications of optical diffraction by gratings”. In: *Proceedings of the IEEE* 73 (1985), pp. 894–937. DOI: 10.1109/PROC.1985.13220.

[53] L. Liu *et al.* “Regulating DNA Self-assembly by DNA–Surface Interactions”. In: *ChemBioChem* 18 (2017), pp. 2404–2407. DOI: 10.1002/cbic.201700545.

[54] C. Kielar *et al.* “Dynamics of DNA Origami Lattice Formation at Solid-Liquid Interfaces”. In: *ACS Applied Materials Interfaces* 10 (2018), pp. 44844–44853. DOI: 10.1021/acsami.8b16047.

[55] C. Lin *et al.* “Multivalent Ion-Mediated Attraction between Like-Charged Colloidal Particles: Nonmonotonic Dependence on the Particle Charge”. In: *ACS Omega* 6 (2021), pp. 9876–9886. DOI: 10.1021/acsomega.1c00613.

[56] K. Besteman, V. E. K., and S. Lemay. “Charge inversion accompanies DNA condensation by multivalent ions”. In: *Nature Physics* 3 (2007), pp. 641–644. DOI: 10.1038/nphys697.

[57] V. A. Bloomfield. “DNA condensation by multivalent cations”. In: *Biopolymers* 44 (1997), pp. 269–82. DOI: 10.1002/(SICI)1097-0282(1997)44:3<269::AID-BIP6>3.0.CO;2-T.

[58] L. Opherden *et al.* “Paramagnetic Decoration of DNA Origami Nanostructures by Eu3+ Coordination”. In: *Langmuir* 30 (2014), pp. 8152–8159. DOI: 10.1021/la501112a.

[59] A. X. Kohll *et al.* "Stabilizing synthetic DNA for long-term data storage with earth alkaline salts". In: *Chemical Communications* 56 (2020), pp. 3613–3616. DOI: 10.1039/d0cc00222d.

[60] M. A. Hartney, D. W. Hess, and D. S. Soane. "Oxygen plasma etching for resist stripping and multilayer lithography". In: *Journal of Vacuum Science Technology B: Microelectronics Processing and Phenomena* 7 (1989). DOI: 10.1116/1.584440.

[61] K. Tapio *et al.* "A DNA–nanoparticle actuator enabling optical monitoring of nanoscale movements induced by an electric field". In: *Nanoscale* 10 (2018), pp. 19297–19309. DOI: 10.1039/C8NR05535A.

[62] T. A. Mgheer and F. H. Abdulrazzak. "Oxidation of multi-walled carbon nanotubes in acidic and basic Piranha mixture". In: *Frontiers in Nanosciense and Nanotechnology* 2 (2016), pp. 155–158. DOI: 10.15761/FNN.1000127.

[63] P. Piskunen *et al.* "Biotemplated Lithography of Inorganic Nanostructures (BLIN) for Versatile Patterning of Functional Materials". In: *ACS Applied Nano Materials* 4 (2021), pp. 529–538. DOI: 10.1021/acsanm.0c02849.

[64] S. P. Surwade *et al.* "Nanoscale Growth and Patterning of Inorganic Oxides Using DNA Nanostructure Templates". In: *Journal of the American Chemical Society* 135 (2013), pp. 6778–6781. DOI: 10.1021/ja401785h.

[65] J. su Yoo, G. Yu, and J. Yi. "Large-area multicrystalline silicon solar cell fabrication using reactive ion etching (RIE)". In: *Solar Energy Materials and Solar Cells* 95 (2011), pp. 2–6. DOI: 10.1016/j.solmat.2010.03.029.

[66] R. d'Agostino and D. L. Flamm. "Plasma etching of Si and SiO2 in SF6–O2 mixtures". In: *Journal of Applied Physics* 52 (1981), pp. 162–167. DOI: 10.1063/1.328468.

[67] R. D. Mansano *et al.* "Anisotropic inductively coupled plasma etching of silicon with pure SF6". In: *Thin Solid Films* 343-344 (1999), pp. 378–380. DOI: 10.1016/S0040-6090(98)01689-7.

[68] K. Racka-Szmidt *et al.* "A Review: Inductively Coupled Plasma Reactive Ion Etching of Silicon Carbide". In: *Materials* 15 (2022). DOI: 10.3390/ma15010123.

[69] S. Xiao *et al.* "Yellow-light negative-index metamaterials". In: *Optics Letters* 34 (2009), pp. 3478–3480. DOI: 10.1364/OL.34.003478.

[70] Z. H. Jiang *et al.* "Tailoring Dispersion for Broadband Low-loss Optical Metamaterials Using Deep-subwavelength Inclusions". In: *Scientific reports* 3 (2013), pp. 1–9. DOI: 10.1038/srep01571.

[71] B. D. Huey. "AFM and Acoustics: Fast, Quantitative Nanomechanical Mapping". In: *The Annual Review of Materials Research* 37 (2007), pp. 351–385. DOI: 10.1016/j.ultramic.2005.12.006.

[72] M. Kopycinska-Müller, R. H. Geiss, and D. C. Hurley. "Contact mechanics and tip shape in AFM-based nanomechanical measurements". In: *Ultramicroscopy* 106 (2006), pp. 466–474. DOI: 10.1016/j.ultramic.2005.12.006.

[73] G. Binnig and C. F. Quate. "Atomic Force Microscope". In: *Physical Review Letters* 56 (1986), pp. 930–933. DOI: 10.1103/PhysRevLett.56.930.

[74] P. Trtik, J. Kaufmann, and U. Volz. "On the use of peak-force tapping atomic force microscopy for quantification of the local elastic modulus in hardened cement paste". In: *Cement and Concrete Research* 42 (2012), pp. 215–221. DOI: 10.1016/j.cemconres.2011.08.009.

[75] W. Melitz *et al.* "Kelvin probe force microscopy and its application". In: *Surface Science Reports* 66 (2011), pp. 1–27. DOI: 10.1016/j.surfrep.2010.10.001.

[76] T. Sulchek *et al.* "High-speed atomic force microscopy in liquid". In: *Review of Scientific Instruments* 71 (2000). DOI: 10.1063/1.1150586.

[77] A. Behle and A. Pawlowski. "Recipe for 50x TAE buffer". In: *Protocols.io* (2018). DOI: 10.17504/protocols.io.gtvbwn6.

[78] M. J. Ryssy *et al.* "Light-Responsive Dynamic DNA-Origami-Based Plasmonic Assemblies". In: *Angewandte Chemie* 60 (2011), pp. 5859–5863. DOI: 10.1002/anie.202014963.

[79] B. Shen *et al.* "Custom-shaped metal nanostructures based on DNA origami silhouettes". In: *Nanoscale* 7 (2015), pp. 11267–11272. DOI: 10.1039/C5NR02300A.

[80] K. F. Wagenbauer *et al.* "How we make DNA origami". In: *ChemBioChem* 18 (2017), pp. 1873–1885. DOI: 10.1002/cbic.201700377.

[81] S. Woo and P. W. Rothemund. “Self-assembly of two-dimensional DNA origami lattices using cation-controlled surface diffusion”. In: *Nature communications* 5 (2014), p. 4889. DOI: 10.1038/ncomms5889.

[82] H. Kim *et al.* “Stability of DNA Origami Nanostructure under Diverse Chemical Environments”. In: *Chemistry of Materials* 26 (2014), pp. 5265–5273. DOI: 10.1021/cm5019663.

[83] M. A. Pillers and M. Lieberman. “Thermal stability of DNA origami on mica”. In: *Journal of Vacuum Science Technology B* 32 (2014), p. 040602. DOI: 10.1116/1.4879417.

[84] B. M. Ward. “Thermodynamics and kinetics of DNA origami cross-tile array formation”. Dissertation. Boise State University, 2017.

[85] S. Ramakrishnan *et al.* “Structural stability of DNA origami nanostructures in the presence of chaotropic agents”. In: *Nanoscale* 8 (2016), pp. 10398–10405. DOI: 10.1039/c6nr00835f.

[86] S. Xiao *et al.* “Yellow-light negative-index metamaterials”. In: *Optics Letters* 34 (2009), pp. 3478–3480.

[87] Z. H. Jiang *et al.* “Tailoring Dispersion for Broadband Low-loss Optical Metamaterials Using Deep-subwavelength Inclusions”. In: *Scientific Reports* 3 (2013), p. 1571. DOI: 10.1038/srep01571.

A List of chemicals

Table 3. Table of used chemicals.

Chemical	**Formula**	**Company**	**Purity**
Magnesium dichloride hexahydrate	$MgCl_2$ ($\cdot$ 6 H_2O)	Merck, Assay (complexometric)	99.0-101.0 %
Nickel dichloride hexahydrate	$NiCl_2$ ($\cdot$ 6 H_2O)	Merck, Assay (complexometric)	$\geq$ 96.0%
Calcium dichloride dihydrate	$CaCl_2$ ($\cdot$ 2 H_2O)	Fluka	$\geq$ 99%
Sodium chloride	NaCl	Merck	$\geq$ 99.5%
Potassium chloride	KCl	Emsure, Merck	$\geq$ 99.5%
Lithium chloride	LiCl	Merck	$\geq$ 99%
Disodium EDTA dihydrate	$C_{10}H_{14}N_2Na_2O_8$ ($\cdot$ 2 H_2O)	Merck, Assay (complexometric)	99.0-101.0 %
Tris	$C_4H_{11}NO_3$	Sigma-Aldrich (Titration)	$\geq$ 99.9%
Acetic Acid	CH_3COOH	Sigma-Aldrich	$\geq$ 99.8%
Sodium hydroxide	NaOH	Riedel-de-Haën, Assay	$\geq$ 99%
Hydrogen peroxide 30%	H_2O_2	VWR Chemicals	29.0-31.0 %
Tetraethyl Orthosilicate (TEOS)	$Si(OC_2H_5)_4$	Sigma-Aldrich	$\geq$ 99.0%
Ammonium hydroxide 25%	NH_4OH	J.T.Baker	28.0-30.0 %
2-propanol (IPA)	$CH_3CHOHCH_3$	Sigma-Aldrich	$\geq$ 98%
Acetone	$(CH_3)_2CO$	Sigma-Aldrich	$\geq$ 99.9%

B Origami mixture calculations

Origami folding protocol

Table 4. Initial concentrations.

scaffold (M13mp18)	oligo staples	edge staples
$c_{\text{scaffold}} = 100$ nM	$c^0_{\text{oligo}} = 100\ \mu$M	$c^0_{\text{edge}} = 100\ \mu$M

Initial concentrations of stock solutions are listed in Table 4. In total there are 186 oligo staples and 24 edge staples. Final concentration ratio has to be

scaffold	:	oligo	:	edge
1	:	1.4	:	5.6

If 1 μL of each 186 staples (100 μM) is taken, we will have 186 μL of solution (oligo mix) which has concentration of

$$\begin{aligned} c_{\text{oligo}} &= \frac{1\ \mu\text{L} \cdot 100\ \mu\text{M}}{186\ \mu\text{M}} \\ &= 0.5376\ \mu\text{M} \\ &= \underline{537.6\ \text{nM}} \end{aligned}$$

Same holds for 24 edge staples (100 μM) where we will have 24 μL of solution (edge mix) and we get the concentration for edge staples to be

$$\begin{aligned} c_{\text{edge}} &= \frac{1\ \mu\text{L} \cdot 100\ \mu\text{M}}{24\ \mu\text{M}} \\ &= 4.16667\ \mu\text{M} \\ &= \underline{4166.7\ \text{nM}} \end{aligned}$$

When these two are combined their concentrations and volumes will change. We know that final concentration of the edges must be $4\times$ of oligo concentration *i.e.* $c'_{\text{edge}} = 4 \cdot c'_{\text{oligo}}$. Using this ratio we can say for oligos

$$\begin{aligned} c_{\text{oligo}} V_{\text{oligo}} &= c'_{\text{oligo}} \cdot (V_{\text{edge}} + V_{\text{oligo}}) \\ &= c'_{\text{oligo}} \cdot (V_{\text{edge}} + V_{\text{oligo}}) \end{aligned}$$

and for edges we can say

$$\begin{aligned} c_{\text{edge}} V_{\text{edge}} &= c'_{\text{edge}} \cdot (V_{\text{edge}} + V_{\text{oligo}}) \\ &= 4 \cdot c'_{\text{oligo}} \cdot (V_{\text{edge}} + V_{\text{oligo}}) \end{aligned}$$

where c'_{oligo} and c'_{edge} are concentrations when oligo and edge staples are mixed which need to be determined. If we divide the obtained results we get

$$\begin{aligned} c_{\text{edge}} V_{\text{edge}} &= 4c'_{\text{oligo}} \cdot (V_{\text{edge}} + V_{\text{oligo}}) \\ c_{\text{oligo}} V_{\text{oligo}} &= c'_{\text{oligo}} \cdot (V_{\text{edge}} + V_{\text{oligo}}) \\ \hline \frac{c_{\text{edge}} V_{\text{edge}}}{c_{\text{oligo}} V_{\text{oligo}}} &= 4. \end{aligned}$$

From here we can calculate the ratio between volumes we need

$$\begin{aligned} \frac{c_{\text{edge}} V_{\text{edge}}}{c_{\text{oligo}} V_{\text{oligo}}} &= 4 \\ V_{\text{oligo}} &= \frac{c_{\text{edge}} V_{\text{edge}}}{4 c_{\text{oligo}}} \\ &= \frac{4166.7 \text{ nM} \cdot V_{\text{edge}}}{4 \cdot 537.6 \text{ nM}} \\ &= \underline{1.93764 \cdot V_{\text{edge}}}. \end{aligned}$$

So now we know that we need 1.93764 times the volume of oligos compared to

edges. If we take for example 20 μL of edge mix, we need

$$\begin{aligned} & 20\ \mu\text{L} \cdot 1.938 \\ &= \underline{38.76\ \mu\text{L}} \end{aligned}$$

of oligo mix. Now we can calculate the final concentration of oligo mix

$$\begin{aligned} c_{\text{oligo}} V_{\text{oligo}} &= c'_{\text{oligo}} \cdot (V_{\text{edge}} + V_{\text{oligo}}) \\ c'_{\text{oligo}} &= \frac{c_{\text{oligo}} V_{\text{oligo}}}{(V_{\text{edge}} + V_{\text{oligo}})} \\ &= \frac{537.6\ \text{nM} \cdot 38.76\ \mu\text{L}}{(20\ \mu\text{L} + 38.76\ \mu\text{L})} \\ &= \underline{354.618\ \text{nM}} \end{aligned}$$

and also for edge mix

$$\begin{aligned} c_{\text{edge}} V_{\text{edge}} &= c'_{\text{edge}} \cdot (V_{\text{edge}} + V_{\text{oligo}}) \\ c'_{\text{edge}} &= \frac{c_{\text{edge}} V_{\text{edge}}}{(V_{\text{edge}} + V_{\text{oligo}})} \\ &= \frac{4166{,}7\ \text{nM} \cdot 20\ \mu\text{L}}{(20\ \mu\text{L} + 38.76\ \mu\text{L})} \\ &= \underline{1418.21\ \text{nM}} \end{aligned}$$

Now we can calculate the amount of scaffold we need. This can be done using either oligo or edge, the result should be same. Now the volume for both oligo and edge is their combined volume ($V'_{\text{oligo}} = V'_{\text{edge}} = 58.76\ \mu\text{L}$). From the ratios we can say that final concentrations are $c''_{\text{oligo}} = 1.4 \cdot c'_{\text{scaffold}}$ and $c''_{\text{edge}} = 5.6 \cdot c'_{\text{scaffold}}$. Using oligo values we get

$$\begin{aligned} c'_{\text{oligo}} V'_{\text{oligo}} &= c''_{\text{oligo}} \cdot (V_{\text{edge}} + V_{\text{oligo}} + V_{\text{scaffold}}) \\ &= 1{,}4 \cdot c'_{\text{scaffold}} \cdot (V_{\text{edge}} + V_{\text{oligo}} + V_{\text{scaffold}}) \end{aligned}$$

where c''_{oligo} is final concentration of oligo mix. For scaffold we can say

$$\begin{aligned} c_{\text{scaffold}} V_{\text{scaffold}} &= c'_{\text{scaffold}} \cdot (V_{\text{edge}} + V_{\text{oligo}} + V_{\text{scaffold}}) \\ &= c'_{\text{scaffold}} \cdot (V_{\text{edge}} + V_{\text{oligo}} + V_{\text{scaffold}}). \end{aligned}$$

If we divide these results we get

$$\begin{aligned} c'_{\text{oligo}} V'_{\text{oligo}} &= 1{,}4 \cdot c'_{\text{scaffold}} \cdot (V_{\text{edge}} + V_{\text{oligo}} + V_{\text{scaffold}}) \\ c_{\text{scaffold}} V_{\text{scaffold}} &= c'_{\text{scaffold}} \cdot (V_{\text{edge}} + V_{\text{oligo}} + V_{\text{scaffold}}) \end{aligned}$$

$$\begin{aligned} \frac{c'_{\text{oligo}} V'_{\text{oligo}}}{c_{\text{scaffold}} V_{\text{scaffold}}} &= 1{,}4 \\ V_{\text{scaffold}} &= \frac{c'_{\text{oligo}} V'_{\text{oligo}}}{1.4 \cdot c_{\text{scaffold}}} \\ &= \frac{354.618 \text{ nM} \cdot 58.76 \ \mu\text{L}}{1.4 \cdot 100 \text{ nM}} \\ &= \underline{148.838 \ \mu\text{L}} \end{aligned}$$

In a same way using edges we would get

$$\begin{aligned} \frac{c'_{\text{edge}} V'_{\text{edge}}}{c_{\text{scaffold}} V_{\text{scaffold}}} &= 5.6 \\ V_{\text{scaffold}} &= \frac{c'_{\text{edge}} V'_{\text{edge}}}{5.6 \cdot c_{\text{scaffold}}} \\ &= \frac{1418.21 \text{ nM} \cdot 58.76 \ \mu\text{L}}{1.4 \cdot 100 \text{ nM}} \\ &= \underline{148.811 \ \mu\text{L}} \end{aligned}$$

Slight difference but we round it to 148.8 μL. So in order to maintain the wanted ratio we need 20 μL of edge mix, 38.8 μL of oligo mix and 148.8 μL of scaffold. Therefore total volume is 207.6 μL.

Before folding we need to have 1×TAE and 12.5 mM Mg conditions in the mixture. These can be achieved by diluting scaffold/staples mix using 2.5x folding buffer (TAE) with 31.25 mM of $MgCl_2$. If we use the whole amount of sample ($V_{\text{tot}} = 207.6$

μL) and want to dilute the buffer from 2.5x to 1× we need to calculate the volume of buffer

$$
\begin{aligned}
c_{\text{buffer}} V_{\text{buffer}} &= c'_{\text{buffer}} \cdot (V_{\text{buffer}} + V_{\text{tot}}) \\
c_{\text{buffer}} V_{\text{buffer}} &= c'_{\text{buffer}} V_{\text{buffer}} + c'_{\text{buffer}} V_{\text{tot}} \\
&\dots \\
V_{\text{buffer}} &= \frac{c'_{\text{buffer}} \cdot V_{\text{tot}}}{c_{\text{buffer}} - c'_{\text{buffer}}} \\
&= \frac{1 \times \cdot 207.6\ \mu\text{L}}{2.5 \times -1\times} \\
&= \underline{138.4\ \mu\text{L}}
\end{aligned}
$$

So we need 138.4 uL of 2.5x buffer to 207.6 uL of DNA mix (total 346 uL). Then this mixture is in 1× TAE with 12.5 mM Mg.

Finally, we need to make sure that scaffold concentration in the end is 20 nM. This was the main condition for the fold and will always remain the limiting factor. To get this concentration for scaffold need to calculate the final volume where concentration will be 20 nM.

$$
\begin{aligned}
c_{\text{scaffold, initial}} \cdot V_{\text{scaffold}} &= c_{\text{scaffold, final}} \cdot V_{1\times} \\
V_{1\times} &= \frac{c_{\text{scaffold, initial}} \cdot V_{\text{scaffold}}}{c_{\text{scaffold, final}}} \\
&= \frac{100\ \text{nM} \cdot 148.8\ \mu\text{L}}{20\ \text{nM}} \\
&= \underline{744\ \mu\text{L}}
\end{aligned}
$$

So, the final volume has to be 744 μL which means that we need to add

$$744\mu\text{L} - 346\mu\text{L} = \underline{398\mu\text{L}}$$

of 1× TAE with 12.5 mM Mg. 1× TAE needs to have 12.5 mM Mg to keep the magnesium level set. This protocol gives us final volume of **744 μL** of folded DNA. This amount could be divided to 5 - 8 PCR-tubes for thermal annealing.

Example folding (7.6.2021)

At 7.6. we folded new batch of origami according to previous calculations. Total volume was chosen to be 1200 μL and final concentration of scaffold to be 20 nM. Initially calculated volumes were 20 μL edge + 38.8 μL oligo + 148.8 μL scaffold + 138.4 μL 2.5x folding buffer with 31.25 mM Mg^{2+} + 397.9 μL 1× folding buffer with 12.5 mM Mg^{2+} = 743.9 μL.

NOTE! Easy way to always determine the amounts of different solutions is to multiply every value with coefficient (Total sample volume/total amount that is calculated (743.9 μL in this case)).

Using this coefficient (1200/744) we calculated amounts of solutions needed and they are listed in table 5.

Table 5. Final volumes according to ratios.

edge	32.3 μL
oligo	62.6 μL
scaffold	240 μL
2.5×TAE (31.25 mM Mg^{2+})	223.2 μL
1×TAE (12.5 mM Mg^{2+})	641.8 μL
total volume	1199.8 μL
scaffold concentration	20 nM

NOTE! These volumes can be **round up** (*e.g.* for edge: 32.3 μL → 32.4 μL) for easier and reasonable pipetting.

C Recipe for origami folding mixture

NOTE! Easy way to always determine the amounts of different solutions is to multiply every value with coefficient (Total sample volume/total amount that is calculated (743.9 µL in this case)).

!!

FOR ANY GIVEN VOLUME

Final volume: 1200

Component:	**Volume (µL):** (Initial)		**Volume (µL):** (Coefficient 400/744)	**Volume (µL):** (Coefficient 1/744)	**Volume (µL):** (Coefficient X/744)
Edge staples (**4166.7 nM**)	20		10,8	0,027	32,3
Regular oligo staples (**537.6 nM**)	38,8		20,9	0,052	62,6
Scaffold (**100 nM**)	148,8		80,0	0,200	240,0
2.5x TAE (**31.25 mM Mg2+**)	138,4		74,4	0,186	223,2
1xTAE (**12.5 mM Mg2+**)	397,9		213,9	0,535	641,8
Total volume (µL):	743,9		399,9	1,000	1199,8
Final scaffold concentration (nM):	20,0		20,0	20,0	20,0

Scaffold conc. fixed to 20 nM with 1x TAE!

D Folding procedure for PCR

Thermal annealing temperatures and times for origami folding (Aalto's procedure):

Temperature °C	Time, min for each degree
80	15
79,78,77,76,75,74,73,72,71	1
70,69,68	5
67,66,65,64,63	10
62	15
61	20
60	30
59,58,57,56,55,54,53,52,51,50,49,48,47,46,45,44,43,42,41,40,39,38	60
37,36	45
35	30
34	20
33,32	10
31,30,29,28,27,26,25	5
24,23,22,21	2
20	Hold
Total	1677 min

Thermal annealing temperatures and times for origami folding (our variation):

Temperature °C	Time, min for each degree
80	15
79,78,77,76,75,74,73,72,71	1
70,69,68	5
67,66,65,64,63	10
62	10
61	15
60	25
59,58,57,56,55,54,53,52,51,50,49,48,47,46,45,44,43,42,41,40,39,38	25
37,36	30
35	25
34	20
33,32	10
31,30,29,28,27,26,25	5
24,23,22,21	2
20	Hold
Total	857 min ~14.3 h

Thermal annealing temperatures and times for origami folding (our variation v2):

Temperature °C	Time, min for each degree
80	15
79,78,77,76,75,74,73,72,71	1
70,69,68	5
67,66,65,64,63	10
62	10
61	15
60	25
59,58,57,56,55,54,53,52,51,50,49,48,47,46,45,44,43,42,41,40,39,38	35
37,36	30
35	25
34	20
33,32	10
31,30,29,28,27,26,25	5
24,23,22,21	2
20	Hold
Total	1077 min ~17.95 h

E Scaffold loop base sequence

5' GTTGCAGGCGGTGTTAATACTGACCGCCTCACCTCTGTT
TTATCTTCTGCTGGTGGTTCGTTCGGTATTTTTAATGGCGA
TGTTTTAGGGCTATCAGTTCGCGCATTAAAGACTAATAGCC
ATTCAAAAATATTGTCTGTGCCACGTATTCTTACGCTTTCA
GGTCAGAAGGGTTCTATCTCTGTTGGCCAGAATGTCCCTTT
TATTACTGGTCGTGTGACTGGTGAATCTGCCAATGTAAATA
ATCCATTTCAGACGATTGAGCGTCAAAATGTAGGTATTTCC
ATGAGCGTTTTTCCTGTTGCAATGGCTGGCGGTAATATTGT
TCTGGATATTACCAGCAAGGCCGATAGTTTGAGTTCTTCTA
CTCAGGCAAGTGATGTTATTACTAATCAAAGAAGTATTGCT
ACAACGGTTAATTTGCGTGATGGACAGACTCTTTTACTCGG
TGGCCTCACTGATTATAAAAACACTTCTCAAGATTCTGGCG
TACCGTTCCTGTCTAAAATCCCTTTAATCGGCCTCCTGTTT
AGCTCCCGCTCTGATTCCAACGAGGAAAGCACGTTATACGT
GCTCGTCAAAGCAACCATAGTACGCGCCCTGTAGCGGCGCA
TTAAGCGCGGCGGGTGTGGTGGTTACGCGCAGCGTGACCGC
TACACTTGCCAGCGCCCTAGCGCCCGCTCCTTTCGCTTTCT
TCCCTT 3'

Length: 701 bases

F Additional samples

F.1 Zoomed 100 mM - 300 mM magnesium samples

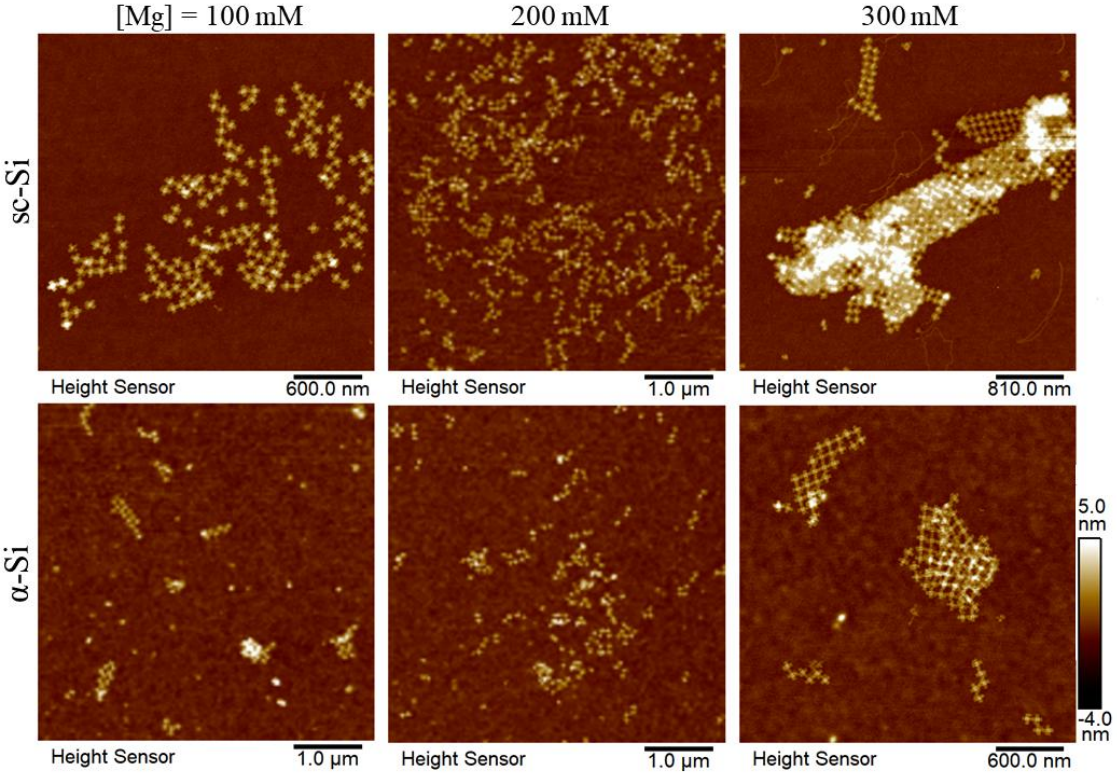

Figure 44. The effect of increasing the magnesium concentration for sc-Si (upper row) and α-Si (lower row) surfaces. Closer images of the best magnesium concentrations 100-300 mM are presented. Each AFM image represents a different sample with incubation time of 40 min. The TC-ST origami concentration for each sample is 10 nM.

F.2 Two-step incubation between magnesium and sodium

For one-step incubated samples all of the salts are added simultaneously and incubated for, *e.g.*, 40 min as was the case for the one-step reference sample. In two-step incubation the divalent cation (magnesium) is introduced first and incubated for a

certain time, in this case 10 min. The monovalent cation (sodium) is added afterwards and incubated further, which was here 30 min. As can be seen from figure 45, the later addition of sodium might have a bigger effect on the mobility of already landed lattices rather than the origami repulsion as some origami pairings are still observed. The origami seem to be more spread out on the surface for two-step incubation instead of in the shapes of drying patterns as observed for the reference. Although, this disappearance of pattern can also be caused by the later addition of liquid in the two-step process. No substantial improvement in lattice assembly can be obtained using two-step incubation between magnesium and sodium.

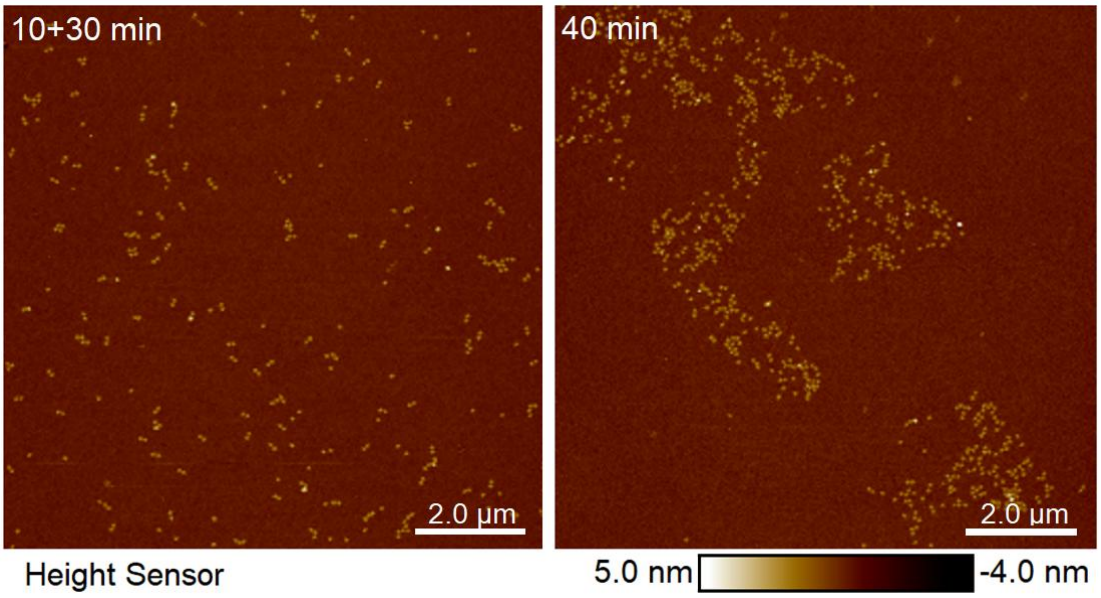

Figure 45. Comparison between a 10+30 min two-step and a 40 min one-step incubation. The two-step sample on the left was first incubated with 200 mM of magnesium for 10 min after which a concentration of 100 mM of sodium was set on the sample for 30 min. The reference sample on the right with the same salt concentrations was incubated as a single step for 40 min. The TC-ST origami concentration for each sample is 10 nM.

F.3 Sample with only nickel

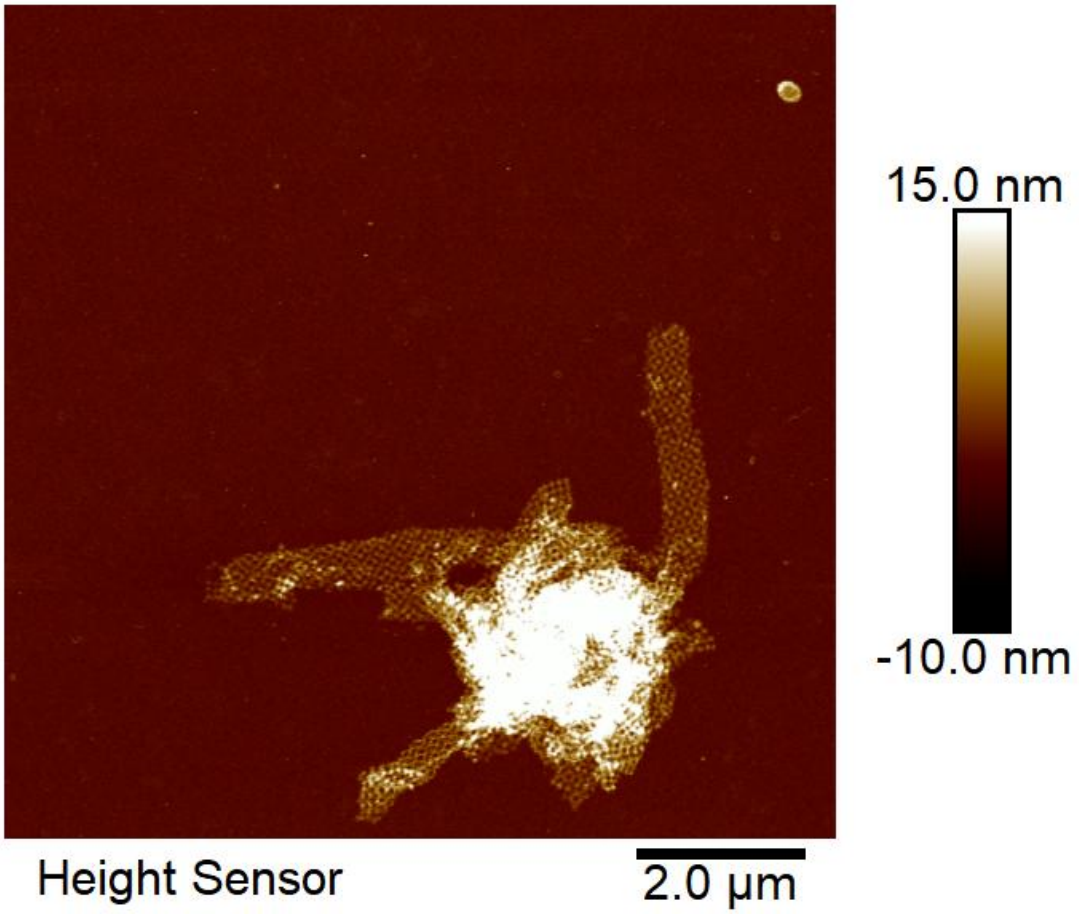

Figure 46. A sample with 1.5 mM nickel concentration and incubation time of 30 min on sc-Si surface. The TC-ST origami concentration is 10 nM.

F.4 Two-step Ni wash sample with elevated nickel concentration

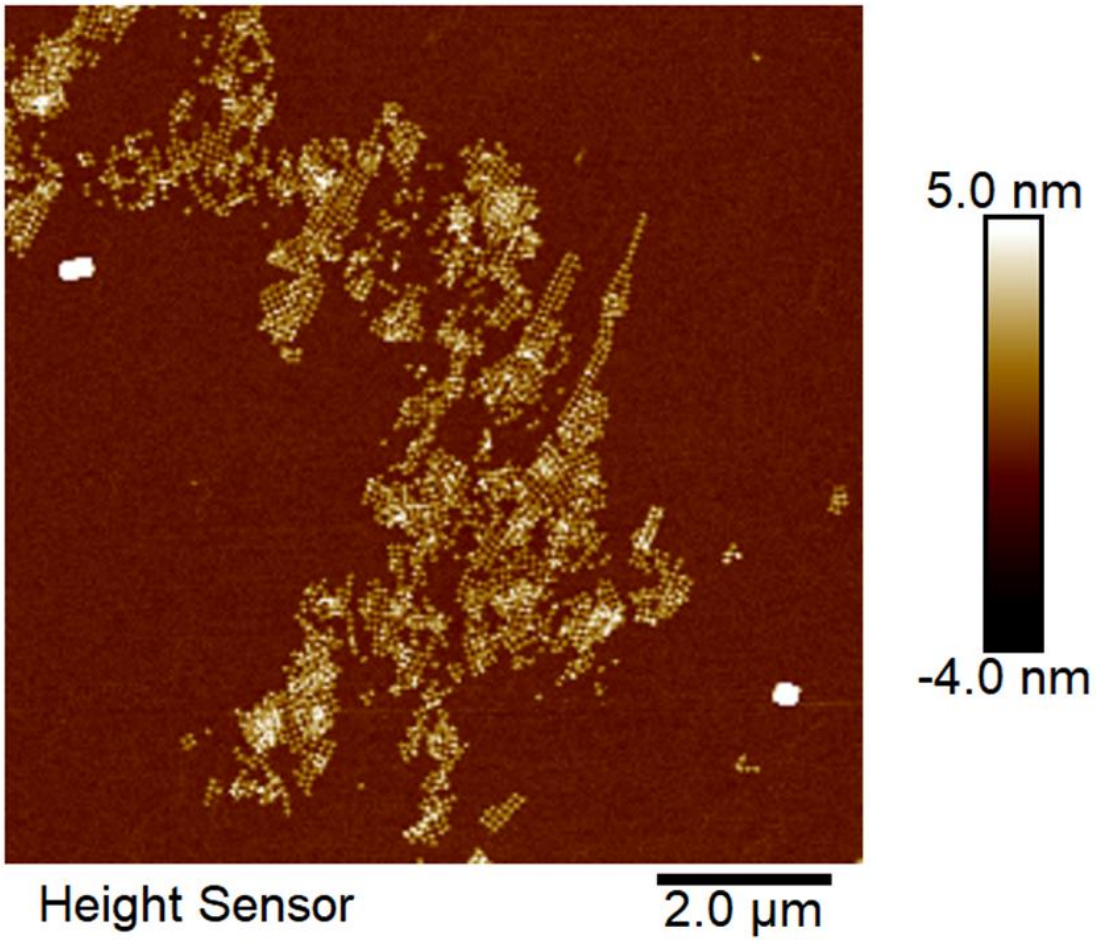

Figure 47. Two-step nickel wash sample with increased nickel concentration of 5 mM, magnesium concentration of 150 mM and sodium concentration of 100 mM with incubation time of 5+5 min on sc-Si surface. Magnesium and sodium were incubated on the sample for 5 min after which nickel was introduced on the sample for 5 min. The TC-ST origami concentration is 10 nM.

F.5 Lithium sample

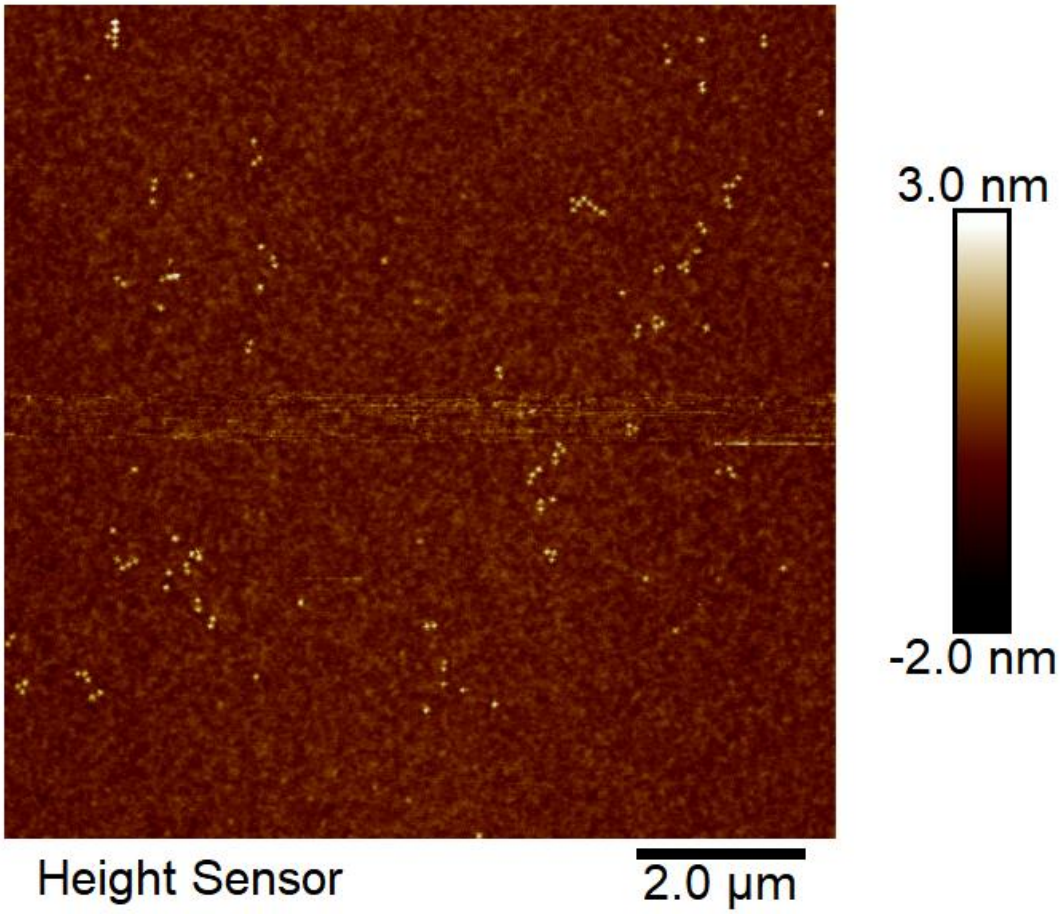

Figure 48. A sample with a 50 mM magnesium, 5 mM nickel, 50 mM lithium and a 10 nM TC-ST origami tile concentration on silicon with a 30 min incubation time.

F.6 Increasing magnesium for a fixed 100 mM sodium concentration

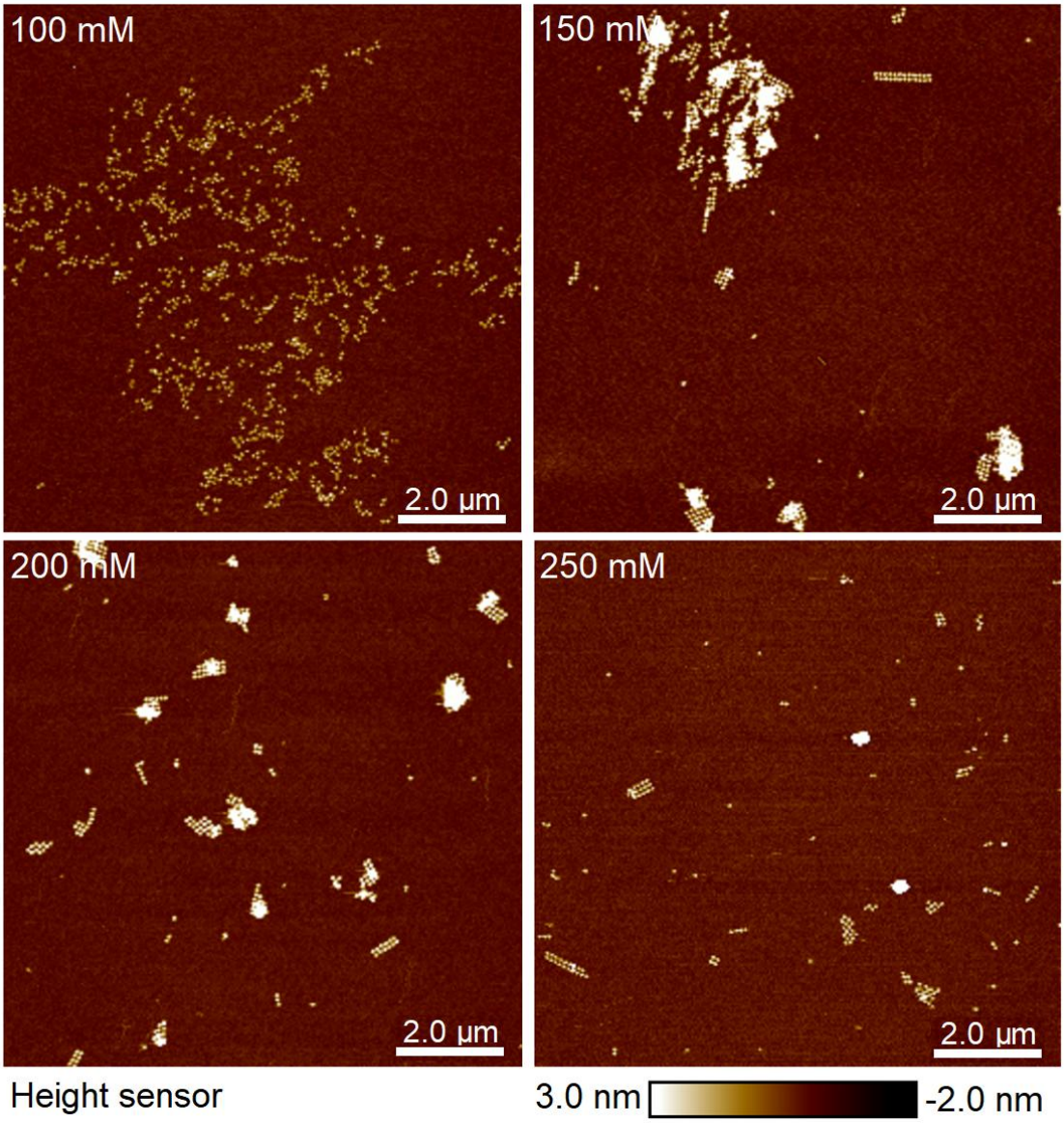

Figure 49. The effect of increasing the magnesium concentration for a fixed sodium concentration of 100 mM on sc-Si surface. Each AFM image represents an individual sample with incubation time of 15 min and magnesium concentration specified on the top left corner. The TC-ST origami concentration for each sample is 10 nM.

F.7 Additional samples from section 4.3.1

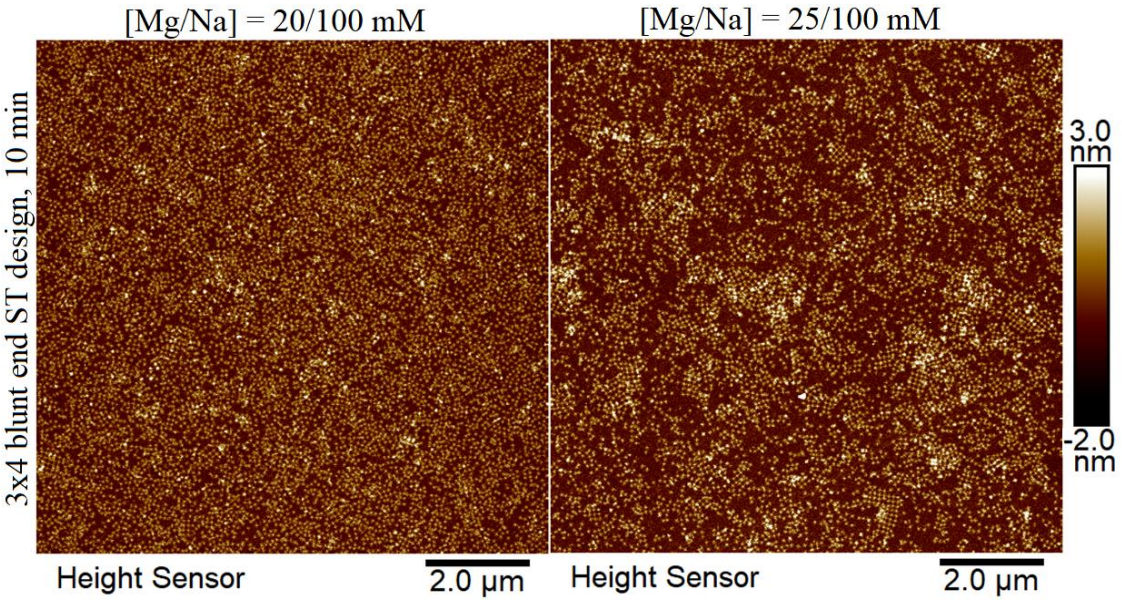

Figure 50. AFM imaging in air done for the 3×4 blunt-end TC-ST origami design in 20 mM and 25 mM magnesium, 100 mM sodium concentration with 10 min incubation time on sc-Si.

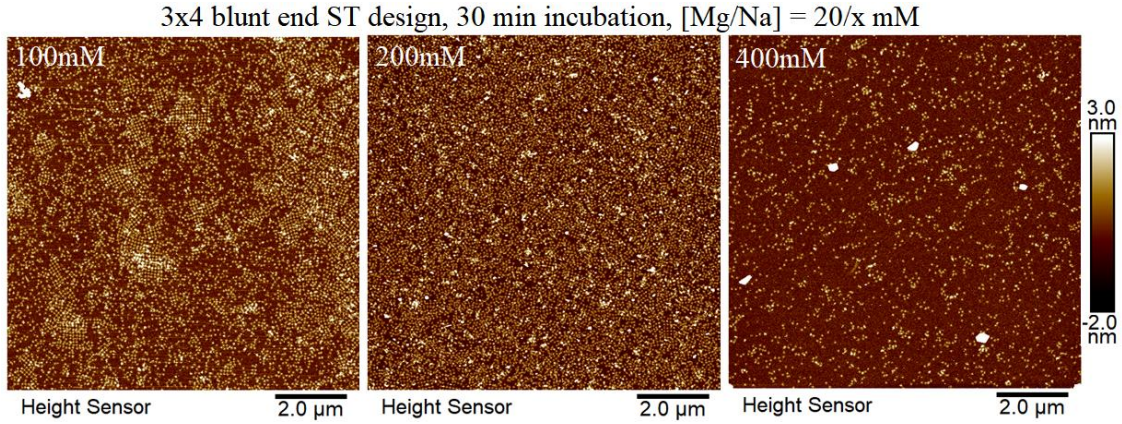

Figure 51. AFM imaging in air done for the 3×4 blunt-end TC-ST origami design in 20 mM magnesium concentration and 100 mM, 200 mM and 400 mM sodium concentration with 30 min incubation time on sc-Si.

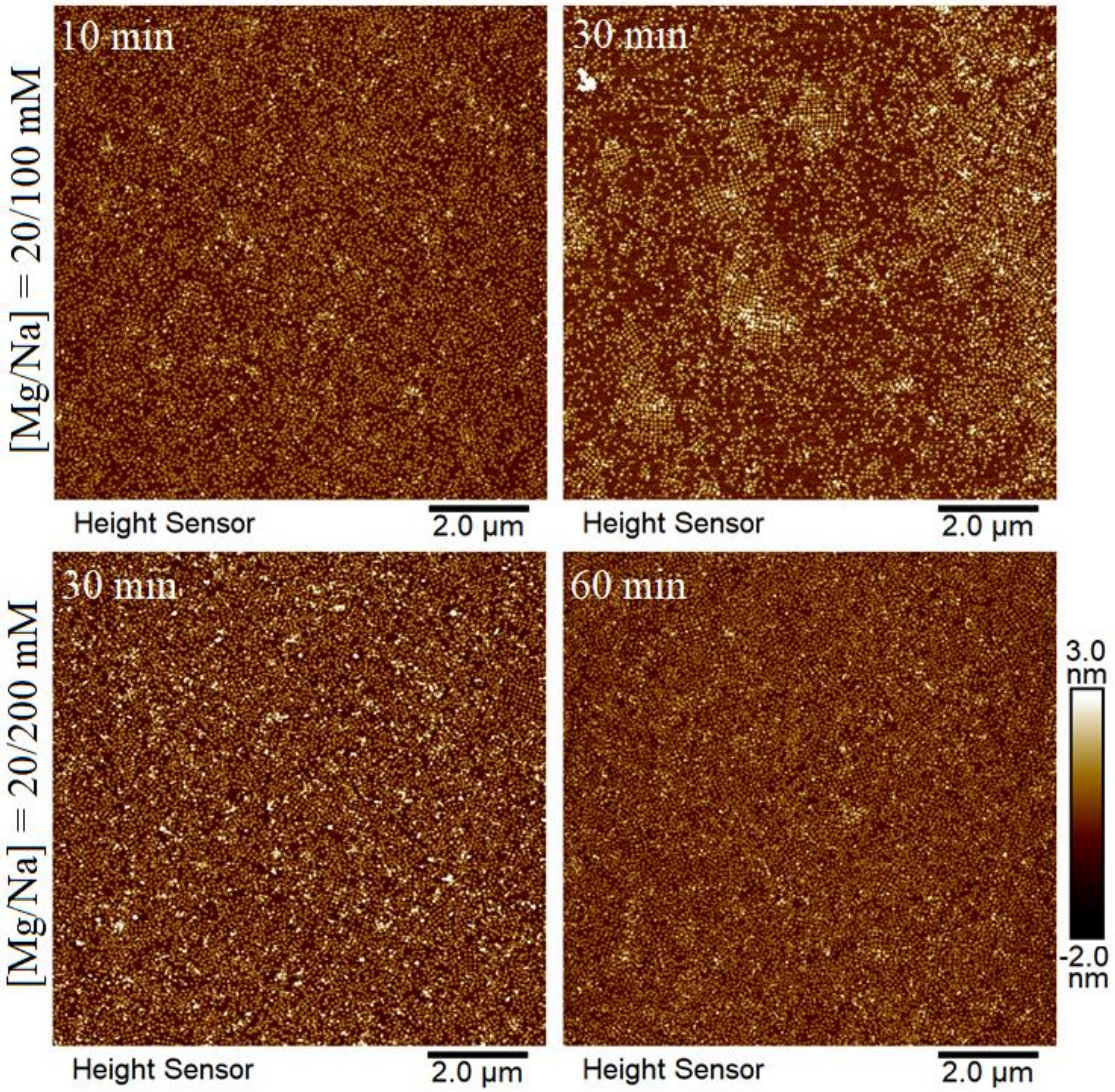

Figure 52. AFM imaging in air done for the 3×4 blunt-end TC-ST origami design in 20 mM magnesium concentration for 100 mM and 200 mM sodium concentrations with varying incubation times on sc-Si.

F.8 Effect of scanning frequencies on lattice assembly in liquid AFM imaging

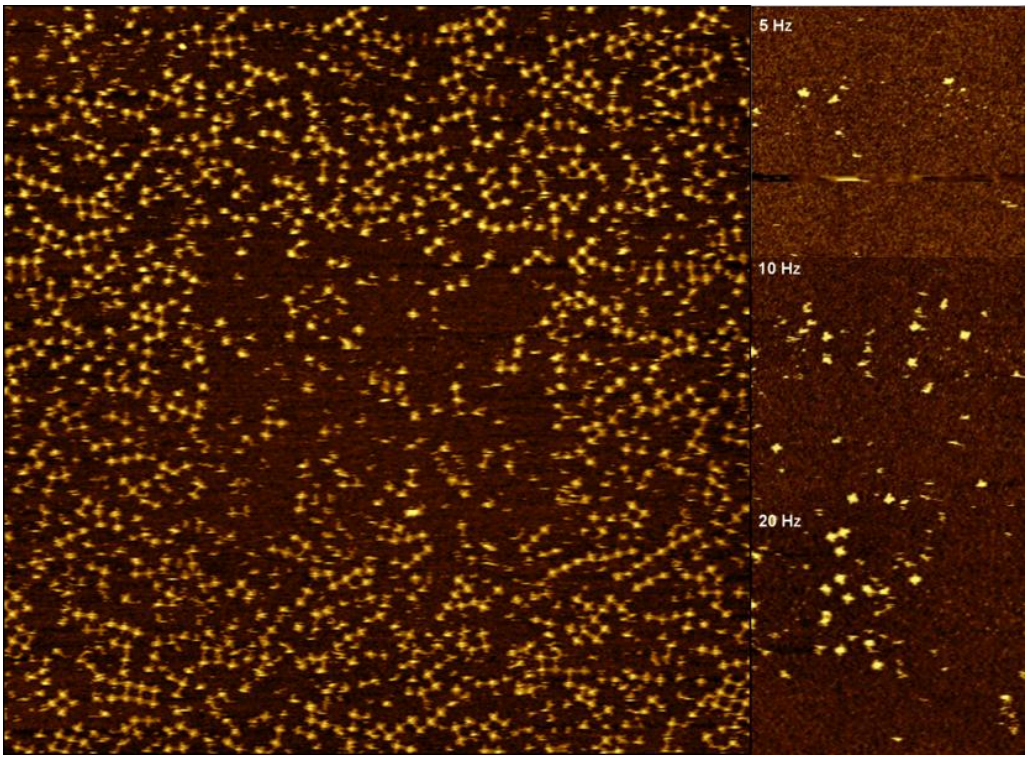

Figure 53. Liquid AFM imaging of TC-ST origami during fast scanning of 5-20 Hz per line. On the left, a zoomed out area is presented, that was imaged using 5 Hz, 10 Hz and 20 Hz imaging frequency. In the fast-scanned area an emptier spot can be seen in middle of the figure. On the right, zoomed areas of 5 Hz, 10 Hz and 20 Hz imaging frequencies are shown from top to bottom, respectively. Imaged by Dr. Charlotte Kielar from HZDR.

G Temperature dependence of the 6×4 blunt-end TC-ST origami design

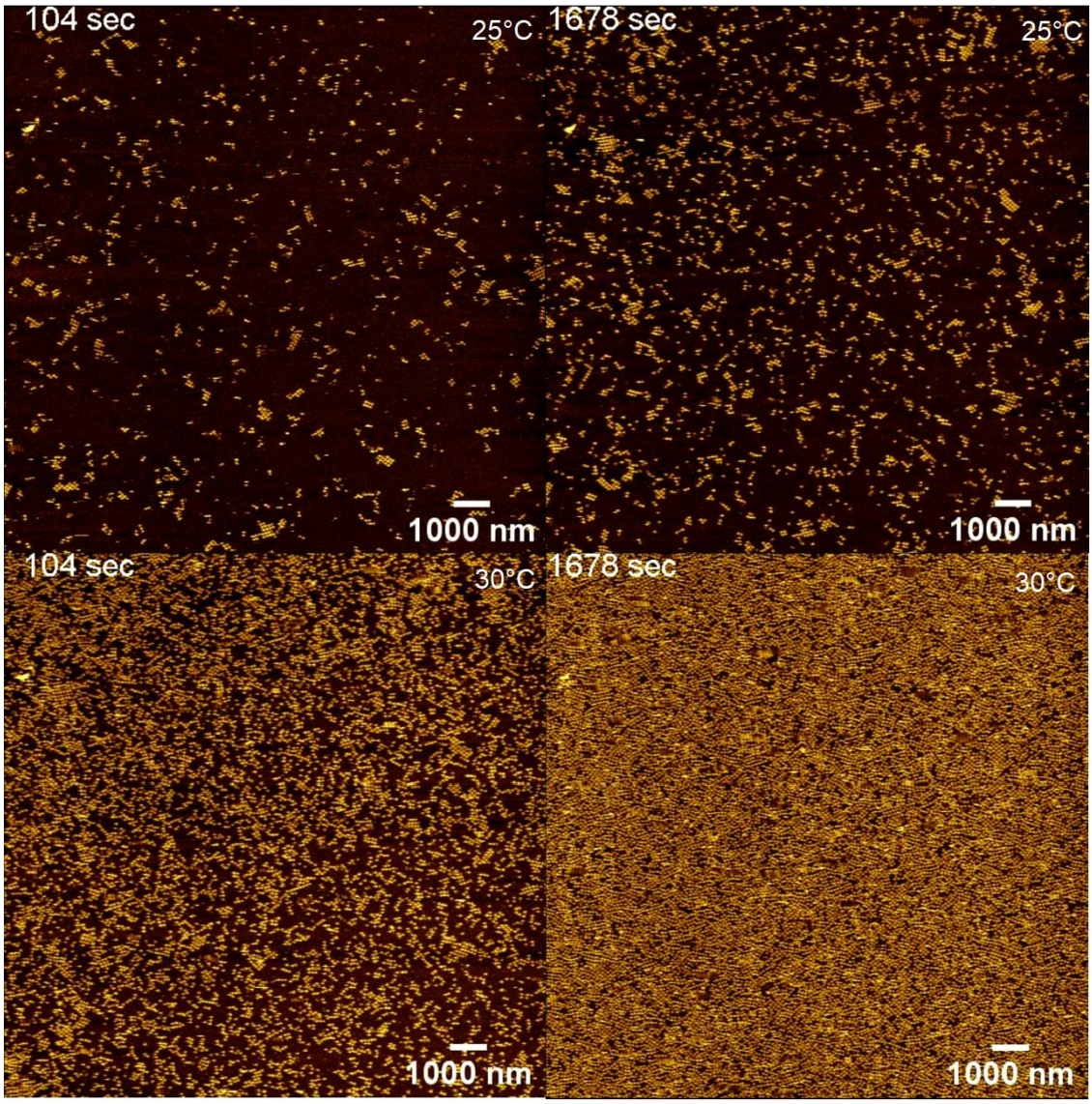

Figure 54. Temperature controlled liquid AFM imaging of 12 nM TC-ST origami with 6×4 blunt-ends in 12.5 mM magnesium and 150 mM sodium buffer in 25 °C and 30 °C. Imaged by Dr. Charlotte Kielar from HZDR.

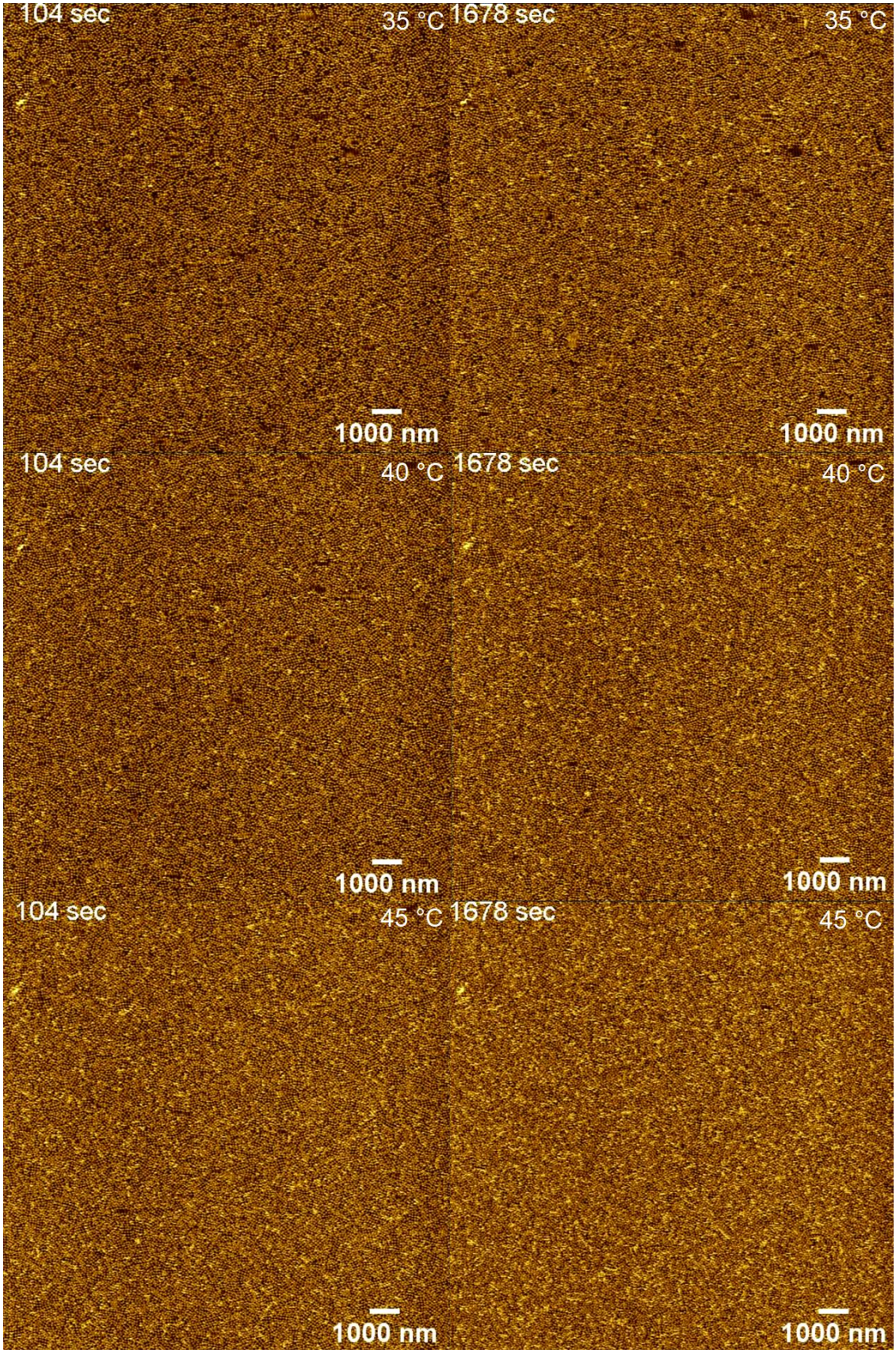

Figure 55. Temperature controlled liquid AFM imaging of 12 nM TC-ST origami with 6×4 blunt-ends in 12.5 mM magnesium and 150 mM sodium buffer in 35 °C, 40 °C and 45 °C. Imaged by Dr. Charlotte Kielar from HZDR.

H Temperature dependence of the 5×4 blunt-end TC-ST origami design

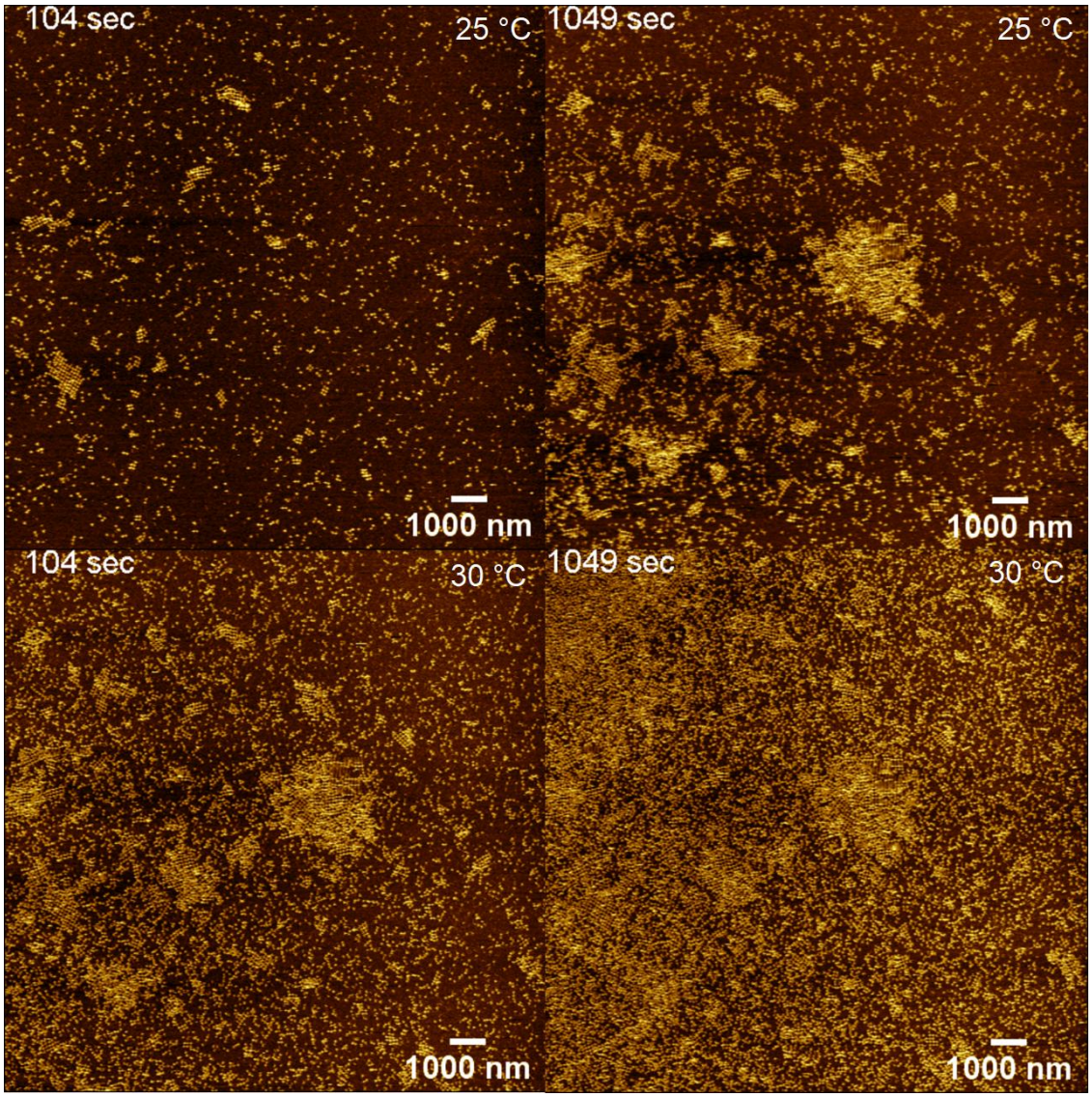

Figure 56. Temperature controlled liquid AFM imaging of 12 nM TC-ST origami with 5×4 blunt-ends in 12.5 mM magnesium and 150 mM sodium buffer in 25 °C and 30 °C. Imaged by Dr. Charlotte Kielar from HZDR.

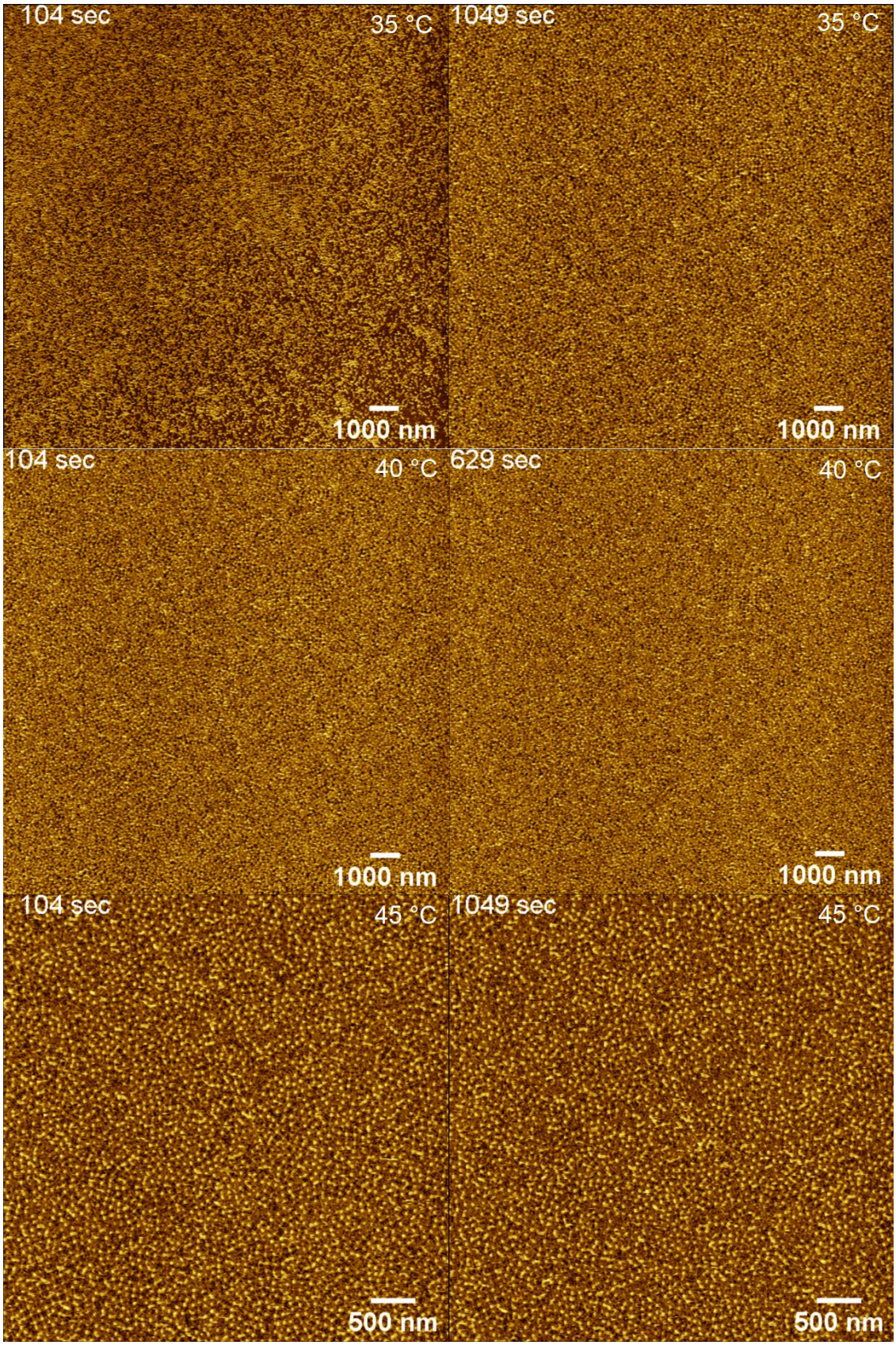

Figure 57. Temperature controlled liquid AFM imaging of 12 nM TC-ST origami with 5×4 blunt-ends in 12.5 mM magnesium and 150 mM sodium buffer in 35 °C, 40 °C and 45 °C. Imaged by Dr. Charlotte Kielar from HZDR.

I Temperature dependence of the 4×4 blunt-end TC-ST origami design

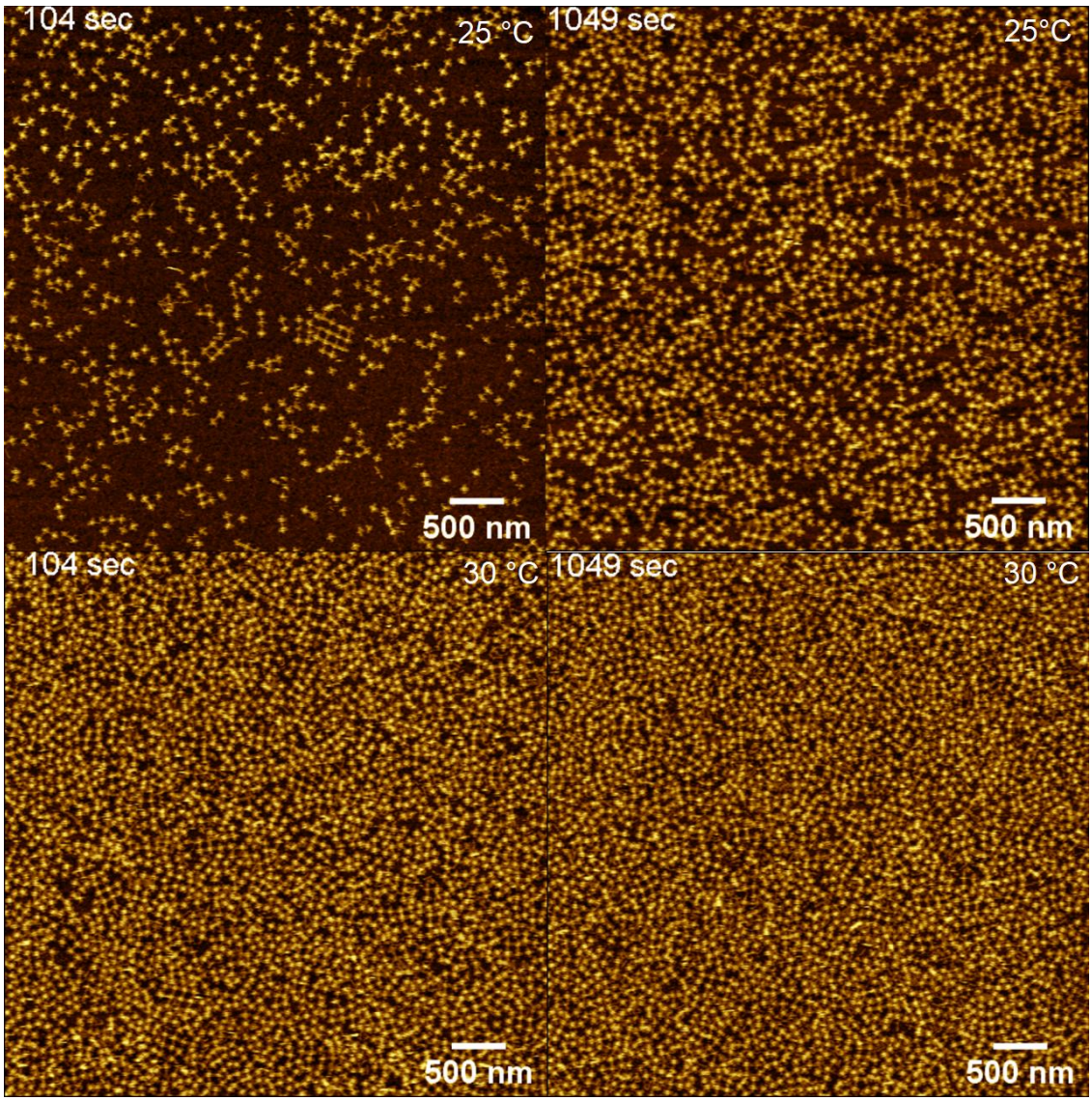

Figure 58. Temperature controlled liquid AFM imaging of 12 nM TC-ST origami with 4×4 blunt-ends in 12.5 mM magnesium and 150 mM sodium buffer in 25 °C and 30 °C. Imaged by Dr. Charlotte Kielar from HZDR.

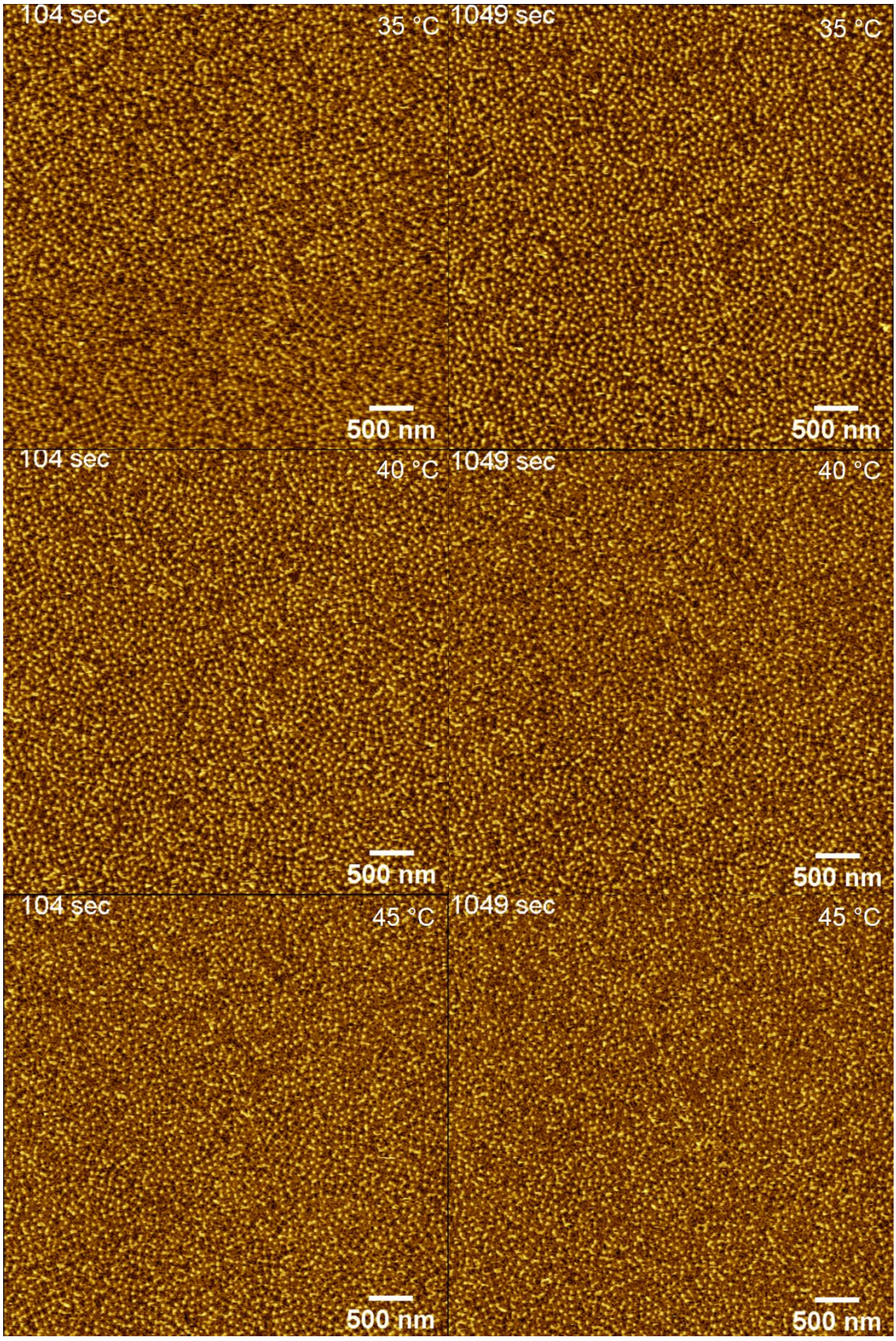

Figure 59. Temperature controlled liquid AFM imaging of 12 nM TC-ST origami with 4×4 blunt-ends in 12.5 mM magnesium and 150 mM sodium buffer in 35 °C, 40 °C and 45 °C. Imaged by Dr. Charlotte Kielar from HZDR.

J Temperature dependence of the 3×4 blunt-end TC-ST origami design

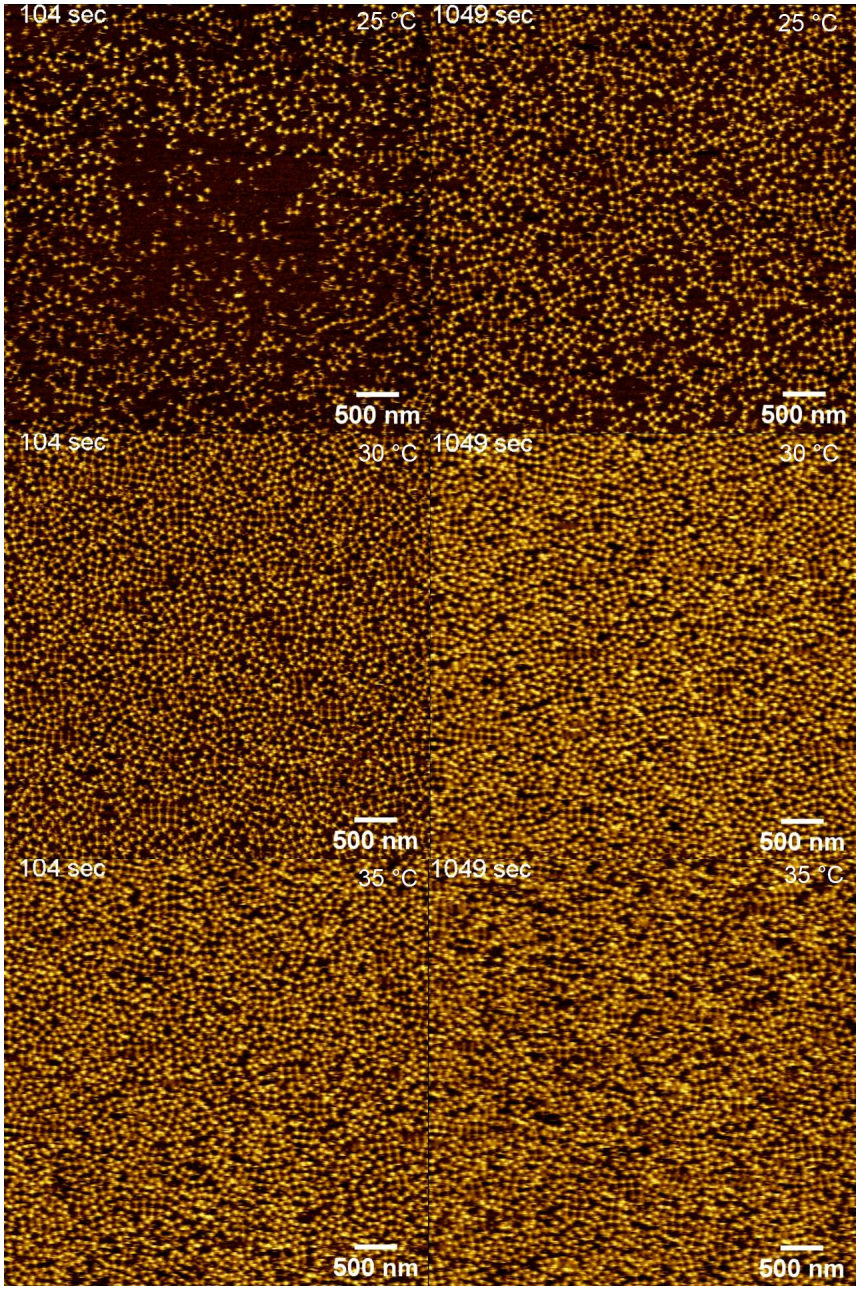

Figure 60. Temperature controlled liquid AFM imaging of 12 nM TC-ST origami with 3×4 blunt-ends in 12.5 mM magnesium and 150 mM sodium buffer in 25 °C, 30 °C and 35 °C. Imaged by Dr. Charlotte Kielar from HZDR.

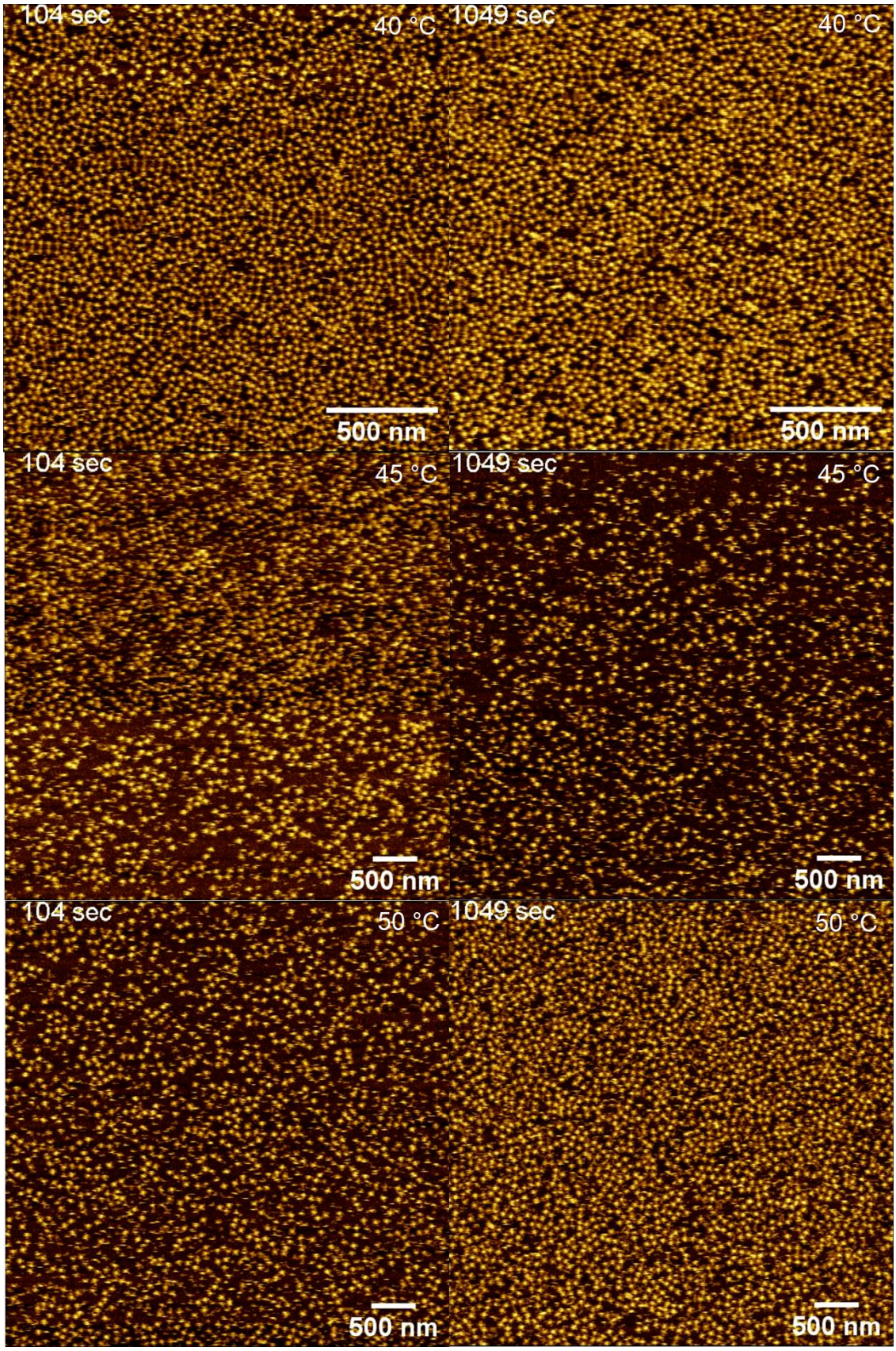

Figure 61. Temperature controlled liquid AFM imaging of 12 nM TC-ST origami with 4×4 blunt-ends in 12.5 mM magnesium and 150 mM sodium buffer in 40 °C, 45 °C and 50 °C. Imaged by Dr. Charlotte Kielar from HZDR.